1-1-2016

Engineering Gold Nanoparticles And Their Use To Control Nucleation

Pedram Jahanian
Wayne State University,

ENGINEERING GOLD NANOPARTICLES AND THEIR USE TO CONTROL NUCLEATION

by

PEDRAM JAHANIAN

DISSERTATION

Submitted to the Graduate School

of Wayne State University,

Detroit, Michigan

in partial fulfillment of the requirements

for the degree of

DOCTOR OF PHILOSOPHY

2016

MAJOR: CHEMICAL ENGINEERING

Approved By:

_____

Advisor Date

_____

_____

_____

_____

DEDICATION

This dissertation is dedicated to my parents for their unconditional support throughout every steps of my life and to my brother, sister.and Aida.

Also, I would like to dedicate this dissertation to Mr James Hetfield who helped me get through dark times of my life.

ACKNOWLEDGEMENTS

First of all, I would like to deeply appreciate my advisor, Prof. Guangzhao Mao, for her most graceful help during my whole Ph. D. study and also for the trust she had in me when enrolling me into her group.

I also wish to thank all of our research group,.Dr Sunxi Wang, Dr Li Li, Dr Song Xu for their guidance and Mr Fangchao Liu, Ms. Lingxiao Xie and Xuecheng Yu for their beneficial discussions during our group meetings and daily experiments.

I also wish to thank my committee members, Dr. Steve Salley, Dr. Gholam-Abbas Nazri, Dr Da Deng and Dr. Jeffrey Potoff for their helpful suggestions and valuable recommendations related to this dissertation.

I would like to acknowledge the financial support from National Science Foundation and Wayne State Universtiy Nano Incubator.

Finally, I wish to express my deepest appreciation to my family and friends specially Aida for their encouragement and patience during this time.

TABLE OF CONTENTS

LIST OF TABLES

LIST OF FIGURES

CHAPTER 1 INTRODUCTION

In chemistry, the term organic-inorganic hybrid is used for crystalline materials that combine organic and inorganic components in a molecular scale. Recently, Organic-inorganic hybrid materials have drawn a lot of attention in electronic, optical and biosensing applications due to their unique chemical and physical properties. One of the unique features of hybrid materials is that they can show properties that are absent in either of their building blocks. Although a lot of work has been done to synthesize nanocrystals with controllable size and shape, scalable production of hybrid organic-inorganic materials with controllable properties is still a major challenge. [1]

In this study, nanohybrids consisting of inorganic nanoparticles and organic nanorods were produced by a seed-mediated nucleation (SMN) method via electrocrystallization on highly oriented pyrolytic graphite (HOPG) substrate. Before going into the synthesis of the organic part, the controlled formation of the inorganic seeds were thoroughly investigated. Gold was selected as an inorganic nano seeds because of its easy synthesis methods and well-studied crystal structure. Gold nanoparticles (AuNPs) were synthesized using the electrochemical methods, and we were able to control the size, and for the first time, the shape of the AuNPs. Later a universal strategy will be introduced to synthesize particle-rod inorganic-organic hybrid materials. The choices of organic materials for nanorods are tetrathiafulvalene bromide ((TTF) $Br_{0.76}$) and partially oxidized potassium tetracyanoplatinate ($K_{1.75}Pt(CN)_4 \cdot 1.5H_2O$) also known as Krogmann's salt or KCP. Both are chosen in part due to their high electrical conductivity. Later the same principles were employed to manufacture a vapor detecting prototype sensor using KCP crystals. We also studied the octadecyltrichlorosilane (OTS) particle lithography, and we

were able to produce uniform OTS nanorings that have electronic and pharmaceutical applications. This study contributes to the understanding of SMN theory and organic-inorganic nanohybrid materials research, which has been organized as following:

Chapter 2 presents the background literature review on seed-mediated nucleation and crystallization of hybrids. The applications of organic crystals will be presented, and later the potential applications of the hybrid structures will be introduced.

In chapter 3, experimental methods that were used to characterize the structure and properties of the materials will be presented. The characterization tools that were used in this study include, Atomic Force Microscopy (AFM) which was the main characterization tool in our work, Field-Emission Scanning Electron Microscopy (FE-SEM), Energy Dispersive X-ray Spectroscopy (EDS), Transmission Electron Microscopy (TEM) and X-ray Diffraction (XRD).

Chapter 4 will explain the particle lithography method for producing the multilayer OTS nanoring pattern on the silicon wafer substrate. The optimum conditions that favor the surface condensation versus polymerization reaction were investigated. Also, the conditions which lead to thicker rings were studied. The multilayer rings later were used as nano-flasks to deposit organic nanoparticles, and we show that the nanoparticles deposition were controlled by the OTS nanopattern.

In Chapter 5, electrochemical synthesis of AuNPs on freshly cleaved HOPG with controlled morphology will be presented. A universal strategy will be introduced to control the size and also the shape of the AuNPs; which later were used as seeds to synthesize the inorganic-organic hybrid materials. The morphology of the particles will be studied mostly with AFM and FE-SEM.

Chapter 6 demonstrates the electrochemical crystallization of organic crystals on the nanoparticle seeds. $(TTF)Br_{0.76}$ nanocrystals were fabricated electrochemically on AuNP decorated HOPG substrate. AuNPs deposition which was thoroughly studied in the previous chapter will be used in this chapter. Similar to chapter 5 the morphology of the AuNP-$(TTF)Br_{0.76}$ hybrid structures were studied with AFM and FE-SEM. The size of the formed TTF crystals were studied with respect to AuNP seeds to investigate heterogeneous nucleation.

In chapter 7, similar to chapter 6 the synthesis of a hybrid material was investigated. AuNPs were used as the seed for the particle-rod hybrid structure. The organic material of choice is KCP. The electrodeposition condition and size of KCP nanorods on AuNP decorated HOPG was studied with AFM and FE-SEM. Later the same principles were employed to synthesize bigger KCP crystals to manufacture a vapor detecting prototype. The sensor monitors the conductivity of the KCP crystal that is formed on a gold pattern. In order to monitor the conductivity of the sensor, it was connected to an electrochemical workstation and the impedance of the crystals was measured while the sensor is exposed to the target vapors. The sensor response to water vapor, methanol, ethanol, isopropanol, dichloromethane, and hexane was studied and to be able to compete with commercial sensors three main factors for commercial sensors were investigated that include: selectivity, reproducibility, and sensitivity.

And finally in chapter 8, conclusions from this study and suggestions for future work will be presented. Overall, the study proves that SMN theory was successfully employed to control the size of the organic crystals and form hybrid structures. Also by

using electrochemical methods, a promising prototype vapor detecting sensor was manufactured that later can be used for producing low-cost sensors.

CHAPTER 2 LITERATURE REVIEW

2.1 Basis of nucleation and crystallization

2.1.1 Concept and scope

The most commonly used theory to describe the nucleation process is the classical nucleation theory. The classical nucleation theory was introduced by Becker (1935) and developed by Volmer (1939) and Gibbs (1948). It was based on the vapor to liquid condensation and later was extended to liquid to solid crystallization. This theory describes the nucleation process from the free energy change.[2] The overall excess free energy, ΔG, is the sum of surface excess energy, ΔG_S, which is the excess free energy between the surface of the particle and bulk of the particle and ΔG_V, which is the excess free energy between the particle and the solute in the solution. ΔG_S is proportional to r^2 and is positive, ΔG_V is proportional to r^3 and in supersaturated solution is negative. [2] Therefore:

$$\Delta G = \Delta G_S + \Delta G_V$$

$$= 4\pi r^2 \gamma + \frac{4}{3}\pi r^3 \Delta G_v \qquad \text{(Equation 1)}$$

Because of the two positive and negative terms, the overall free energy of nucleus formation has a maximum value. This value or ΔG_{crit}, corresponds to the critical nucleus radius, r_c, which can be obtained by differentiating the above equation:

$$r_c = \frac{-2\gamma}{\Delta G_v} \qquad \text{(Equation 2)}$$

And:

$$\Delta G_{crit} = \frac{16\pi\gamma^3}{3(\Delta G_v)^2} = \frac{4\pi\gamma r_c^2}{3} \qquad \text{(Equation 3)}$$

The existence of the newly created crystal depends on its size and it can either grow or re-dissolve in the solution. If the free energy of the particle decreases then the crystal

will grow, therefore r_c is the minimum size of the stable nucleus. Particles with a diameter less than r_c will dissolve because this is the only way that its free energy can be reduced and similarly the larger particle will continue to grow. The nucleation rate, J, means the speed of nuclei formation and can be explained by the following equation:

$$J = Aexp(-\Delta G/\mathbf{k}T) \quad \text{(Equation 4)}$$

From the Gibbs-Thomson relationship, ΔG_{crit} can be derived as:

$$\Delta G_{crit} = \frac{16\pi\gamma^3 v^2}{3(\mathbf{k}T \ln S)^2} \quad \text{(Equation 5)}$$

Therefore:

$$J = Aexp\left[-\frac{16\pi\gamma^3 v^2}{3k^3T^3(\ln S)^2}\right] \quad \text{(Equation 6)}$$

This equation shows that nucleation rate is dependent on three main variables, interfacial tension, γ, degree of super-saturation, S, and temperature T.

2.1.2 Heterogeneous nucleation

The nucleation rate can be affected drastically by the presence of impurities in the system. The impurity particles can act as nucleation seeds to induce heterogeneous nucleation. The overall free energy barrier in heterogeneous nucleation will be less than the free energy barrier in homogeneous condition. Their ratio is defined as ϕ:

$$\Delta G'_{crit} = \phi \Delta G_{crit} \quad \text{(Equation 7)}$$

In which ϕ is:

$$\phi = \frac{(2+\cos\theta)(1-\cos\theta)^2}{4} \quad \text{(Equation 8)}$$

In this equation, θ is the angle of contact between the crystalline deposit and the foreign particle surface. The nucleation rate increases with decreasing free energy barrier.

The interfacial tension, γ, with a power of 3 is one of the important factors controlling the nucleation process. Figure 2 shows the interfacial energy diagram between three present phases in this process, two solid phases, and one liquid phase. Figure 1 represents a schematic of heterogeneous nucleation on a foreign particle seed.

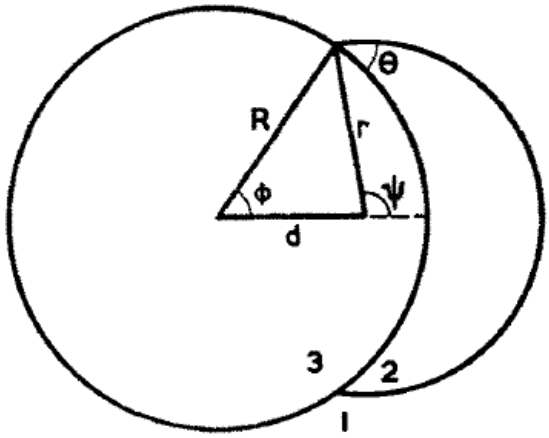

Figure 1. (1) Embryo (2) on the nucleating particle (3) in parent phase. [2]

Resolving these interfacial forces will result in:

$$\gamma_{sl} = \gamma_{cs} + \gamma_{cl} \cos\theta \qquad \text{(Equation 9)}$$

And:

$$\cos\theta = \frac{\gamma_{sl} - \gamma_{cs}}{\gamma_{cl}} \qquad \text{(Equation 10)}$$

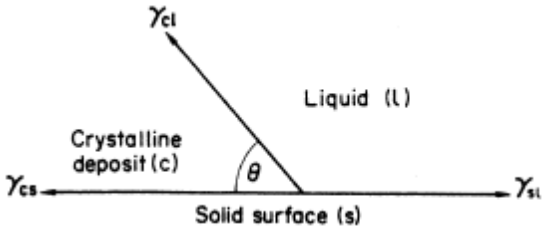

Figure 2. Interfacial forces between the phases present at the boundary of the phases. [2]

As described, the nucleation rate in the presence of a foreign seed is related to the size of the seed, and the contact angle of the crystalline deposit and the seed surface. The contact angle is determined by three interfacial energies. These factors were summarized by Fletcher in Figure 3. In this figure, m is cosθ and x is the ratio of the seed size to critical nucleus radius. It can be seen that the most effective size for the seed is 1 to 10 times the size of critical nucleus radius. When x is more than 10, the effect of the seed size is diminished, and when x is less than 1 the seed does not have much effect in the crystallization.

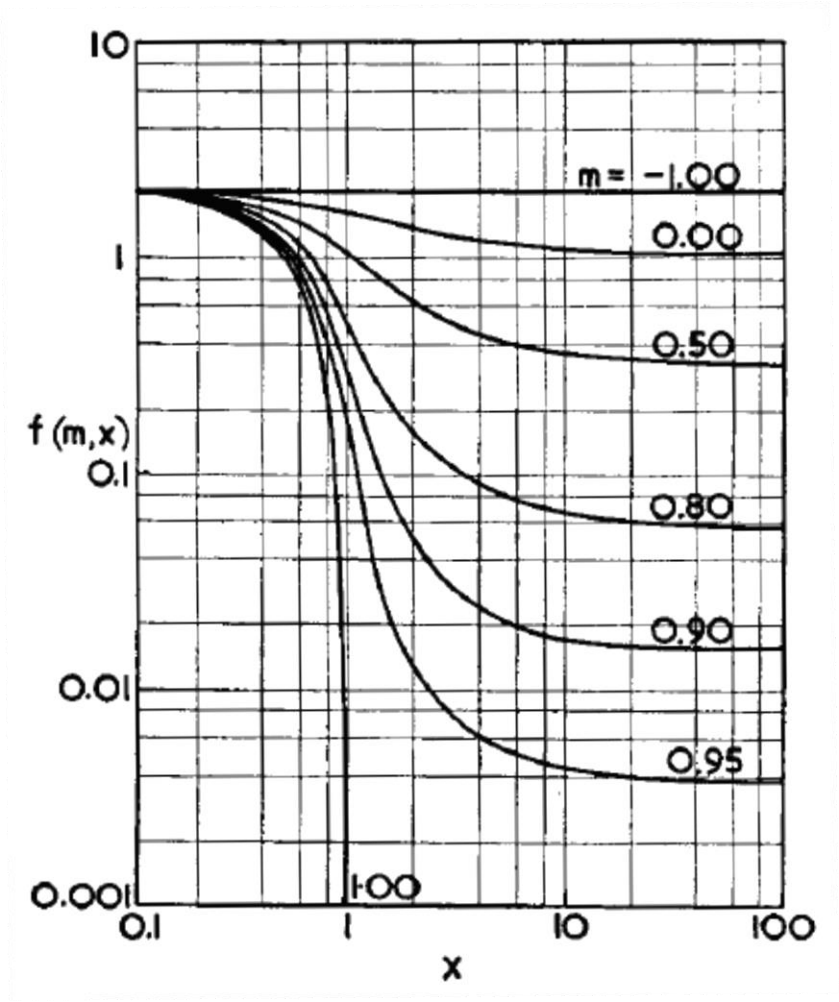

Figure 3. Geometrical factors in terms of radius ratio and contact angle. [2]

When heterogeneous nucleation is applied on the nanoscale, a nanoparticle seed can be used to nucleate species with different chemical natures from the seed. In addition, the size and morphology of the seed may be used to control the size and shape of the crystal grown. Figure 4 shows a schematic example of an organic nanorod with an inorganic nanoparticle as nucleation seed.

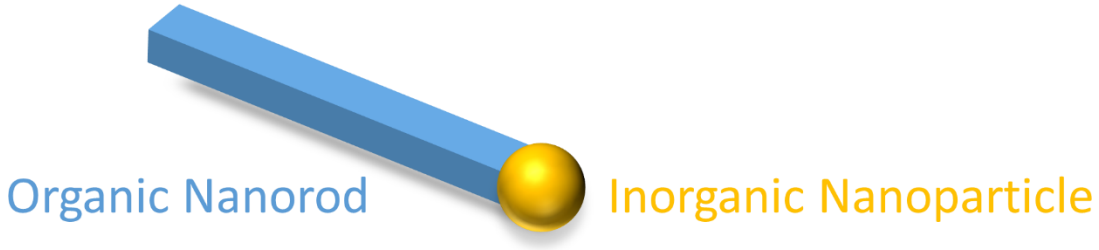

Figure 4. Schematic of hybrid seed-mediated nucleation

Cacciuto et al. reported the numerical simulation of heterogeneous crystal nucleation in colloidal suspensions. Monte Carlo simulations were used to study the spherical seed size effect on crystallization. The crystal nucleation energy barrier was calculated to predict the crystal growth on the seed particle. A low energy barrier translates to an easy crystallization. The results show that to promote the crystallization the seed size should be more than a minimum size, otherwise the seed will not be “seen”. On the other hand, when the seed size is very large the particle will be seen as a flat surface, and the particle and a macroscopic crystal will cover the surface. When the seed size is between these two ranges the crystal will grow radially on the surface. Figure 5 shows a schematic of the simulated crystallization on the seed with different diameters. The results show that when the smaller seed is present, the crystal will grow in a rod shape in the radial direction.

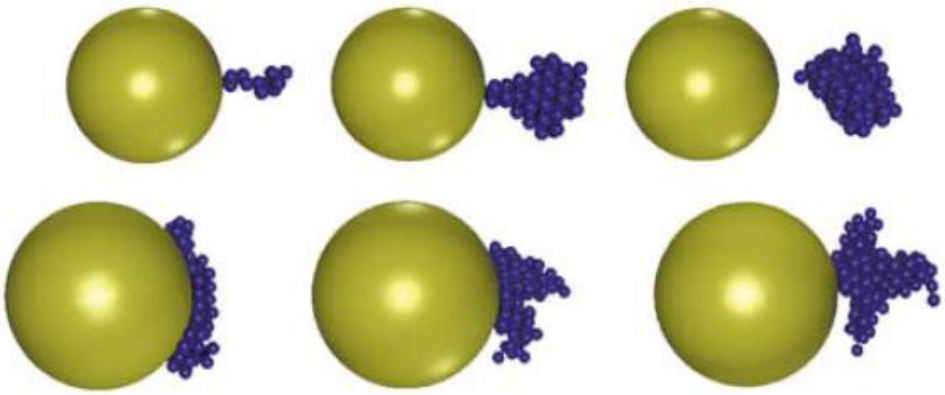

Figure 5. Snapshot sequence of crystal nucleation simulation for different sizes of seeds. Seed radii for top row is $R_s = 5\sigma$ and $R_s = 7\sigma$ for bottom row. σ is the diameter monodisperse spherical colloids. The nuclei size is increasing from left to right.

Nanocrystals can be confined with three known methods, nano-pores [3-5], nanopatterns [6-7], and nanoparticles [8]. In this study, we focus on nanoparticle and nanopattern crystal confinement. Penner's group reported the electrochemical synthesis of TTF-Bromide nanorods on platinum nanoparticles that follows the heterogeneous nucleation theory.The length of TTF-Bromide nanorods are in micrometer range, and their width is linearly related to the diameter of the platinum seed. The size of platinum seed range from 70 nm to 1.3 μm and TTF-Bromide rod width is range from 30 nm to 600 nm. SEM images of the obtained platinum particles and hybrid Pt(TTF)Br are shown in Figure 6. whose results show 15-25% of the platinum nanoparticles involved in TTF(Br) crystallization. The analysis of the TTF(Br) formation on platinum seeds is shown in Figure 7. The data shows a clear linear relationship between the TTF(Br) and platinum nanoparticles diameter with a remarkable correlation of 0.99. The slope of the plot 0.423 that is the ratio of platinum nanoparticle width to TTF(Br) nanorod width.

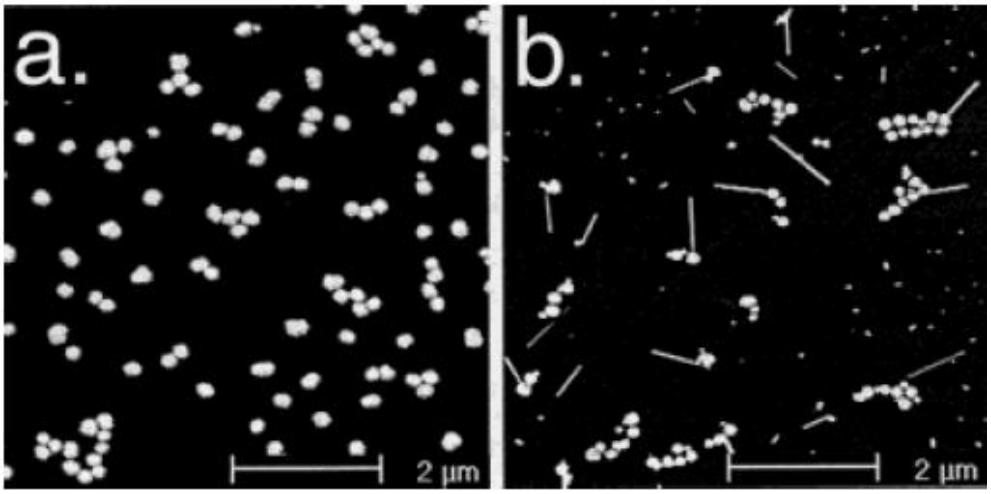

Figure 6. SEM images of (a) Pt-decorated HOPG substrate (b) electrocrystallization TTF(Br) nanorods on Pt nanoparticle seeds (Pt/TTF(Br) Hybrid). [9]

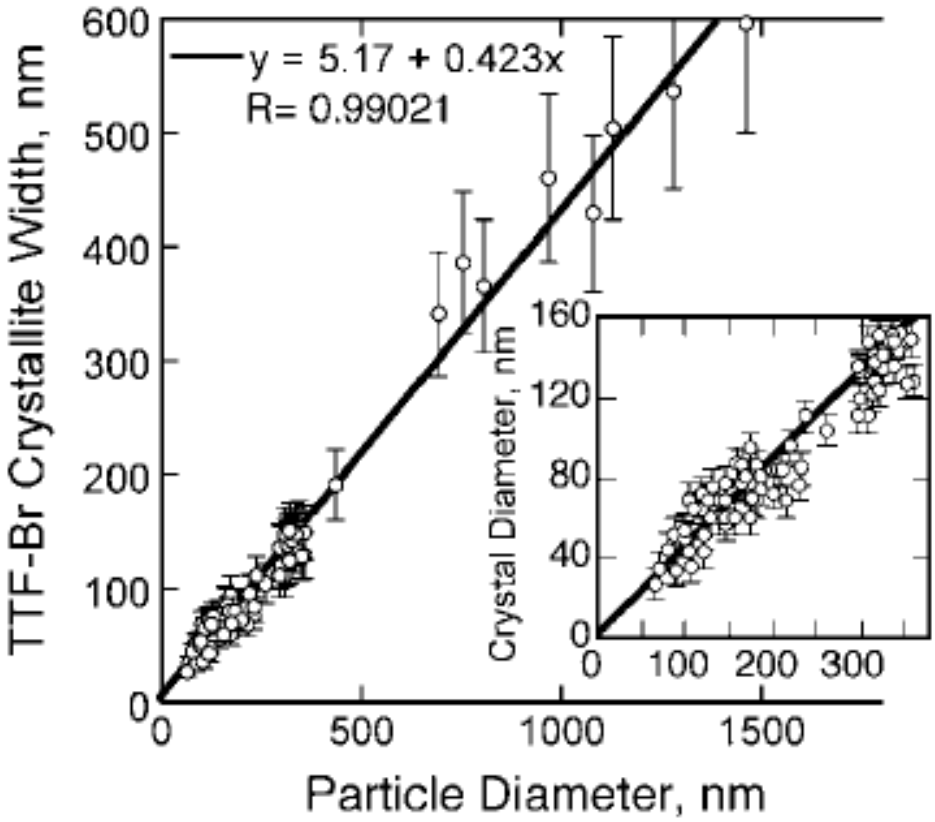

Figure 7. Plotted TTF(Br) nanorods width versus the nucleation Pt nanoparticle diameter.

Another example of nanoparticle confinement is the synthesis of carboxylic acid nanorods on oleylamide-capped gold nanoparticles (OA-AuNPs) using spin coating method reported by Mao's group. [10] Carboxylic acids form an epitaxial pattern when they are deposited on bare HOPG, but this pattern changes to nanorods in the presence of nanoparticles. Figure 8 shows the AFM height images of the epitaxial pattern on HOPG for different carboxylic acids. The carboxylic acid film thickness is 0.3 ± 0.1 nm. After introducing OA-AuNPs to the solution, the AuNPs changed the carboxylic acid formation pattern. The data show the formation of nanorods with the height ranging from 0.8 to 1.1 nm and the width ranging from 7 to 11.4 nm. (Figure 9)

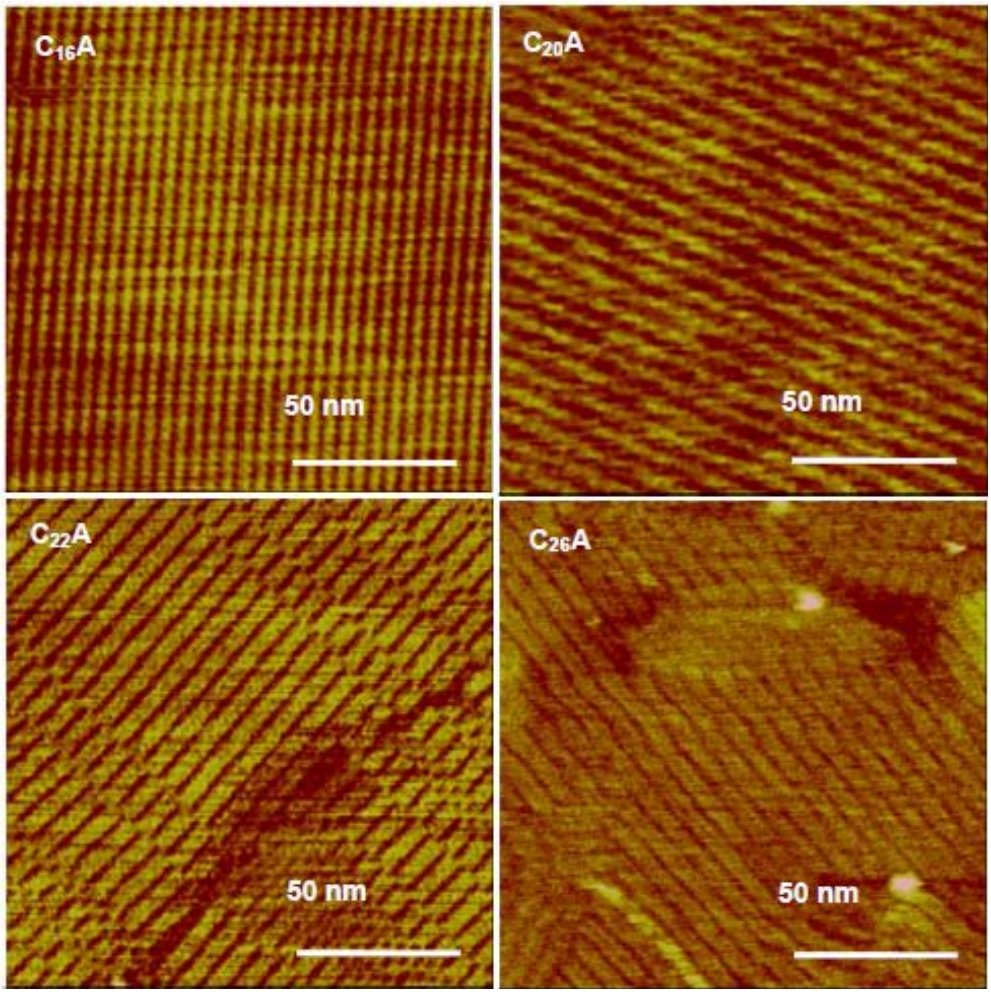

Figure 8. AFM height images of the n-carboxylic acid monolayers on HOPG substrate. (z-range = 1 nm). [10]

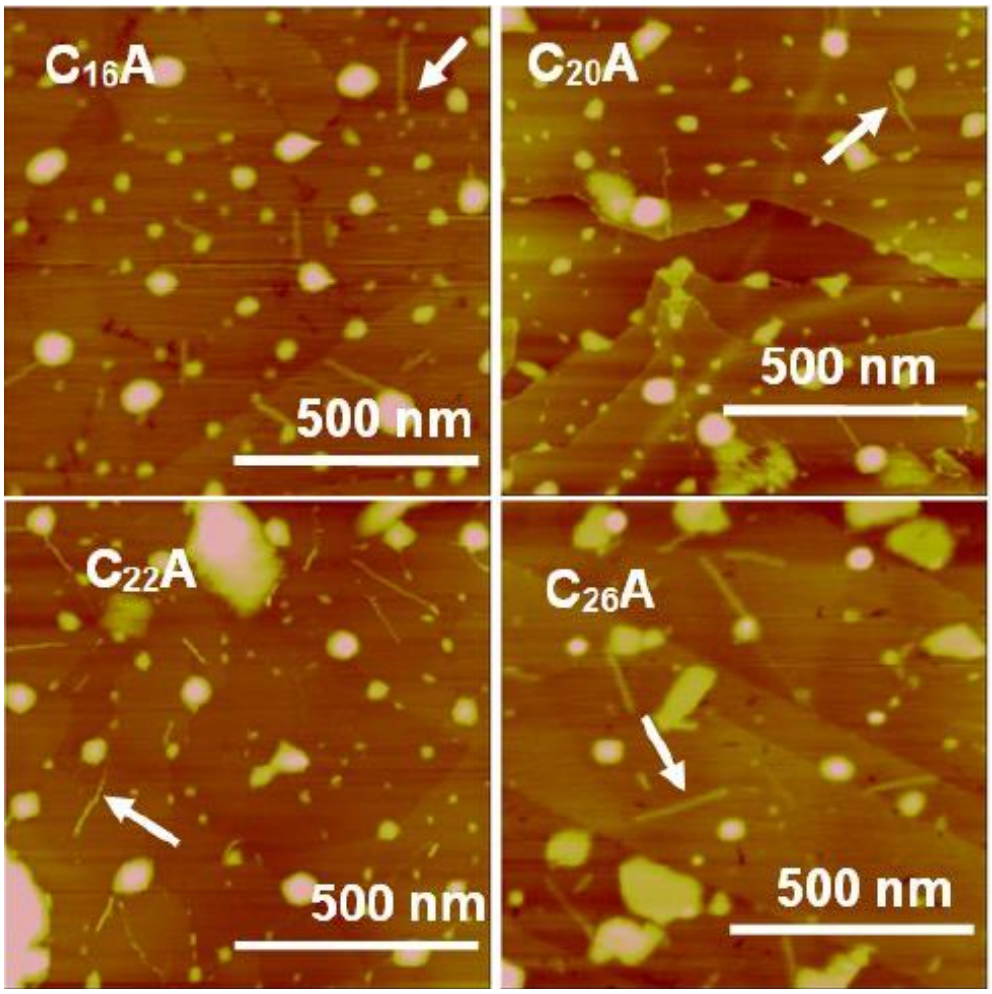

Figure 9. AFM height images of n-carboxylic acid nanorods nucleated on OA-AuNPs on HOPG substrate. The z-rang for all the images is 10 nm.[10]

2.1.3 Seed-mediated growth in shape controlled synthesis of nanocrystals

Seed-mediated growth method is one of the most efficient methods for controlled synthesis of metallic nanocrystals. In this method, the nucleation stage and growth stage are separated from each other to allow more control over the size and shape of the nanocrystals. Compared to other methods, solution based methods have a higher potential for low-cost manufacture of nanocrystals with well-defined morphologies. [11]

Although several parameters are known to affect the growth of metallic nanocrystals, the exact mechanisms for the shape-controlled synthesis of metallic

nanocrystals are still not well understood. [11-12] In fact, understanding of the mechanisms that lead to the synthesis of crystals with a specific shape has only recently emerged.

Metallic nanoparticles are an interesting subject for scientists in the past century and now are heavily used in biomedical and engineering applications. [13] They can be modified with a variety of chemical groups which allow them to be used as a vehicle for drugs, antibodies, genes and ligands. This makes them good candidates for the targeted drug and gene delivery and diagnostic imaging applications. [14-15] There have been developments for medical imaging tools such as ultrasound, CT, and MRI for the imaging of various disease states that leads the use of different metal nanoparticles like gold and silver as contrast agents in these devices. [16] Among metal nanoparticles, AuNPs are interesting because of their distinct optical properties, which is due to their unique interaction with light. AuNP optical properties depend on the size and shape of the particles that make these properties tunable with the morphology of the particles. Due to these interesting optical properties, there is considerable ongoing research on AuNPs with applications in biological imaging.

Research in the past decade has yielded synthetic methods of several nanocrystal shapes. Table 1 lists various shapes including cube, sphere, spheroid, cuboctahedron, octahedron, tetrahedron, right bipyramid, decahedron, icosahedrons, thin plate with a triangular, hexagonal, or circular profile, and rod or wire with different cross sections.

Table 1. Summary of the different shapes of nanocrystals synthesized. [17]

Structures	Shapes	Schematic drawings	Metals
single-crystal	perfect/truncated cube[a]		Pd, Ag, Au, Pt, Cu, Rh, Bi, Fe
	perfect/truncated octahedron[a]		Pd, Ag, Au, Pt
	perfect/truncated tetrahedron[a]	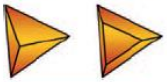	Ag, Au, Pt, Rh
	rectangular bar		Pd, Ag, Pt
	octagonal rod		Pd, Au, Fe, Co, Ni
	rectangular or octagonal wire	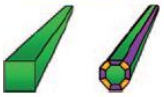	Pb, In, Sn, Sb, Fe, Co
singly twinned	right bipyramid		Pd, Ag
	beam		Ag
multiply twin-ned	decahedron[a]		Pd, Ag, Au
	icosahedron[a]		Pd, Au
	five-fold twinned pentagonal rod		Pd, Ag, Au, Cu
	five-fold twinned pentagonal wire	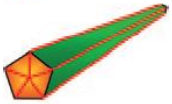	Ag, Au, Cu
	triangular/hexagonal plate		Pd, Ag, Au, Cu, Pb, Bi, Co, Ni
	disc		Sn, Co

To approximate the most stable product, the formation of single-crystal seeds can be considered in the context of Wulff's theorem, which is based on the minimization of the total interfacial free energy of a system with a given volume. For an fcc structure with a lattice constant of a and bond length of ε, the surface energies of the low-index crystallographic facets that typically encase nanocrystals can be estimated as:

$\gamma\{100\} = 4(\varepsilon/a^2)$, $\gamma\{110\} = 4.24(\varepsilon/a^2)$, and $\gamma\{111\} = 3.36(\varepsilon/a^2)$

These equations results in the energetic sequence of $\gamma\{111\} < \gamma\{100\} < \gamma\{110\}$. Such a sequence implies that a single-crystal seed should take an octahedral or tetrahedral shape in order to maximize the expression of {111} facets and minimize the total surface energy. Both shapes, however, have larger surface areas than a cube of the same volume. As a result, single-crystal seeds are expected to exist as truncated octahedrons (or Wulff polyhedrons) enclosed by a mix of {111} and {100} facets. This shape has a nearly spherical profile and thus the smallest surface area to minimize the total interfacial free energy. Such seeds have been used in the synthesis of a number of metal nanocrystals. [17]

The right half of Figure 10 summarizes the correlation that has been established between different types of seeds and the final nanocrystals of an fcc metal. In general, from single crystal seeds, octahedrons, cuboctahedrons, or cubes will be produced depending on the relative growth rates along the {111} and {100} directions. If uniaxial growth is somehow induced, the cuboctahedral and cubic seeds will grow into octagonal rods and rectangular bars, respectively. From singly twinned seeds, right bipyramids enclosed by {100} facets, a nanocrystal consisting of two right tetrahedrons symmetrically placed base-to-base, will be produced. Interestingly, these seeds can also evolve into nanobeams when uniaxial growth is initiated. From multiple twinned seeds, icosahedrons, decahedrons, and pentagonal nanorods (or nanowires) can be produced, depending on whether the {100} planes on the side surface are stabilized or not. Finally, when the seeds contain stacking faults, they will grow into thin plates with the top and bottom faces being {111} facets and the side surfaces being enclosed by a mix of {100} and {111} facets. Because of the six-fold symmetry of an fcc system, these seeds typically become thin plates with a hexagonal

cross-section. As the growth is continued, the final products can also take a triangular shape by eliminating the {111} facets from the side surfaces. [18]

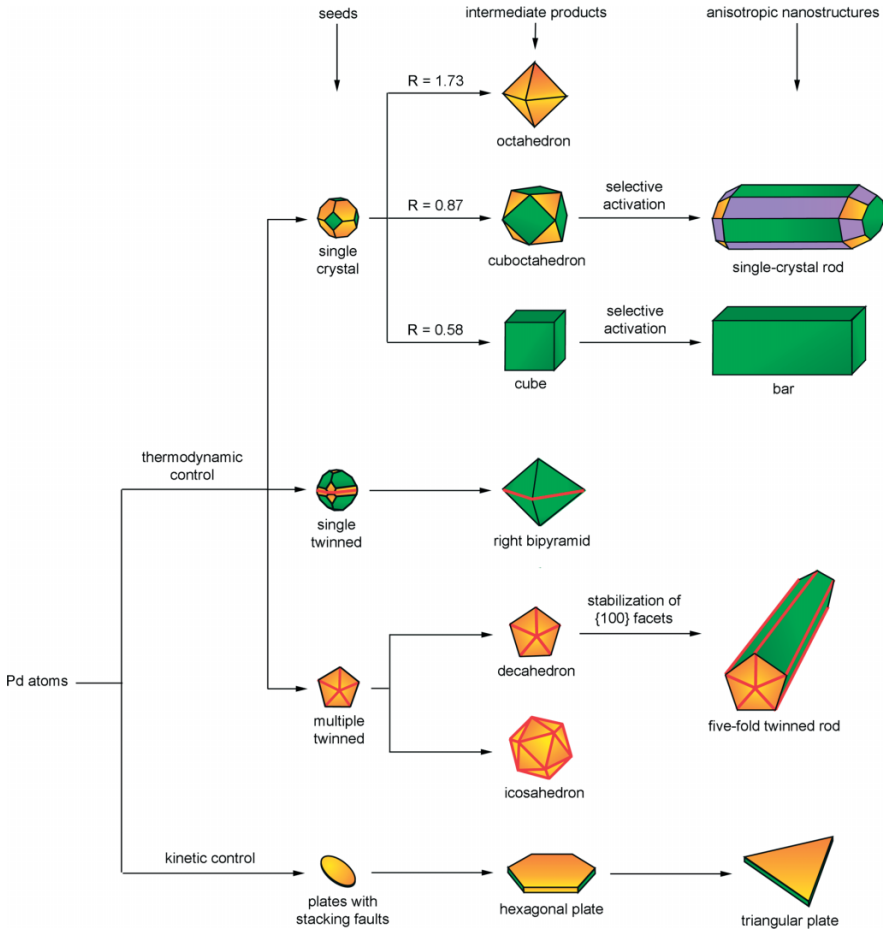

Figure 10. Reaction pathways that lead to fcc metal nanocrystals having different shapes. [18]

First, an ion is reduced to form the nuclei. Once the nuclei have grown larger than a certain size, it becomes a single crystal seed, singly twinned crystal, or multiple twinned crystal. In Figure 10 orange, green and purple colors represent the {111}, {100}, and {110} facets, respectively. Twin planes are delineated in the drawing with red lines. The parameter R is defined as the ratio between the growth rates along the ⟨100⟩ and ⟨111⟩ directions. [18]

The shapes presented in Figure 10 are the generic shapes that can be produced from the seed. It is possible that the final shape differs from these general shapes due, to the surface capping effect or other factors like impurities. The capping effect is one way to change the final shape of the crystal. This is achieved by decreasing the free energy of crystal's specific facet with a capping agent. The first paper suggesting the capping effect was published on 1986 by Harris [19] reporting that quasi-spherical Pt nanocrystals grew to cubic shape when they were exposed to H_2S gas. It was proposed that {100} facets were formed over {111} because the {100} faces were interfaced with sulfur. In this process, S is a capping agent that interacts more strongly to the {100} facet and because of it the {100} facet will form preferentially compare to {111} leading to a dominated cube-shape. Another example of a capping agent is polyvinylpyrrolidone (PVP) that is a polymeric capping agent whose oxygen atoms react strongly with the {100} facets of Pd and Ag. This alternation will affect the surface energy sequence and change the relative growth rate for different facets. According to Wulff's theorem the final shape of the crystal should have the minimum surface energy, therefore by changing the orders of the surface energy we alter the final shape of the crystal. An example of the effect of PVP capping agent is presented in Figure 11. [20]

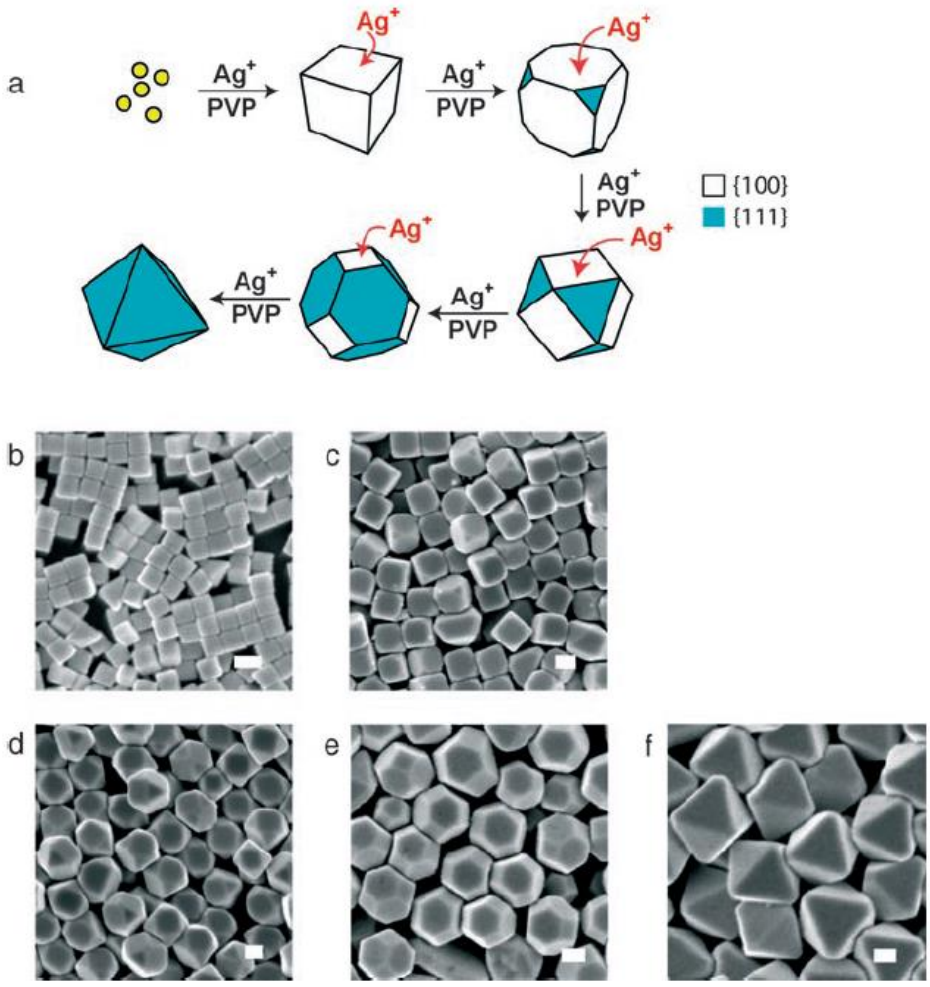

Figure 11. Overgrowth process of Ag nanocrystals, in which Ag atoms are continuously deposited onto the {100} facets of an Ag nanocube to eventually result in an octahedron enclosed by {111} facets. [20]

As an example of controlling the shape with capping effect Niu et al. [21] were able to synthesize three different shapes of gold crystals from different seeds. The gold seeds with an average size of 3 nm were prepared then grown to nanorods with ~30nm in width and ~60nm in length to act as seeds for making rhombic decahedral (RD), octahedral and cubic gold nanocrystals by changing the conditions and concentrations. Cetylpyridinium chloride (CPC) was used as the capping agent. The final shape of the crystals is controlled by the variation of the CPC concentration and concentration of reducing agent (ascorbic

acid). Figure 12 shows different SEM images of gold nanocrystals made by different types of seeds.

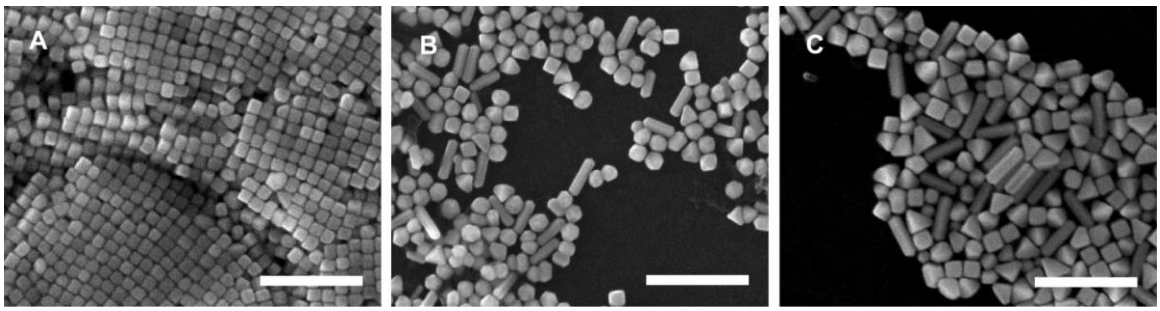

Figure 12. The effect of the seed in crystal shape. (A) ~3 nm cetylpyridinium chloride (CPC) capped single crystal gold seeds (B) ~3 nm citrate-capped twinned gold seeds, and (C) ~1.5 nm cetyltrimethylammonium bromide (CTAB) capped single crystalline Au seeds. (Scale bars: 500 nm) [21]

2.2 Potential applications of hybrid structures

2.2.1 Applications of nanoparticles

Due to their unique electronic, chemical and optical properties; particles in the nanometer size range are very attractive for technological applications. AuNPs have attractive electronic, optical, thermal and catalytic properties, which can be used in physics, chemistry, biology, medicine, and material science. [22-23] Synthesis of AuNPs can be divided into two categories, colloidal-based methods, and surface-based methods. By far the most common and simplest way to produce AuNPs is the reduction of $H[AuCl_4]$ by sodium citrate. [24] Besides sodium citrate, other reducing agents such as borohydride can also be used.[25] AuNP arrays can be prepared by first synthesizing the particles in solution and then depositing them on the surface or can be synthesized directly on the substrate. The substrates can be glass, metal, or carbon. Applications of AuNPs in recent two decades are vastly increased. Some examples for each of the important applications will be presented below.

AuNPs are designed for use as conductors from printable inks to electronic chips. In the world of electronics, nanotechnology becomes an enabling technology as electronic devices are becoming more and more compact. AuNPs are used to connect resistors and other elements of a microchip. In the electronic system, low resistance conductors are very important for the development of low-cost systems like radio frequency identification tag. Low resistance conductors are essential for the fabrication of high-Q inductors, capacitates, tuned circuits and interconnections. Making circuits by printing will lead to a huge cost reduction. Huang et al. proposed to use solutions of organic-encapsulated AuNPs to be printed and annealed to form the high-conductivity patterns. [26]

Stuchinskaya et al. suggested a four-part consulate consisting of an antibody, polyethylene glycol, phthalocyanine and gold particle as a potential drug for targeted photodynamic breast cancer therapy. AuNPs when excited by light at a wavelength range of 700 to 800 nm, produce heat. This enables these nanoparticles to destroy targeted tumors. When light is applied to the tumor that contains the AuNPs, the particles will heat up, causing the tumor cells to die. This treatment is known as hyperthermia therapy. [27]

AuNPs are used in a variety of different sensors, for example, a colorimetric sensor based on AuNP can identify if food is safe to be consumed. Other methods, like surface enhanced Raman spectroscopy, use AuNPs as substrates to measure the vibrational energies of chemical bonds. This method can also be used to detect pollutants and proteins. [28]

AuNPs are used as catalysts in a number of chemical reactions. The surface of a AuNP can be used for selective oxidation. For example, AuNPs are being developed to be used

in fuel cell applications. These studies can be useful in the display and automotive industry. [29]

2.2.2 Applications of organic crystals

One of the major new technologies that use organic materials is organic light-emitting devices (OLED), which are used in display screens in devices like monitors and cell phones. Typically, OLED is an organic layer sandwiched between two electrodes. Applied potential between the two electrodes causes radiation emission in the visible range. The first OLED was made in 1963 by Pope et al. that used anthracene. [30] Since then many improvements have been made regarding the OLED materials. Organic thin film transistors (OTFT) are another type of displays that are the next generation of thin film transistors. The use of organic materials makes flexible displays possible.

Another example of industrial use of organic materials is organic photovoltaic cells (OPVC) that are made by sandwiching one or two layers of organic electronic materials between two metallic conductors. When the organic layer absorbs light, electrons will be excited to the lowest unoccupied molecular orbital at it causes a current to flow. A lot of research has been done since the invention of photovoltaic cells, [31] and the net conversion efficiency of the cell has been improved with the use of organic materials. [32]

Carbon nanotubes (CNTs) and graphene have attracted great attention for numerous applications for future flexible electronics, owing to their supreme properties including exceptionally high electronic conductivity and mechanical strength. [33] Figure 13a shows three examples of all- CNT thin-film transistors. Q. Cao et al. reported transparent and flexible all-CNT thin-film transistors on a PET substrate. [34] V. K. Sangwan et al. reported split buried-gate all-CNT transistors, in which the CNT electrodes were prepared by a

solution process and the dielectric layer composed of an Al_2O_3 and PMMA bilayer (Figure 13b). [35] In both of the above examples, flexibility was limited. S. Aikawa et al. recently reported an extremely flexible and deformable all-CNT transistor (Figure 13c), in which the substrate and dielectric layer were made of PVA. [36]

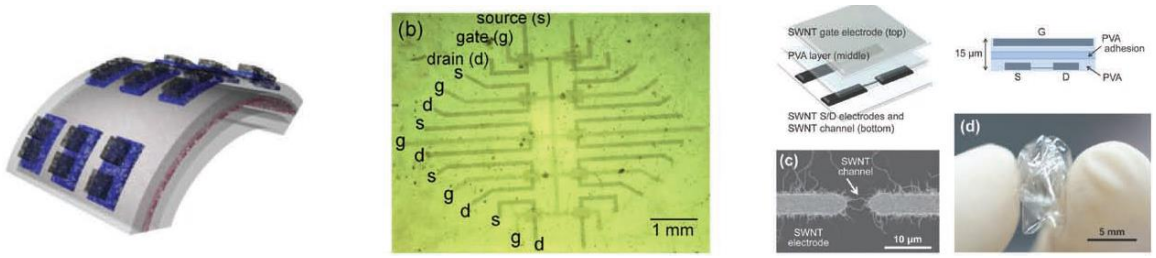

Figure 13. Different types of CNT transistors. [34-36]

Individual CNTs and materials based on CNTs have been widely investigated for a diverse array of applications. In recent years, focus on CNTs has grown to include their possible biological applications, such as drug delivery transporters, selective cell destruction agents, biosensors, cellular growth substrates, and prosthetic implant materials (Figure 14). [37]

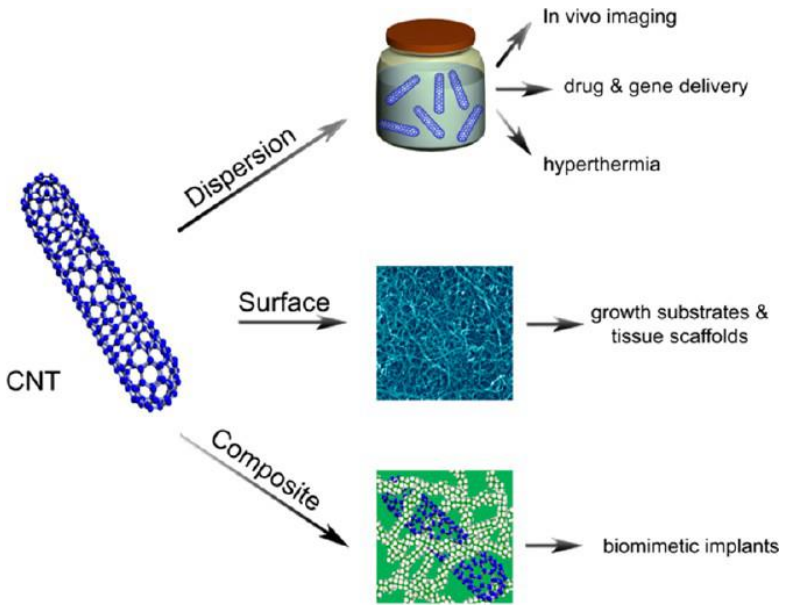

Figure 14. Different forms of CNTs and their biomedical application. [37]

One of the first studies on the use of CNTs for drug delivery has been carried out by Wu et al. in 2005, who conjugated MultiWalled Nanotubes (MWNTs) to the antibiotic amphotericin B, a drug considered problematic due to its narrow therapeutic index and poor aqueous solubility. [38] Both issues could be resolved by conjugating to MWNTs, which reduced the toxicity of the drug toward mammalian cells while preserving its antifungal activity. In the following years, many more studies have been conducted, almost solely focusing on the delivery of anticancer drugs. The first studies were undertaken in this area mainly focused on functionalization issues, whereas subsequent studies investigated the therapeutic activity of the systems in vitro. Current studies are trying to tackle the challenge of in vivo settings in order to move a step further toward the clinical applications and investigate the fate of the CNTs in living systems. [37]

2.2.3 Potential applications of hybrid structures

There are many applications for hybrid structure, but in this study, we emphasize on inorganic-organic structures. Inorganic-organic materials represent a new way to design new materials and compounds with improved features which have promising applications in biology, medicine, energy, electronics, coatings, fuel and solar cells catalyst, *etc.* [1]

Trindade et al. reported the synthesis of organic-inorganic materials using organic capped AuNPs and polystyrene. The optical properties of the composites are dominated by plasmonic effects and are related to the morphology of the hybrid product. They show that the optical response of the nanocomposites can be tuned with the AuNPs arrangement within the polymer matrix. They reported a universal strategy to control the optical response of the nanocomposites with the morphology of the polymer nanoparticles containing AuNPs. [39]

Yuet et al. introduced a method to directly attach AuNPs to carbon nanotubes (CNT) with high dispersity by reducing the interfacial tension between the CNT and solution using a small amount of ethanol. The results show a well-distributed GNP decorated CNT using this method. They were able to control the attached AuNP density by adjusting the weight ratio between the AuNPs and CNTs. The electrochemical catalytic properties of the hybrid CNTs were characterized, and they showed a higher oxygen reduction rate compare to reported data for bare CNTs. [40]

There have been extensive studies to use AuNPs in biomedical research in the past decades, and promising applications have been introduced. DNA has been widely used with the combination with nanoparticles for biological applications. [41] Yamada et al. were able to synthesize inorganic-organic materials by mixing double stranded DNA with

inorganic materials for a selective absorbance of harmful compounds. They were able to improve the mechanical strength of the DNA by mixing it with silane coupling reagents and synthesize a water soluble hybrid material which could accumulate harmful DNA-intercalating compounds. [42]

CHAPTER 3 EXPERIMENTAL METHODS

3.1 Atomic force microscope (AFM)

Atomic force microscope (AFM) is a surface imaging technique with lateral resolution on the order of fractions of a nanometer. In this study, AFM is our main tool for nanomaterials characterization. AFM consists of five main parts, laser beam, photodiode, cantilever tip, scanner, and the controller. The AFM tip is a nano-fabricated probe that is on a flexible cantilever with a specific spring constant. AFM works by bringing a probe in contact or close to the surface. A laser beam is focused on the cantilever and the reflection is recorded with the photodiode. A repulsive force between the sample and the tip bends the cantilever upwards. The amount of bending, measured by a laser spot reflected on to a split photodetector, can be used to calculate the force. By keeping the force constant while scanning the tip across the surface, the vertical movement of the tip follows the surface profile and is recorded as the surface topography by the AFM (Figure 15).

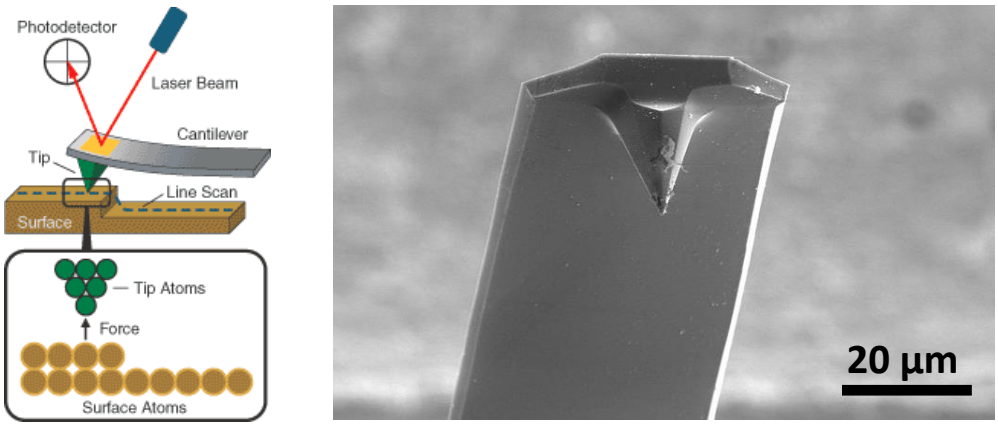

Figure 15. Schematic of an Atomic Force Microscope (left) and SEM image of an AFM tip (right).

AFM has three modes of operation, contact mode, none contact mode, and tapping mode. First and the most common mode of operation is the contact mode. In the contact

mode, tip will scan across the sample surface, and the cantilever deflection will be monitored by the photodiode detector as the tip moves over the surface corrugation. None contact mode measures the surface topography by sensing the van der Waals forces between the surface and tip. The third mode is the tapping mode. In this mode, AFM will sense the surface by tapping the surface at a high frequency. The cantilever is oscillated at its resonance frequency ranging from 50- 400 kHz in the air. One of the advantages of AFM compare to other surface characterization devices is that it can operate in liquid. Therefore, it is possible to conduct real-time imaging for a variety of experiments. In this research, we conduct *in-situ* AFM characterization of the electrochemical processes by AFM imaging in liquid in an electrochemical cell. The surface of the substrate is imaged in real time while it is connected to the potentiostat. When the AuNPs were imaged in electrochemical cell the AFM tip can move the particles, makes it difficult to image the particles. This problem can be solved by optimizing the force in contact mode or using the tapping mode in liquid.

All the AFM images presented in this dissertation, were obtained with Multimode Nanoscope IIIA and Dimension 3100 instruments from Bruker.

3.2 Field emission scanning electron microscope (FE-SEM)

The second important tool that we use extensively in our work is FE-SEM. Scanning Electron Microscope (SEM) is a microscope that obtains the surface morphology by scanning it with a focused beam of electrons. The electrons interact with the atoms in the sample and produce various signals. The signals, which contain information about the sample's surface topography and composition, will be recorded. The electron beam will scan the surface, and the image will be produced by combining the beam's position with

the detected signal. SEM can achieve resolution higher than 1 nanometer. Specimens can be observed in a high vacuum, in low vacuum, and (in environmental SEM) in wet conditions.

Field emission SEM is a new generation of SEMs with an improved electron gun that allows us to obtain ultra-high-resolution images at lower voltages and on non-conductive samples. The main difference between FE-SEM and SEM is the source of the electron emission. The emitter type in SEM is thermionic emitter which uses electric current to heat filament (usually tungsten). When the filament is heated enough to overcome the work function of the material, electrons can escape from the material. FE-SEM electron emitter works by putting the filament in a large potential gradient. Field emission gun emits electrons from a much smaller area than a therionic gun which translates to higher image resolution. In this work the selected accelerating voltage is 15 kV for most of the images that sometimes melts the particles. It was observed that in the lower voltages the melting issue can be solved and the image quality can be improved. The Energy dispersive X-ray spectroscopy (EDS) system connected to FE-SEM is an analytical technique used for the elemental mapping or chemical composition analysis. EDS detects X-rays emitted from the sample as a result of the high-energy electron beam penetrating into the sample. X-ray spectra can be collected and analyzed, yielding elemental quantitative information about the sample. With the combination of these two tools, it is possible to analyze a specific part of the sample.

In my preliminary research JSM-6510LV-LGS Scanning Electron Microscope (SEM) was used to analyze the sample and measure the size and shape of the formed nanoparticles and nanorods on the HOPG surface.

3.3 Transmission electron microscopy (TEM)

Transmission electron microscopy (TEM) is a microscopic technique whereby a high voltage beam of electrons is transmitted through an ultra-thin specimen, interacting with the specimen as it passes through. An image is obtained from the interaction of the electrons transmitted through the sample. The image is magnified and focused onto an imaging device, such as a fluorescent screen, on a layer of photographic film, or to be detected by a sensor such as a CCD camera. The typical resolution of TEM is 0.2 nm and with high-resolution TEM, the resolution can be improved up to 0.1 nm. TEM is a suitable tool for characterizing nanoparticles and especially with the solution based synthesized nanoparticles and nanorods. For the preparation of the samples, they should be transferred to a TEM sample support mesh "grid", with ultra-microtome sectioning that allows the electron to pass through the sample and the nanoparticles can be seen by the sensor. We use TEM in characterizing synthesized AuNPs with colloidal technique, and it will provide us size, shape and crystalline planes inside the lattice crystal. We also synthesized the particles directly on the TEM grid with electrochemical methods.

3.4 X-ray crystallography

X-ray scattering techniques are a family of non-destructive analytical techniques that can be used to obtain the chemical composition, crystal structure, and physical properties of the materials and thin films. These techniques are based on observing the scattered intensity of an X-ray beam hitting a sample as a function of incident and scattered angle, polarization, and wavelength or energy. Note that X-ray scattering is different from X-ray diffraction, which is widely used for X-ray crystallography. The X-ray diffraction will provide the crystal structure and chemical composition nanoparticles that cannot be

obtained by AFM. In this study, X-ray diffraction techniques will be used to investigate the crystal structure of the synthesized AuNPs and organic nanocrystals on the HOPG surface.

CHAPTER 4 A SUPRA-MONOLAYER NANOPATTERN FOR ORGANIC NP ARRAY DEPOSITION

4.1 Introduction

Recent advances in nanofabrication made it possible to create micro to nano-scale patterns on the surface. In the last two decades, the microelectronic industry has pushed this study to smaller sizes in order to produce faster computing systems. Several technics have been introduced in making the nanopatterns including, advanced photolithography, [43] laser scanning, [44] serial writing with charged particles, [45-47] micro- and nano-machining, [48-52] direct writing and material deposition, [53-54] transfer printing [55-56] and particle lithography. [57] In the last decade, extensive research has been done on the technics which makes the production of complex structures possible, aiming to lower operational cost and time. In this study, we are using particle lithography to produce a nano-flask pattern.

The self-assembled organosilane monolayers have been studied extensively in the past decade because of their applications in electronics and sensors.[58] They are easy to make, stable and applicable to a variety of different substrates. Octadecyltrichlorosilane (OTS) molecules will attach to the surface of the silicon wafer, with the strong Si-O-Si covalent bond thus, they are good candidates for the nano-flask pattern in this study. In our previous work, we were able to produce a smooth self-assembled monolayer (SAM) of OTS using chemical vapor deposition (CVD) technic. Compare to solutions based methods, [59-60] it is easier to control the amount of water with the CVD method. [61] However, it can complicate the role of water in polymerization and condensation reaction. Water excess can cause organosilane polymerization that will lead to the vertical growth of multilayer islands. [62] In this study, OTS nanorings were produced based on a previously studied method in which the nanorings were formed because of the immersion capillary

forces between the particles and the substrate. [63-64] A two-step method was suggested to obtain two-dimensional (2D) colloid crystals. First, the formation of the nucleus by capillary forces between particles immersed in the water, and next the crystal growth. It is possible to obtain well-ordered nanoring patterns of OTS on the substrate, by employing particle lithography method combined with OTS SAMs. [65-66] Size and surface density of nanorings simply can be controlled by the size of the deposited particles. The obtained rings can be used to deposit a variety of nanoparticles into nanopatterns. For example, drug nanoparticles can be deposited into nanorings by employing the amphiphilic properties of the substrate similar to the deposition of aspirin on a self-assembled phospholipid pattern. [67]

In this study, the conditions which favors the polymerization reaction at the space between the particle and the substrate was investigated. Polystyrene particles were used with 300 nm and 900 nm in diameter, and they resulted in OTS nanorings with the thickness exceeding the monolayer which later can serve as nano-flasks to induce nucleation of small organic molecules like n-docosane that belongs to the n-alkane group which has a well-defined chain length dependent crystallization behavior. Using the OTS nano-flasks to deposit n-docosane crystals resulted in uniform crystal size which is dictated by the nano-flask size.

4.2 Experimental

4.2.1 Materials

n-docosane ($C_{22}H_{46}$, 99%, Aldrich), deionized water (electrical resistivity 18 MΩ-cm, Barnstead water purification system), clarithromycin ($C_{38}H_{69}NO_{13}$, > 95%, Sigma), sodium chloride (99%, Fisher), ethanol (200 proof, Fluka), diethyl ether (> 99%, Alfa

Aesar), potassium sulfate (> 99%, Fisher), 1-butanol (99.9%, Fisher),, n-OTS (95%, Gelest), ethanol (200 proof, Fluka), hydrogen peroxide (30% in water, Fisher), aspirin ($C_9H_8O_4$, >99%, Sigma), sulfuric acid (98% in water, Fisher), chloroform (99.9%, Fisher), heptane (99%, Fisher), n-type silicon (111) wafers (Wafer World), Size-sorted monodisperse polystyrene (PS) latex mesospheres (1 wt.% solution) with particle diameters of 100, 300 and 900 nm (Thermo Scientific)

4.2.2 Sample preparation and particle deposition

Silicon wafers were cut into 1×1 cm^2 squares and were cleaned with piranha solution for 1 hour. Piranha solution is 1:3 volume ratio of 30% hydrogen peroxide and concentrated sulfuric acid which is extremely corrosive. After the cleaning, silicon wafers were rinsed with deionized water to remove the extra solution from the substrate and dried with air. To remove the surfactant in the PS solution, it was centrifuged for three cycles (15 min $cycle^{-1}$) at 15000 rpm. Between each cycle, the participated PS mesospheres were removed from the bottom of the centrifuge tube and resuspended with deionized water. A 30µl of the suspension solution was placed on treated 1x1 cm silicon wafer and dried for 5 hours in ambient condition. To avoid dust contamination on the sample, it was covered with a petri dish during the drying time. PS particles are pulled together by the capillary forces caused by the evaporation, of water and form a close-packed layer on the surface. Later it was dried under vacuum for 30 min to remove the excess water.

Small amounts of water remain under the sphere particles and produce a uniform meniscus under each particle. OTS nanorings were formed from these water rings on the substrate using the CVD method. The substrate was put in a closed container with 100 µl OTS added to the container; then it was kept at 70 °C for 90 min for CVD. Two containers

with 0.13 L and 5.2 L in volume were used and in all experiments, the distance between the silane and the substrate were kept constant at 2cm. After 90 min the samples were removed from the reactor and the PS spheres were removed from the substrate by sonication (Baransonic, 1510R-MTH) in a 1:1 mixture of water and ethanol for 30 min at room temperature.

4.2.3 Characterization

OTS nanopatterns and Organic nanoparticle deposition were studied with both AFM (Digital Instruments Inc. EX1 and Dimension 3100) and FE-SEM (JEOL JSM-7600F). AFM images were obtained with silicon tapping mode probes (VEECO, Budget sensors) with a spring constant of 40 N/m, nominal resonant frequency of 300 kHz, width of 40 μm and length of 125 μm. The AFM imaging was done in tapping mode in air with an integral gain of 0.4 and the proportional gain of 0.8. Scan speed was modified based on the scan size from 0.25 to 1 Hz. Height, phase, and amplitude images were recorded for all the samples although the majority of the analysis were done based on the height image. Nanoscope version 5.2 and Nanoscope analysis version 1.5 were used for the data analysis. The particle lithography was imaged with FE-SEM and later the detached particles were analyzed with TEM. In order to be able to image the particle monolayer on the substrate with FE-SEM, it was coated with a layer of gold using Effacoater.

4.2.4 Organic nanoparticle deposition on the OTS nano-flasks

NP deposition was done by evaporative re-crystallization on OTS nanorings. 40 μL of the solution was placed on 1x1 a cm substrate. It is the optimum volume for a perfect deposition of the NPs on the nanorings. Higher volumes resulted in the coverage of the whole sample with a layer of the n-docosane, and lower volumes lead to incomplete NP

deposition. The substrate then was heated at 90 °C for 30 min and immediately was cooled down to -20 °C.

4.3 Results and Discussion

4.3.1 OTS nanorings pattern using particle lithography

Particle lithography was done based on previous studies by other groups. [63-64] Deposited PS layer on the silicon wafer was imaged with AFM and SEM. Figure 16 shows the obtained AFM and SEM images of 300nm and 900nm PS sphere particles.

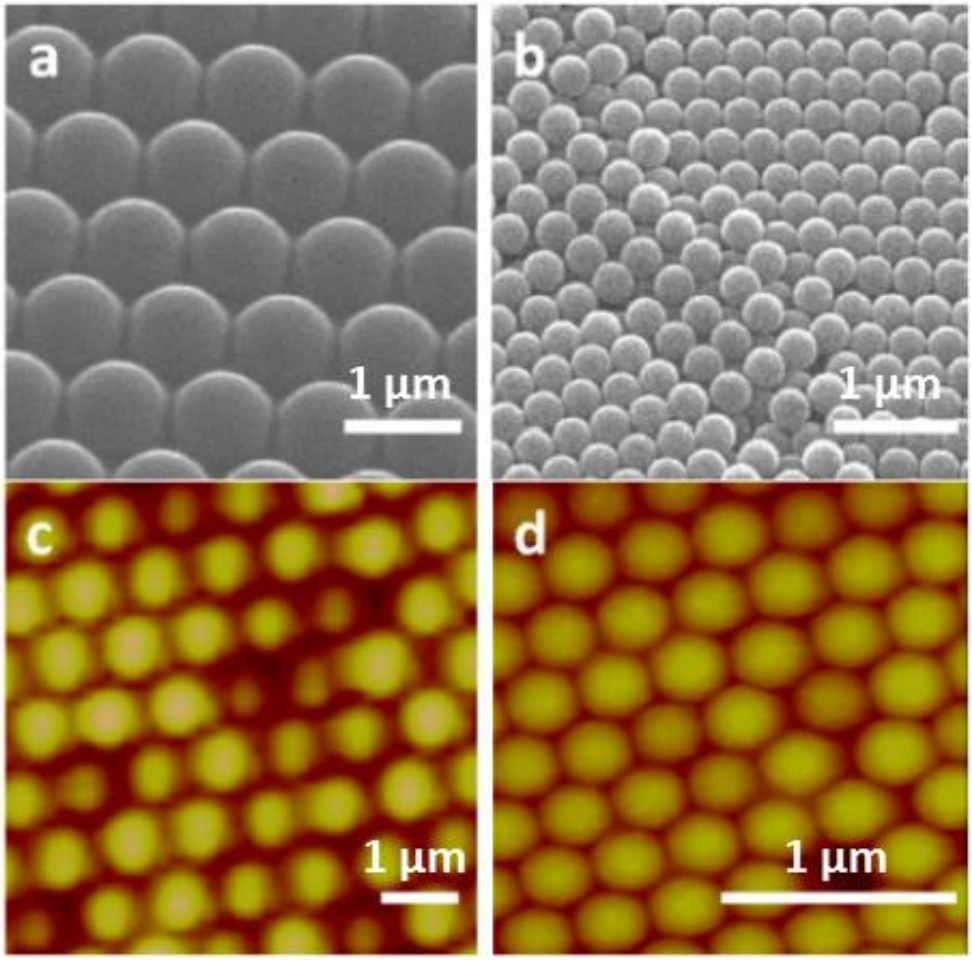

Figure 16. SEM and AFM images of PS particles monolayer on silicon wafer substrate. (a) and (b) are the SEM images of the PS particles, 900 nm, and 300 nm respectively. (c) and (d) are the AFM images of the particles in the same size order. [68]

The PS monolayer on the substrate was used for the formation of the OTS nanorings by CVD of silane with water rings between the sphere particles and the substrate. We were able to reproduce the monolayer rings and also we were able to produce the thicker rings also known as supra-monolayer. Figure 17 demonstrates the AFM images and cross-sectional analysis of the nanorings. Data analysis was done for 50 data points for different parts of the sample. The average ring height is 3.0 ± 0.5 nm (N=50) for 300 nm PS particles and 14.4 ± 2.4 nm (N=50) for 900 nm PS particles that shows a monolayer ring for the 300 nm sphere and a supra-monolayer for the 900 nm sphere.

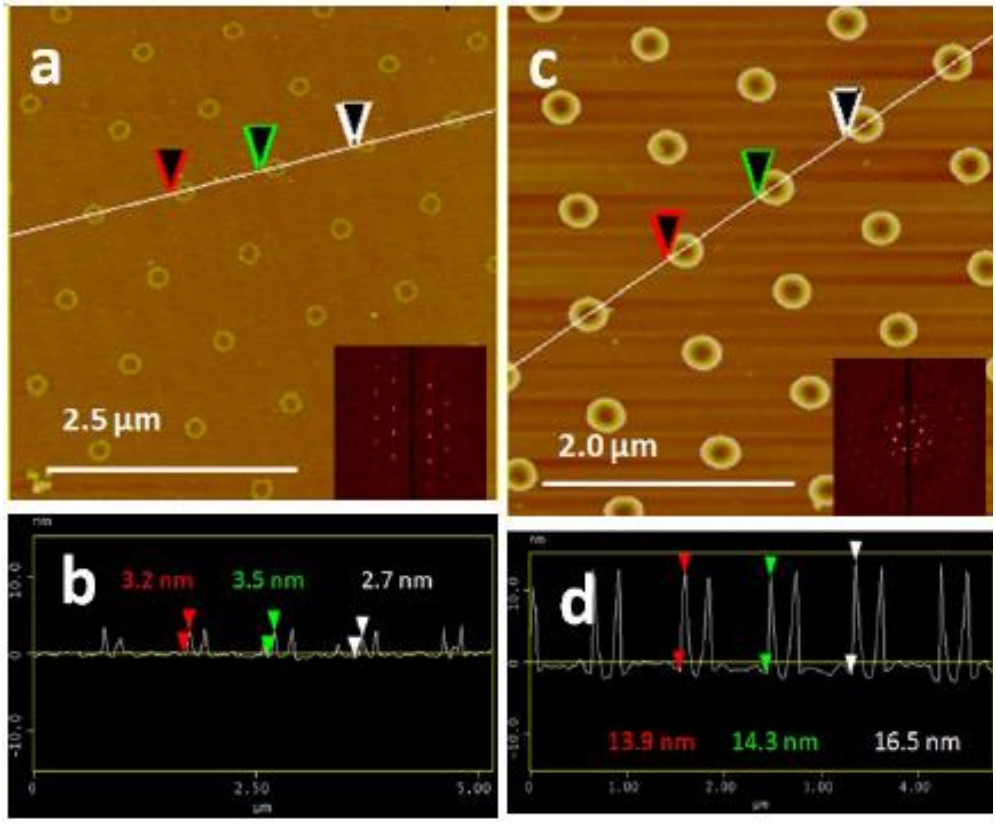

Figure 17. AFM images and analysis of OTS nanorings on a silicon wafer substrate. (a) and (c) are the height images of the OTS rings for 300 nm (Z-range= 30nm) and 900 nm (Z-range=60nm) PS particles respectively. (b) and (d) are the cross sectional analysis of the AFM image. [68]

In this study, we were aiming to produce the thick OTS nanorings that later can be used as a nano reservoir organic NP deposition. Different conditions of the experiment had been studied and thickness of the nanorings was monitored. The experiment was done with different reactor volume, CVD length, and relative humidity while the volume of the silane introduced to the system was kept constant at 100 µL. To understand the effect of each factor, only one of the factors was changed for each experiment. The reservoir volume was 0.13 L and the experiment was done at room temperature (24 ºC) and relative humidity of 5%. CVD time varied from 5 min to 720 min.

The data analysis shows that the nanorings thickness increases with time until 30 min and after this time the growth was not significant. Figure 18 shows the AFM images and cross-sectional analysis of the related image for 5 min (a) and 720 min (b) reaction time.

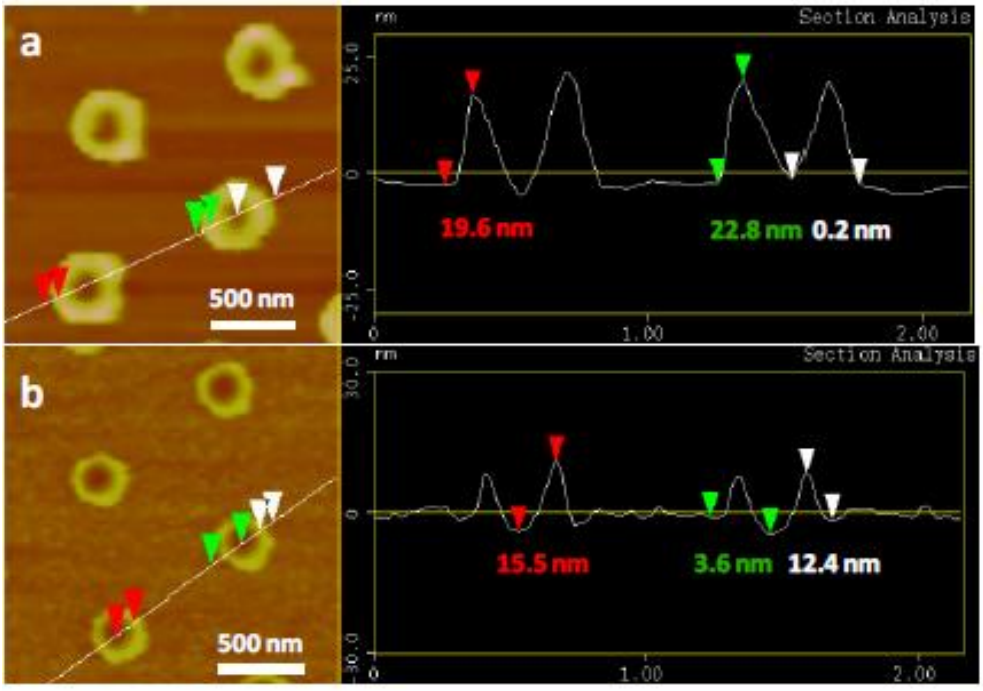

Figure 18. AFM height and cross-sectional analysis of OTS nanorings corresponding to 900 nm PS particles with different CVD time, (a) 5 min (b) 720 min.

Numbers marked in the cross-sectional analysis are the vertical distance for each marked point. Z-range for both images is 60 nm. [68]

In this study, we had a lot of failed experiments in which none or just the footprint of nanorings pattern was observed on the substrate after the removing the spheres from the silicon wafer. To investigate the cause of the failed experiments, removed PS spheres were studied with SEM and TEM. An alternative way to remove the PS particles from the silicon wafer is to use an adhesive tape beside sonication. [69] Figure 19a shows the SEM images of the 300 nm PS spheres removed with scotch tape from the substrate after the reaction, and Figure 19b shows TEM image of 900 nm PS particles after removal using sonication in 1:1 volume ratio of ethanol and water. The solution containing the removed particles then centrifuged for 5 min at 15000 rpm. The separated palate centrifuge tube was diluted with water and was placed on TEM grid for imaging. The OTS rings on the PS particles can clearly be spotted on both SEM and TEM images, and it shows that the OTS rings were removed from the surface with the PS particles during the particle removal process. It shows that with thicker rings OTS sometimes has stronger adhesion with the particle compared to the silicon wafer substrate.

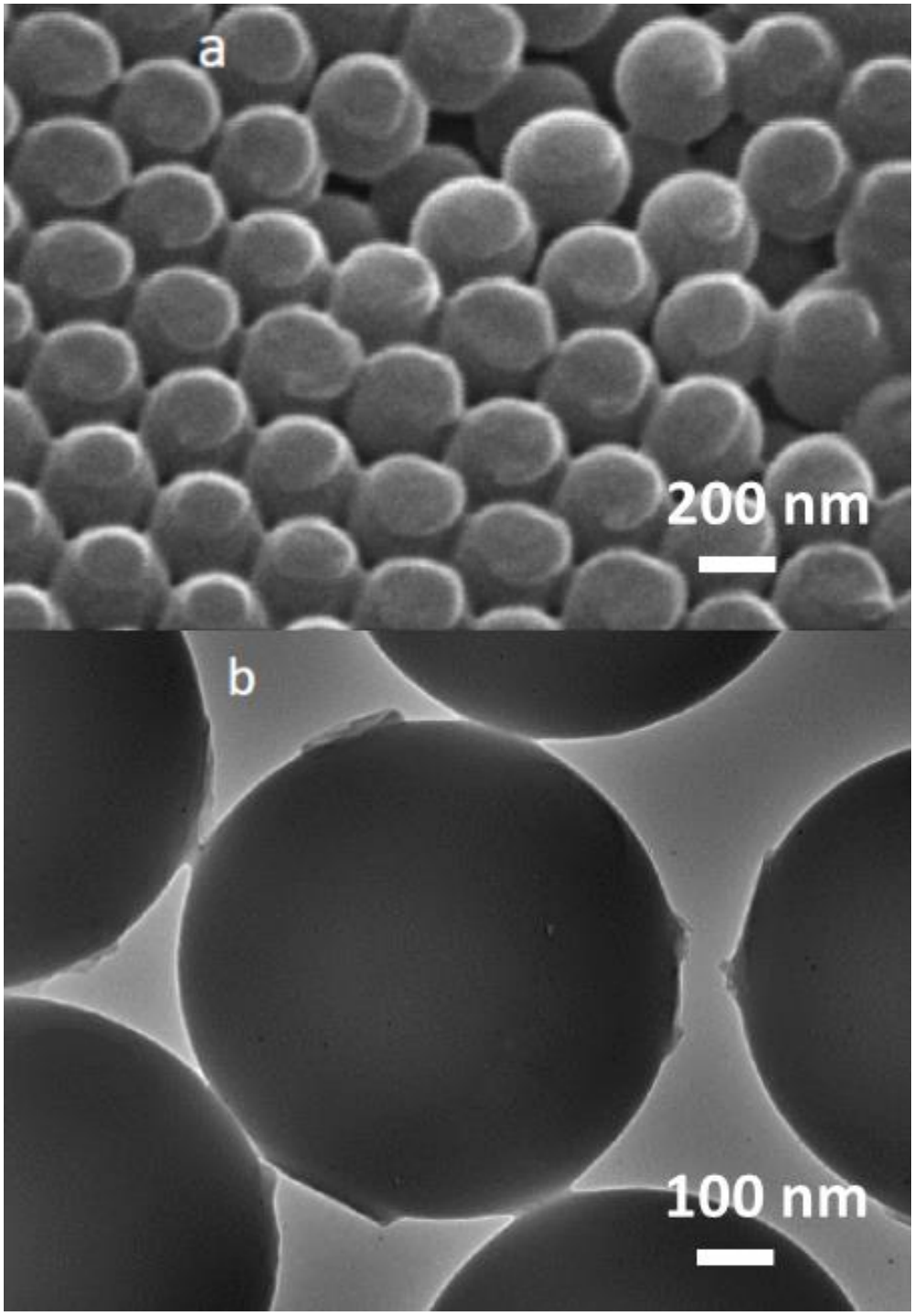

Figure 19. (a) SEM and (b) TEM images of removed from the substrate after reaction for (a) 300 nm and (b) 900 nm PS particles.

The next studied factor is relative humidity, while other factors were kept constant.

The experiments were done at room temperature (24 ºC), and the reaction time is 90 min

with 100 µL OTS introduced to the container. The reactor sizes are 0.13 and 5.2 L. The relative humidity was controlled with saturated salt solutions from 5% to 39%, 79%, and 98%. In Figure 20 OTS ring thickness is plotted against relative humidity for two different reactor sizes, for 900 nm PS particles. The data show that relative humidity has no significant effect on the ring thickness, although they show that in order to form supra-monolayer OTS rings, reactor size needs to be smaller. It is due to the sufficient OTS vapor pressure with the small reactor.

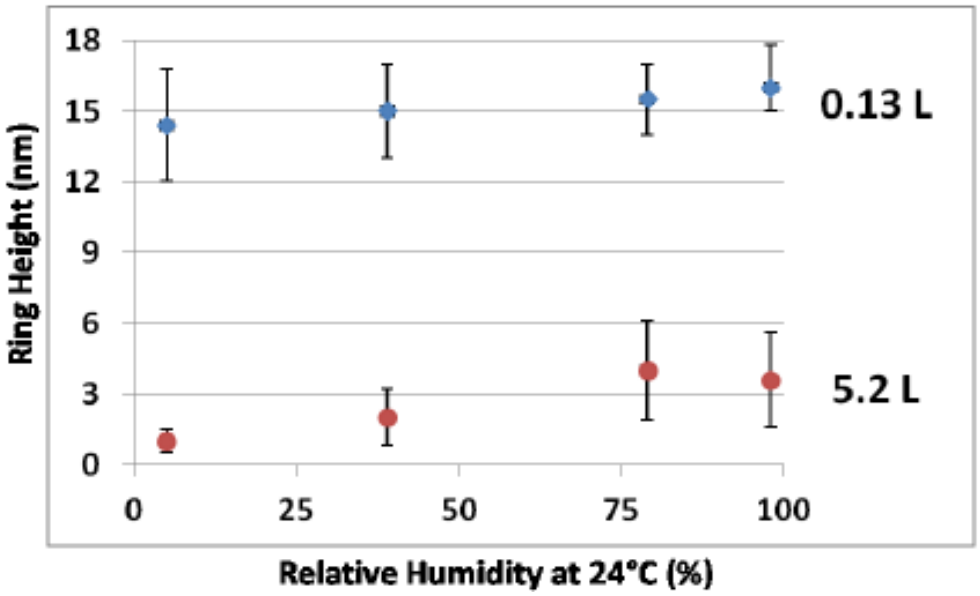

Figure 20. Nanorings thickness vs. relative humidity for OTS rings formed with 900 nm PS particles for 0.13 L and 5.2 L reactors. [68]

4.3.2 Organic NP deposition in OTS nanorings pattern

In the following section, the deposition of organic NP in OTS nanorings pattern will be explained. Three hydrophobic organic crystal were used, aspirin, n-docosane, and clarithromycin. The selected OTS rings formation conditions are, 90 min reaction time, 0.13 L reactor, and 5% relative humidity. Experiments had been done for both 900 nm and 300 nm PS particles. Before the NP crystal deposition, the successful pattern formation

was checked with AFM. Figure 21 shows the AFM height images of the nanorings pattern before the NP deposition. The nanorings thickness is 14.4 ± 2.4 nm with 379 ± 46 nm in outer diameter and 160 ± 32 nm inner diameter for 900 nm PS particles. The thickness is 10.3 ± 2.2 nm with 121 ± 25 nm in outer diameter and 56 ± 14 nm inner diameter. (N=50) The cross-sectional data shows uniform spherical ring structure.

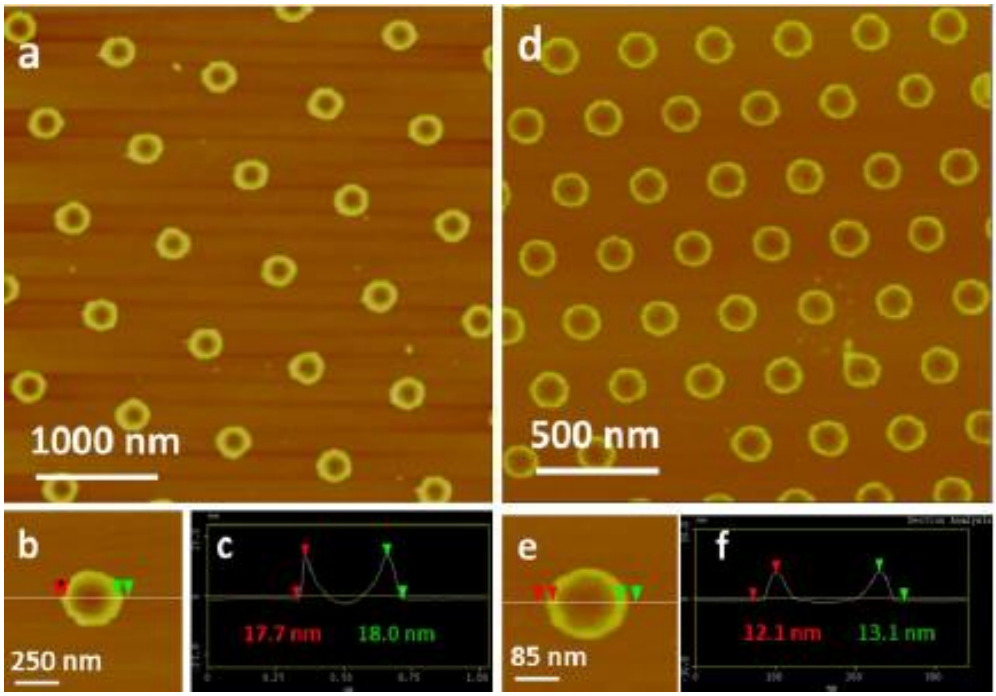

Figure 21. AFM height images of OTS nanorings patterns for 900 nm (a-c) and 300 nm (d-f) PS spheres. (c) and (f) are the cross-sectional analysis of a single ring as an example.

In the next step, n-docosane was deposited into the nanorings with recrystallization technic. Diethyl ether was used as the solvent because it is more volatile and the resulting film is more uniform compared to other solvents. The n-docosane deposited film was heated above the melting point (43 ºc) and quickly was cooled down to -20 ºC to recrystallize. The deposition quality is greatly affected by the concentration of n-docosane. While all the surface was covered with a thick n-docosane layer with the concentration above 7 mM, almost no crystal was deposited with the concentration below 0.7 mM. Figure

22 shows the AFM height images and cross-sectional analysis of the deposited n-docosane crystals in OTS nanorings for 900 nm PS spheres for different concentration of n-docosane. As it can be seen in the data the size of deposited n-docosane NP in the rings were increased with the concentration. Small uniform NPs were deposited in the nanorings with 1 mM n-docosane.

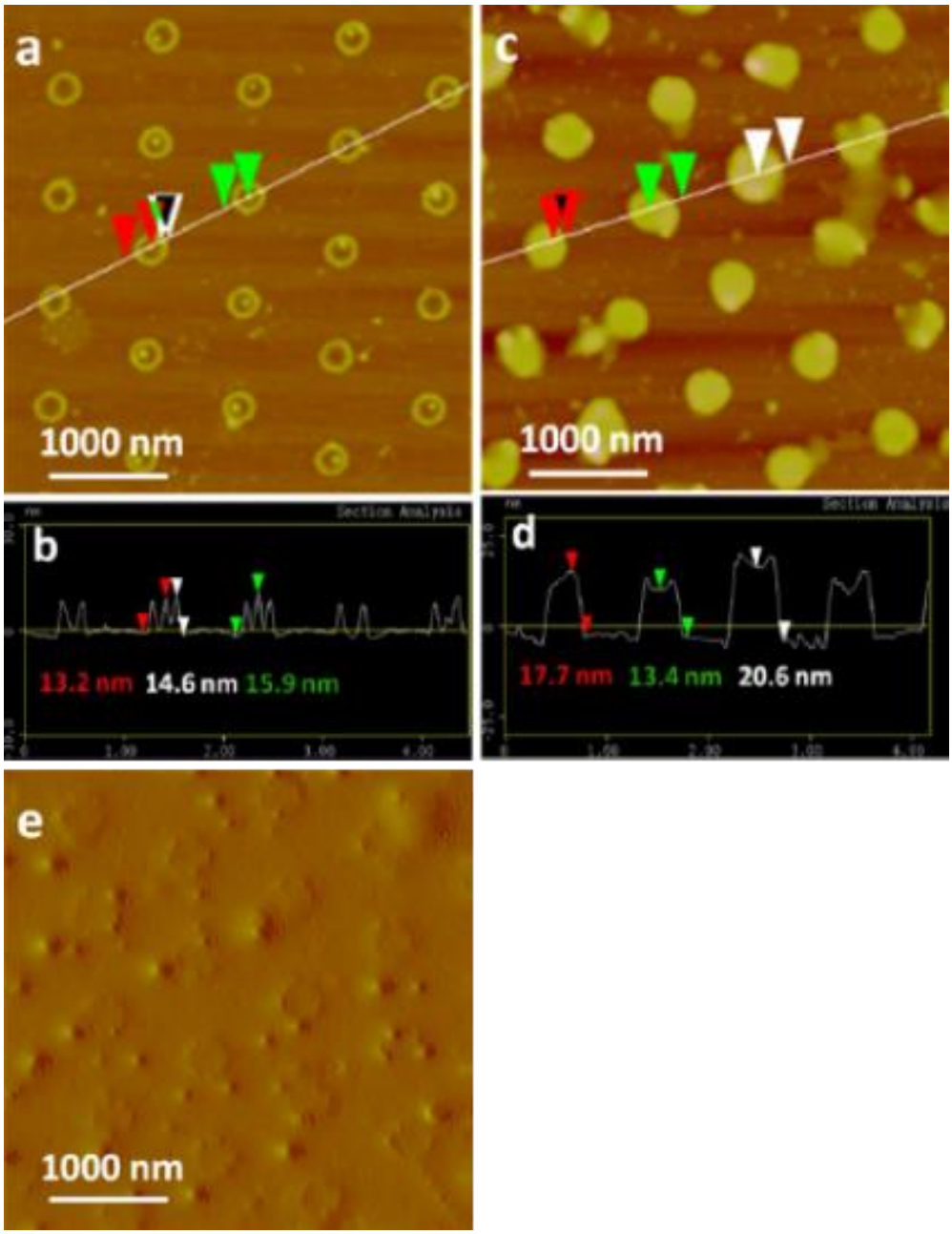

Figure 22. AFM height images of deposited n-docosane in the nanorings pattern for 900 nm PS spheres template. (a) and (c) are the height images of the deposited NPs for (a) 1nM and (b) 3.5 mM and (e) amplitude image for 7mM n-docosane. (b) and (d) are the cross-sectional analysis of the above image.

The rings were completely filled with a concentration of 3.5 mM n-docosane and all the substrate was covered with a layer of n-docosane with the concentration of 7mM. The data analysis demonstrates a uniform deposited of n-docosane NPs in the rings that

clearly shows the OTS nanorings pattern can control the organic crystal deposition and this process has the potential to be employed as an organic NPs manufacturing method.

Beside n-docosane, two other organic materials were tested for the inside ring deposition: clarithromycin and aspirin. In this section, fast evaporation technic was used for the organic NP deposition on the nanorings pattern. Similar to recrystallization technic the governing factor for the deposition quality is the concentration of the organic material. Diethyl ether was used again to serve as the solvent because of the fast evaporation. Figure 23, shows the 900 nm OTS nanorings maximum filling with 0.7 mM n-docosane(a), 0.2 mM clarithromycin (b) and 3 mM aspirin. Aspirin deposition NP size-dependent to the concentration for 300 nm and 900 nm OTS nanorings were demonstrated in Figure 24 and Figure 25 respectively and calculated NP volumes were plotted in Figure 26, and the data shows a linear relation between the deposited aspirin NP and concentration for both cases.

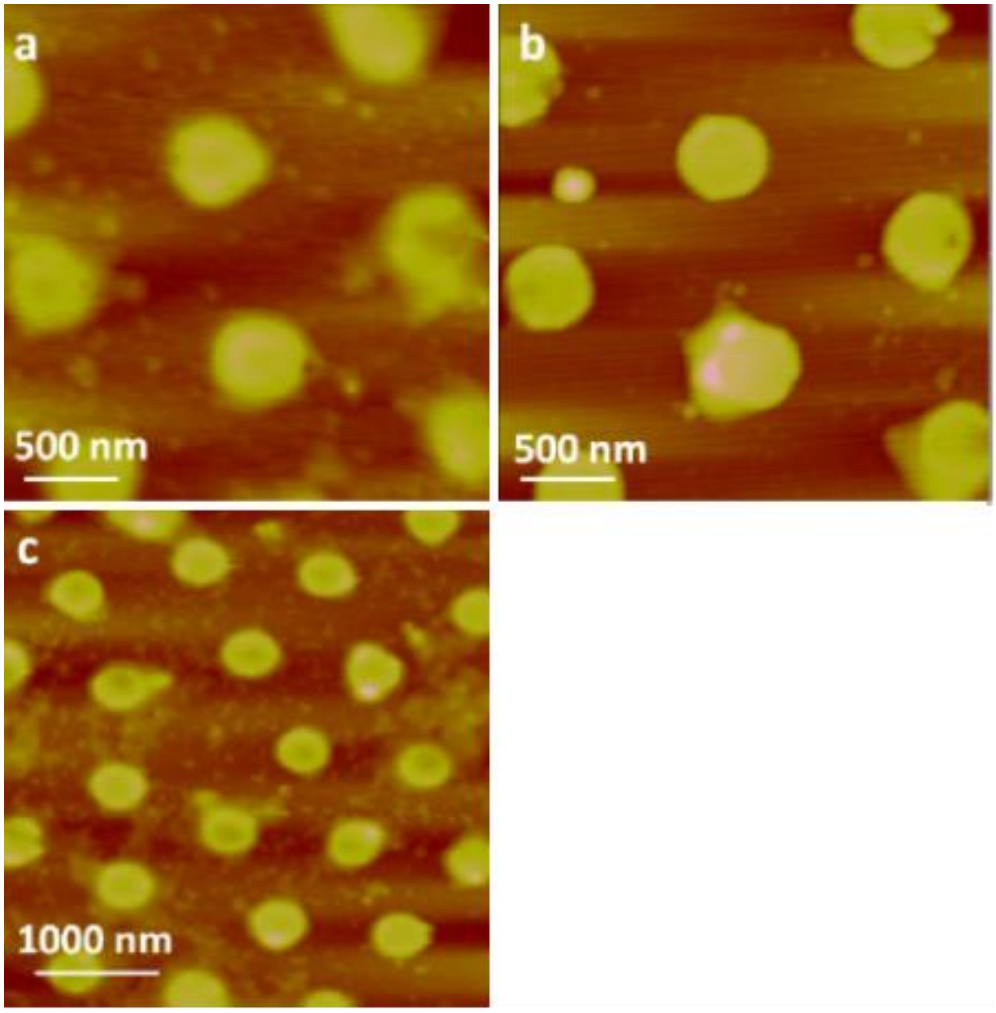

Figure 23. AFM height images of OTS nanorings template for 900 nm PS sphere filled with (a) n-docosane (b) clarithromycin and (c) aspirin and concentrations are 0.7, 0.2 and 3 mM respectively. Z-range is 60 nm for all the images.

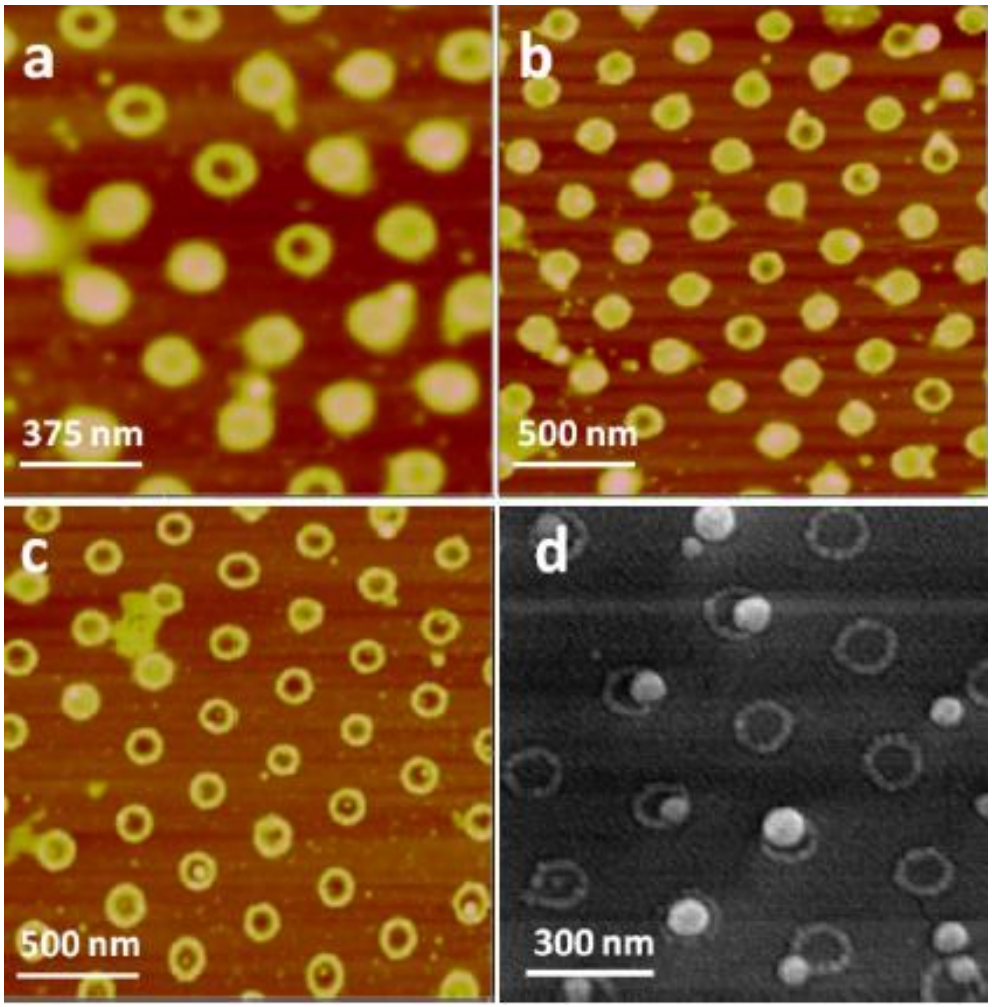

Figure 24. AFM height images of deposited aspirin in 300 nm PS particle nanopattern for (a) 1 mM (b) 0.3 mM and (c) 0.1 mM aspirin solutions Z-range is 20 nm. (d) FE-SEM image of (c). [68]

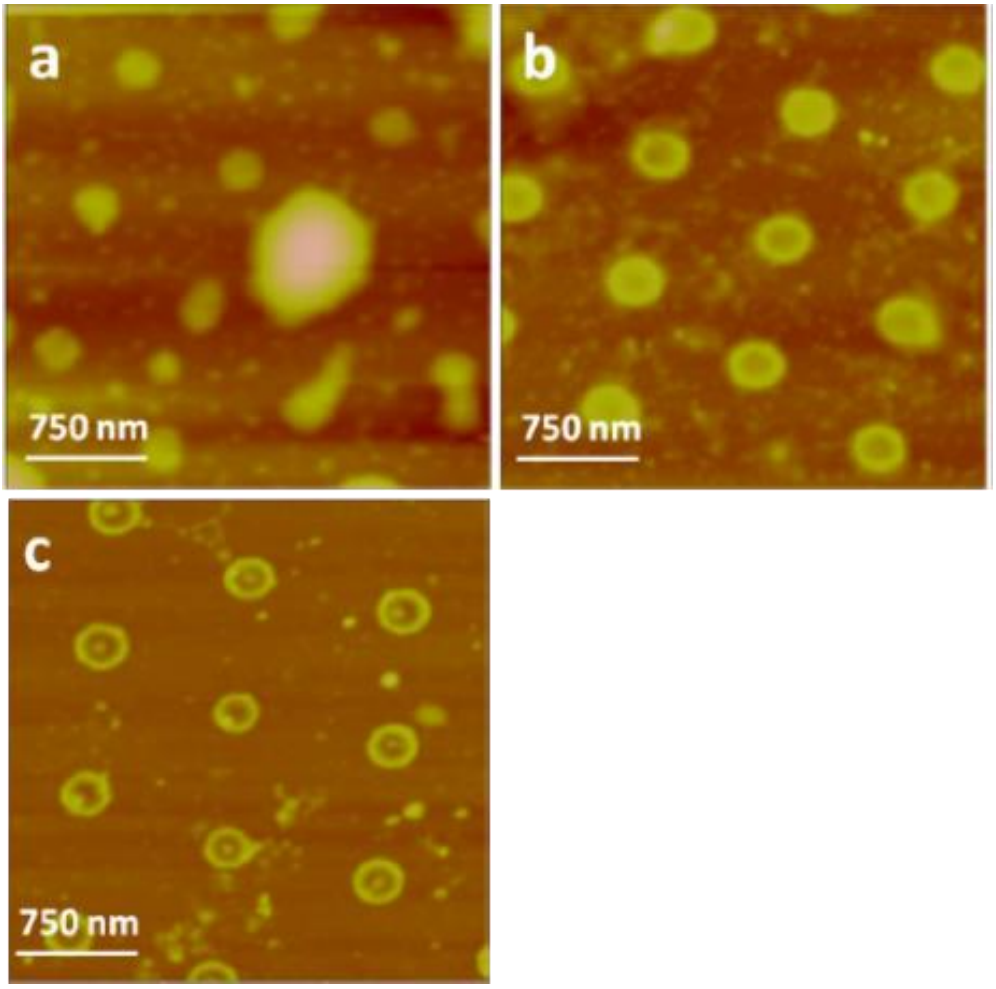

Figure 25. AFM height images of deposited aspirin in 900 nm PS particle nanopattern for (a) 1 mM (b) 0.3 mM and (c) 0.1 mM aspirin solutions Z-range is 60 nm.[68]

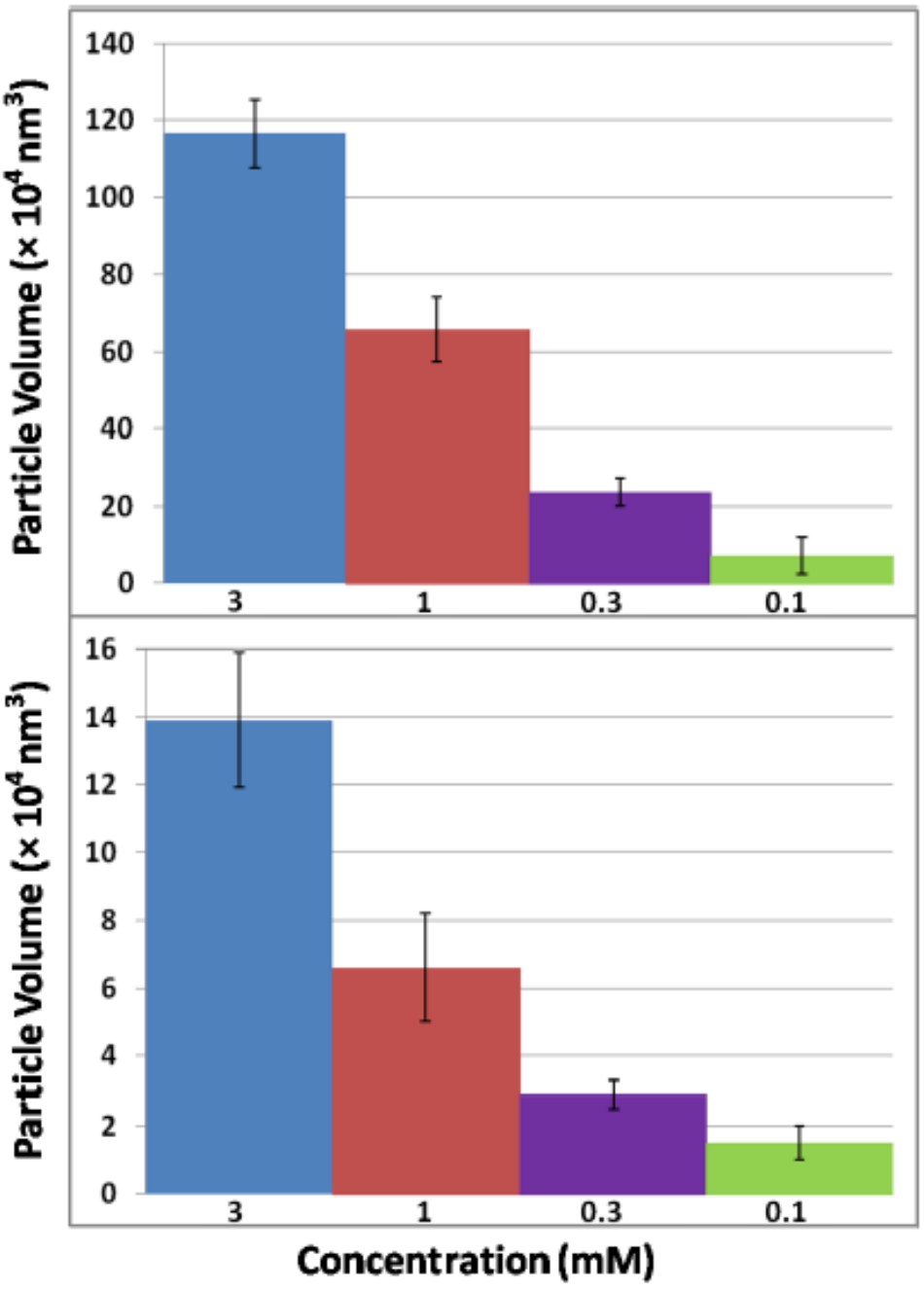

Figure 26. Deposited aspirin NP size-dependent on the concentration of the solution for (a) 900 nm OTS nanorings and (b) 300 nm OTS nanorings. [68]

4.4 Conclusion

This study had investigated the optimum conditions to produce nanorings and the use of nanorings to deposit organic NPs. PS spheres of 300 nm and 900 nm were used in

particle lithography, combined with the CVD method, to produce a uniform supra-monolayer nanoring pattern on the silicon substrate with thickness up to 23 nm. It was determined that the nanoring growth is mostly happening at the beginning of the reaction and also the humidity does not play a major role in the growth of the rings, but the reactor size is very influential on the final thickness of the nanorings. The produced OTS nanoring pattern shows great stability on multiple uses for the deposition of organic NPs, and multiple rinsing with solvents. The nanorings were served as nano-flasks for the deposition of a variety of organic NPs like aspirin, n-docosane, and clarithromycin. The process showed an almost perfect deposition of the organic NPs inside the nanorings with a uniform size suggesting that the deposition is controlled by the OTS nanorings. The size of the deposited NPs or the filling ratio was easily controlled with the concentration of the organic solution. This method of deposition has drug delivery applications because of the uniform small size of organic NPs.

CHAPTER 5 ELECTRODEPOSITION OF THE AuNPS ON THE HOPG ELECTRODES WITH CONTROLLED MORPHOLOGY

5.1 Introduction

In the following chapter, the controlled electrochemical synthesis of AuNPs will be investigated. In the next chapters, electrochemical crystallization of organic crystals on synthesized AuNP seeds based on SMN theory will be explained. The selected organic crystals are tetrathiafulvalene (TTF) and potassium tetracyanoplatinate bromide trihydrate (KCP) also known as Krogmann's salt. Lastly, the formation of faceted AuNPs using colloidal and electrocrystallization methods and the possible use of these nanoparticles as seeds to controlled synthesis of TTF /gold nanohybrids will be investigated.

Precise control over metal nanoparticles shape and size recently has drawn a lot of attention due their applications in electronics, optics, and catalysis. [70-72] AuNPs are point of interest because of their high chemical stability and easy synthesis methods.[73] Electrochemical synthesis of AuNPs on HOPG substrate follows the Volmer-Weber (VW) island growth mechanism because of weak van der Waals' interactions. [74] Sphere-shaped AuNPs are the most common shapes of AuNPs because of their bio, chemical, and electronic applications. [75-78] Au nanorods are good candidates for optical applications such as photothermal and photodynamic therapies, because their optical absorption is tunable with their aspect ratio. Different shapes of AuNPs other than traditional sphere shape has a lot of potential applications in electron microscopy, optical imaging, homogeneous assays, solid phase assays, drug carriers, biosensing, plasmonic photothermal therapy, and surface enhanced Raman scattering. [79] However, because of the sensitivity, poor reproducibility and small scale production of the common producing methods, they are rarely being used. [80] Many research groups led the study on high volume production and

better synthesis methods of a variety of the metal nanoparticle shapes. Murphy et al. were able to produce up to 1 gram gold nanorods, with the controllable aspect ratio between 2 and 25. [81-82] All the developed methods are similar as they basically reduce metal salt with a reducing agent, and using a capping agent to control the shape of the produced particles. In this study, we introduce a more reliable method by employing the same principles to produce nanocube gold particles directly on the surface, electrochemically. [81] Many studies had been done on the electrochemical synthesis of metal nanoparticles and specially AuNPs. Penner et al. thoroughly investigate the electrodeposition of the AuNPs on HOPG. They were able to introduce a general method to study the effect of applied potential on the population of deposited particles, and they were able to produce monodispersed AuNPs, with control over their size and density. [83] In comparison between the two methods, one major factor that sets them apart is reaction time. Standard colloidal synthesis methods sometimes take up to 24 hr in order to produce size-controlled nanoparticles, which is 10 ms for the electrochemical method. In this section, the average AuNP sizes are determined using Nanoscope software for AFM images (N=80-100).

5.2 Experimental

5.2.1 Materials

All the materials were used as received; gold (III) chloride trihydrate (HAuCl4·3H2O, >99.9%, Aldrich), potassium chloride (KCl, ACS grade, Fisher Scientific), acetonitrile (CH3CN, 99.9%, Fisher Scientific), methanol (Mallinckrodt Chemicals, 100%), ethanol (Pharmco, 100%) and HOPG (Mikromasch, ZYB grade).

5.2.2 Electrodeposition of AuNP seeds on HOPG electrodes

AuNP was deposited on HOPG substrate by electrocrystallization method. PAP 263A electrochemical workstation (Princeton Applied Research) was used for all the experiments. The workstation is connected to the electrodes using a Signatone probe holder station. We are using a typical three-electrode system for electrochemical experiments: a working electrode, a counter electrode, and a reference electrode. HOPG serves as the working electrode; the counter electrode is a platinum wire, and quasi-reference electrode is a silver wire. All the potentials reported are in reference to saturated calomel electrode (SCE). A schematic of the three-electrode setup is demonstrated in Figure 27.

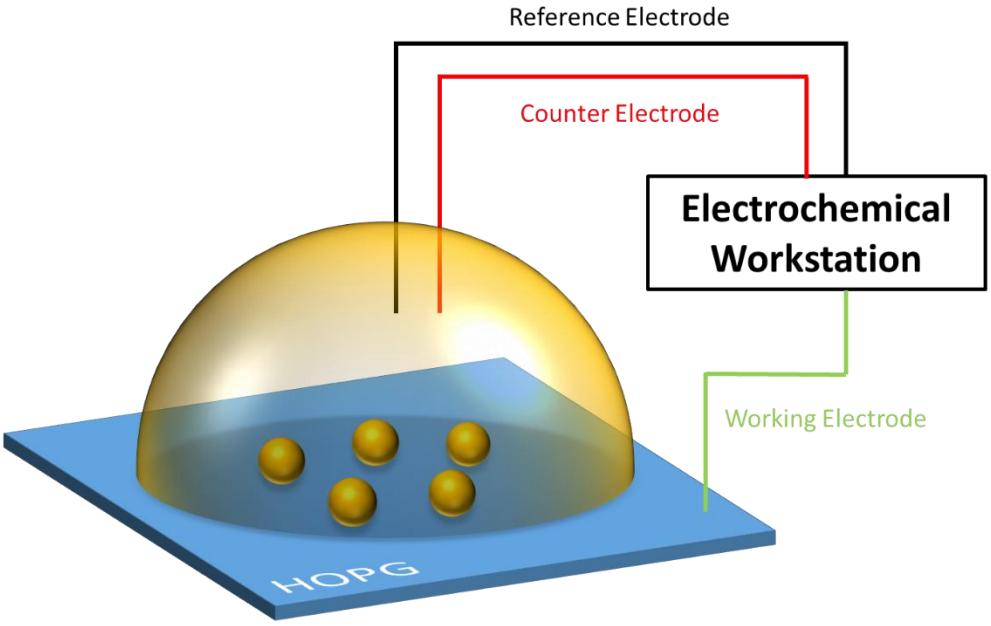

Figure 27. A schematic of three-electrode electrochemical cell for AuNP deposition on HOPG.

An aqueous solution of 0.05 to 10 mM hydrogen tetrachloroaurate ($HAuCl_4$) with 0.1 M potassium chloride (KCl) as the supporting electrolyte was prepared. AuNPs were deposited on HOPG substrate with reduction of $HAuCl_4$. For every experiment, the solution was purged with nitrogen to deoxygenize the solution, and the substrate was

cleaved with scotch tape. After the experiment, the substrate was rinsed with DI water and dried with nitrogen. One step method was used with the step time ranging from 10 ms to 10 s and the applied overpotential ranging from -0.9 V to -0.1 V. The electrochemical reduction reaction of the $HAuCl_4$ is:

$$AuCl_4^- + 3e^- \rightarrow Au(0) + 4Cl^- \quad \text{(Equation 11)}$$

The equilibrium reduction potential is 0.77±0.02 V that is calculated based on the Nernst equation, for [$AuCl_4^-$] (0.05 to 10mM) and [Cl^-] equal to 0.1 M:

$$E_{eq} = E_{Au(III)/Au(0)} = E^0_{Au(III)/Au(0)} + \frac{0.059}{n}\log\frac{\left[AuCl_4^-\right]}{\left[Cl^-\right]^4} \text{ (at 25 °C)} \quad \text{(Equation 12)}$$

5.3 Results and Discussion

5.3.1 Size variation of synthesized AuNPs

Cyclic voltammetry (CV) measurement was used to determine the suitable potential range for gold reduction based on equilibrium reduction potential. CV is significantly dependent on scan rate, in this case, the scan rate was fixed at 100mV/s for all the experiments, potential range is -0.5 to 1.5V and it was done for different concentrations of $HAuCl_4$ aqueous solution from 0.05 mM to 10 mM. Figure 28a demonstrates a comparison between obtained CV curves for six different concentrations of $HAuCl_4$. Reduction peak occurs in 0.2 – 0.5V and oxidation peak occurs in 1.0 – 1.2V. As the concentration of $HAuCl_4$ increases, the absolute value of the corresponding peak for both oxidation and reduction also increases while the peak for oxidation shifts to more positive potential and reduction peak shifts to more negative potential. Crossover potential (E_{co}) of forward and reverse scan is 0.66±0.02 which is close to calculated equilibrium potential. Current peak can be calculated with the following equation:

$$i_p = (2.69 \times 10^8)\, n^{\frac{3}{2}} A\, D^{\frac{1}{2}}\, C\, u^{\frac{1}{2}}$$ (Equation 13)

In this equation *n* is the number of transferred electrons, which in this case is 3. *A* is droplet area in cm^2, *D* is diffusion coefficient in cm^2/s, *C* is the concentration of analyte which in this case is $HAuCl_4$ in aqueous solution and *u* is scan rate in mV/s. To analyze the reaction regime, CV was done with different scan rates. Figure 28b is the plotted data of peak current versus scan rate that demonstrates a linear relationship between scan rate and current at the peak. This shows that the reduction reaction of Au^{+3} to Au is controlled by the diffusion of the gold ions from the bulk to the surface of the electrode in oppose to kinetic control. The diffusion coefficient can be calculated based on $i_p = (2.69 \times 10^8)\, n^{\frac{3}{2}} A\, D^{\frac{1}{2}}\, C\, u^{\frac{1}{2}}$ (Equation 13. For 0.5 mM $HAuCl_4$ concentration D is 5.6×10^{-6} cm^2/s which matches the diffusion coefficient value of the metal ions. The area is the droplet contact with the surface (A) for a 50 µL drop roughly to be 0.5 cm^2.

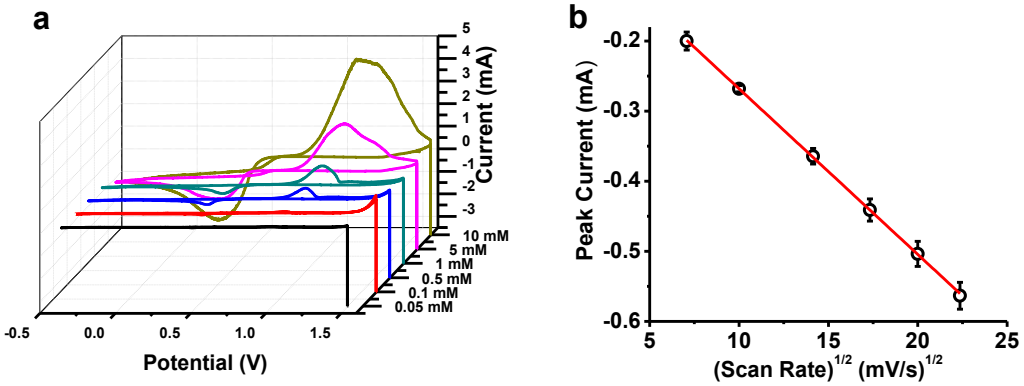

Figure 28. (a) cyclic voltammetry obtained for different concentration of $HAuCl_4$ from 0.05 mM to 10 mM (b) dependence of reduction peak current to different scan rates.[84]

Gold deposition morphology was studied as a function of $HAuCl_4$ concentration and deposition time. AFM and FE-SEM were used to determine the size, morphology, and density of the deposited gold particles on HOPG. Overpotential was fixed at -0.5V for all

the cases; the experiment had been done with 0.1mM, 0.5mM, 1mM, 5mM and 10mM aqueous solution of $HAuCl_4$. Figure 29 shows the AFM images of the deposited AuNPs on the HOPG substrate for the mentioned concentrations. Dimensions and density of the observed nanoparticles in all the cases is presented in Table 2. Particles density is determined by the average number of particles per μm^2 and the data shows that density is decreased with when the concentration increases. The covered surface area is estimated from the obtained AFM data on the sample. Deposition time is 0.01s for all the cases. AFM images show that the size of the AuNPs is increased when the concentration increases. The shape of the AuNPs also changes with concentrations above 1mM to a dendritic shape that matches the results from previous studies. [85] The smallest observed particle size for 0.1mM $HAuCl_4$ which dimensions are 32 ± 6 nm in width and 11± 2 nm in height. To study the seed curvature effect on crystal growth, smaller AuNPs were prepared by reduction of the lower concentration of $HAuCl_4$. These prepared AuNPs later were used as seeds for synthesizing of organic/inorganic hybrid structures.

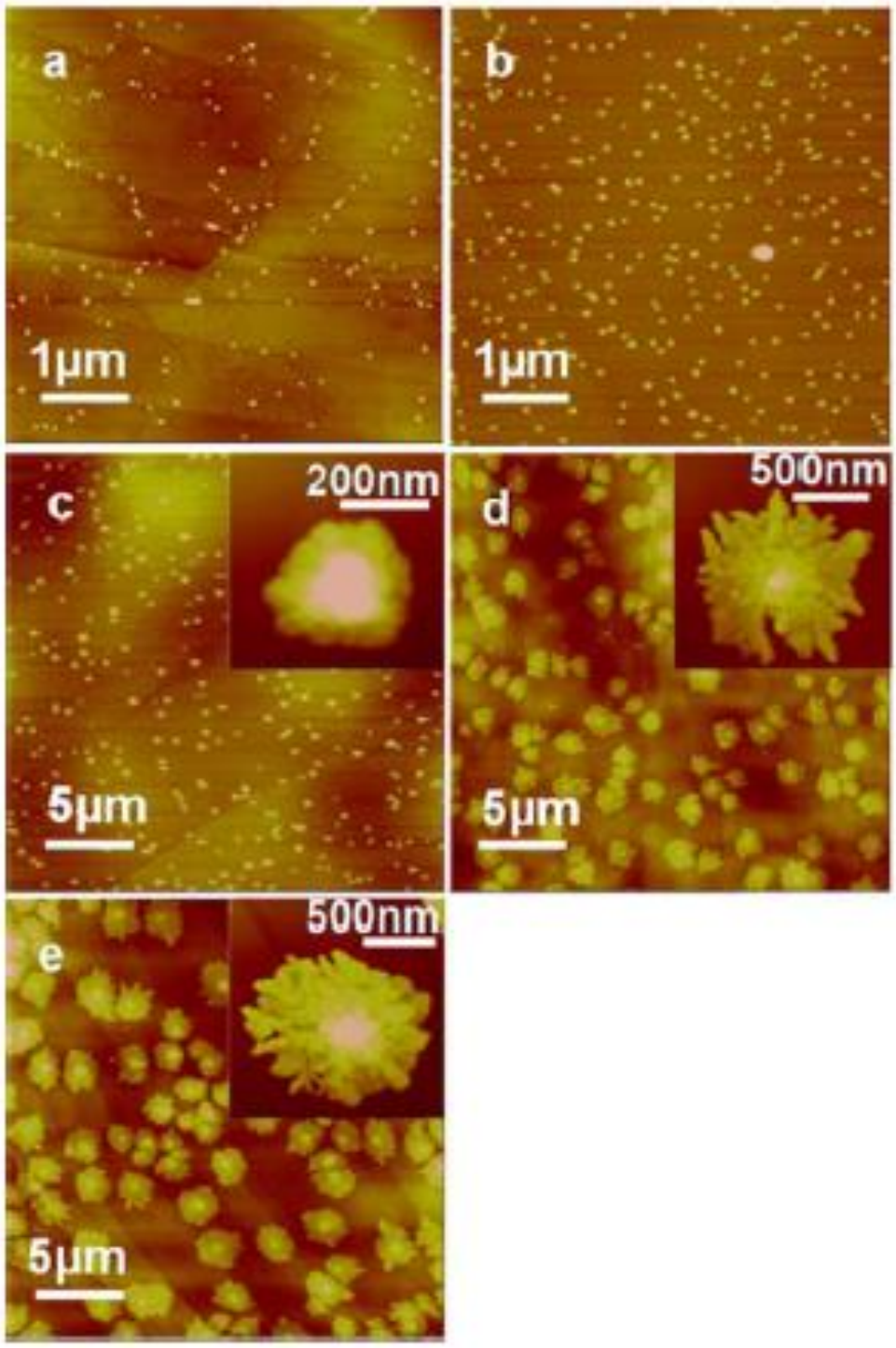

Figure 29. AFM height images of deposited AuNPs on HOPG with different concentrations. Applied overpotential for all the prepared samples is -0.5 V and deposition time is 0.01s. Concentration of $HAuCl_4$ is (a) 0.1mM (b) 0.5mM (c) 1mM (d) 5mM and (e) 10mM. [84]

Table 2. Average dimensions of deposited AuNPs on the freshly cleaved HOPG with different concentrations of $HAuCl_4$ observed from AFM images. [84]

$HAuCl_4$ Concentration (mM)	Particle size ($x10^{-3}$ μm/particle)	Particle Density (particle/μm^2)	Surface Area (cm^2)
0. 1	0.006 ± 0.004	13.0 ± 3.8	0.005
0.5	0.024 ± 0.008	13.3 ± 1.7	0.012
1.0	0.6 ± 0.3	0.98 ± 0.15	0.032
5.0	7.2 ± 5.9	0.28 ± 0.05	0.115
10.0	12.2 ± 8.0	0.22 ± 0.04	0.170

5.3.2 Shape variation of synthesized AuNPs

The data show that when the $HAuCl_4$ concentration is above 1mM, the deposited gold shows a dendritic shape. The dendritic shape is not an ideal shape for our study because of the non-uniform radius of curvature throughout the structure. In order to improve the nanoparticle shape, we used a two-pulse method to dissolve the dendritic parts of the particles[83, 86]. By using this method, we were be able to control the size and density of the AuNPs on the HOPG. The first step is the normal electrodeposition of gold that was described before, with an applied potential of 0.1V and 10ms deposition time as determined by the CV curve in the reduction region (reduction of Au^{+3} to Au(0)). In the

second step, the potential is in the oxidation region of the CV curve to dissolve the dendritic part of the AuNP (oxidation of Au(0) to Au^{+3}). After trial and error, we found that uniform shapes of the AuNPs could be produced with a potential of 1.0 V (in the oxidation region) and 5s deposition time. Figure 30 shows the AFM images of the side by side comparison of the one-pulse method and two-pulse method for 1mM and 10mM $HAuCl_4$ aqueous solution.

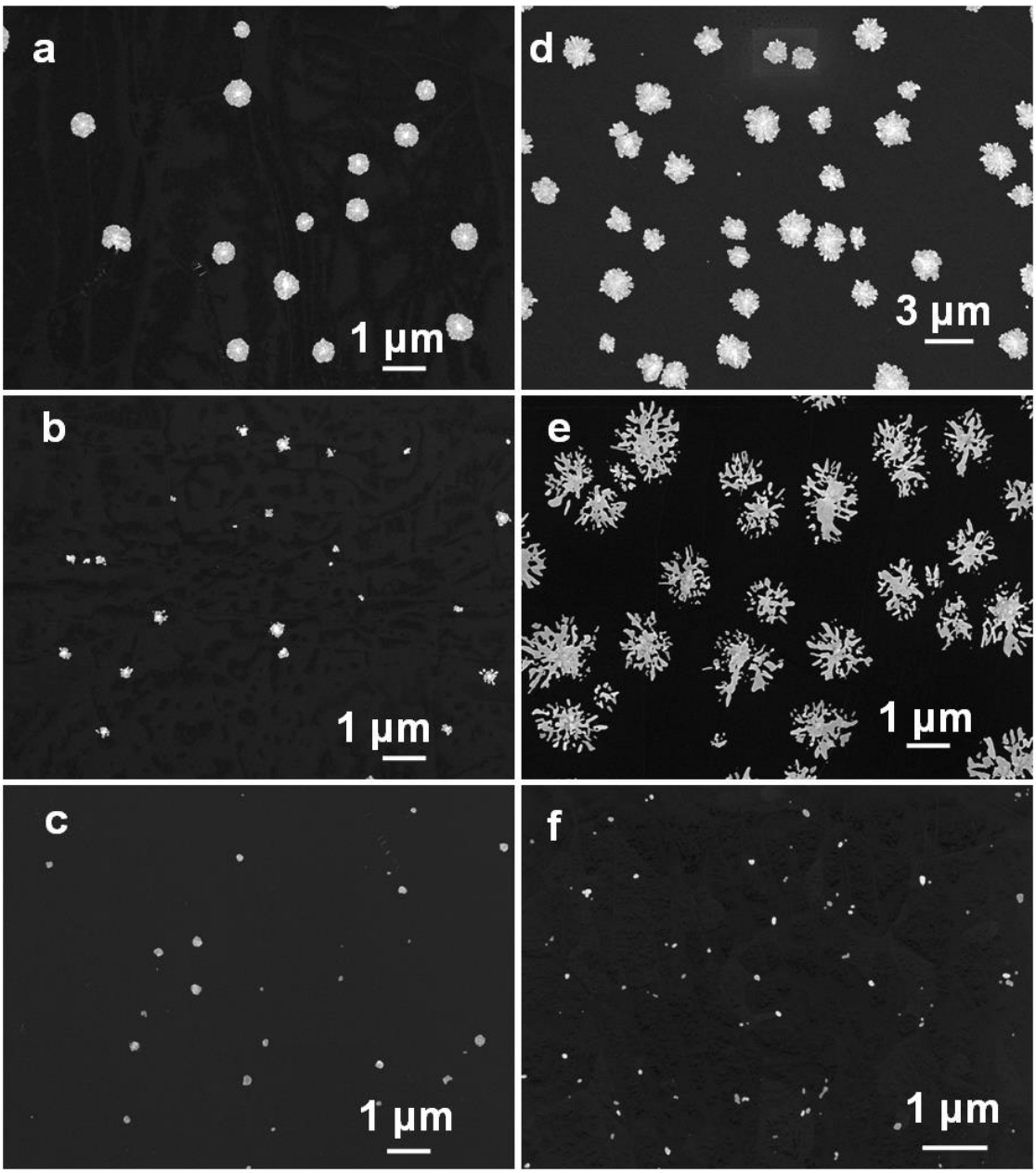

Figure 30. FE-SEM images of deposited AuNPs on freshly cleaved HOPG, left and right columns represent the images from the electrodeposition of 1mM and 10mM $HAuCl_4$ respectively (a) and (d) are images from a 1 step electrodeposition of 0.1V and 10ms, (b) and (e) represents the images from a two-step electrodeposition with second step of 1.0V and 1s. (c) and (f) represents the results of the second step of 1.0V and 5s.

Figure 30(a) and (d) are prepared as the previous method with one-pulse the potential of 0.1V and deposition time of 10ms, (b) and (e) are prepared with one step as the previous item and second step with potential of 1V and dissolving time of 1s , as it can

be seen the dissolution time was not enough to dissolve the dendritic parts of the particles completely, in (c) and (f) under the same conditions as the first step and second step with a potential of 1V and dissolution time of 5s shows that dendritic parts are dissolved completely. FE-SEM image data analysis shows that the average diameter of the AuNPs in Figure 30a is 495±128 nm and it decreases to 110±64 nm after 5s oxidation reaction (Figure 30f).

Next, the effect of deposition time and applied overpotential on electrodeposition of gold on freshly cleaved HOPG was studied. The concentration of $HAuCl_4$ was kept constant while the deposition time and applied overpotential varied. Figure 31 demonstrates the preliminary AFM images of electrodeposition of 0.1mM $HAuCl_4$ with applied overpotential from -0.1V to -0.5V and deposition time from 0.01s to 1s. As expected, with higher deposition time, the size of deposited AuNPs was increased but the average particle density was decreased. This can be due to Ostwald ripening meaning that the particles at growth phase migrate and form bigger and more stable particles; which will lead to a lower particle density.

Table 3. AFM data analysis of deposited AuNPs on HOPG depending on deposition time and applied overpotential. [84]

Overpotential (V)	Time (ms)	Particle height (nm)	Particle width(nm)	Particle Density (particle/μm^2)
- 0.1	10	18.2 ± 4.1	50.3 ± 11.1	4.9 ± 0.8
- 0.5	10	11.3 ± 2.1	32.3 ± 6.2	13.0 ± 3.8

- 0.5	100	17.9 ± 3.4	43.8 ± 8.2	6.2 ± 1.1
- 0.5	1000	20.0 ± 3.8	52.2 ± 7.9	3.9 ± 0.9
- 0.9	10	2.3 ± 0.6	34.4 ± 6.4	50.0 ± 5.2

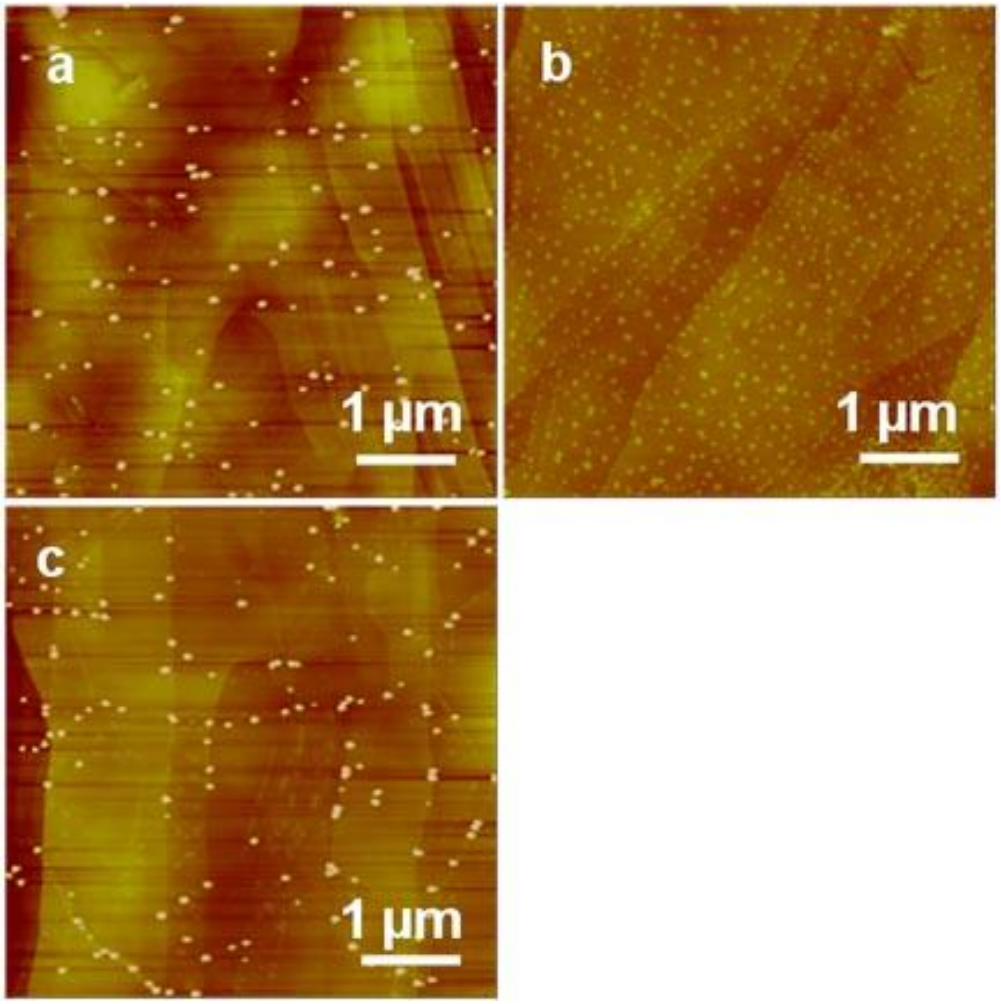

Figure 31. The effect of applied overpotential on electrodeposition of AuNPs on freshly cleaved HOPG with the following conditions for applied overpotential and deposition time respectively (a) -0.1 V, 0.01 s (b) -0.9 V, 0.01 s (c) -0.5 V, 0.01s. [84]

XRD was used to investigate the crystal shapes formed with electrodeposition of AuNPs on freshly cleaved HOPG. Figure 32 shows the XRD patterns of synthesized

AuNPs with different concentrations. XRD was done on bare HOPG, 0.1mM $HAuCl_4$, and 10mM $HAuCl_4$ aqueous solution. Overpotential was selected -0.5V with a deposition time of 0.01s. XRD patterns of bare freshly cleaved HOPG does not show any peaks. For 0.1mM $HAuCl_4$ sample {111}, {200} and {222} crystalline planes can be seen respectively at 38°, 44° and 82° 2θ values. The {222} peak for 10mM $HAuCl_4$ sample is divided into two peaks because of the dendritic shape of the nanoparticles in this case.

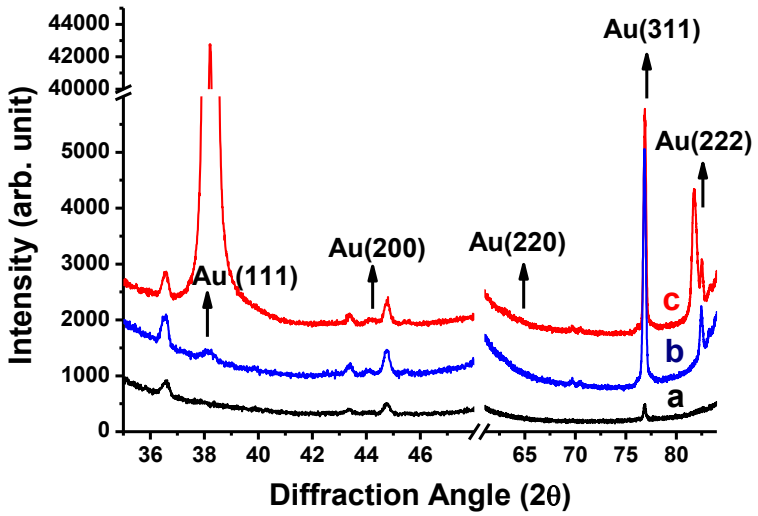

Figure 32. XRD patterns of (a) Bare HOPG (b) Electrodeposited AuNPs from 0.1mM $HAuCl_4$ aqueous solution (c) Electrodeposited AuNPs from 10mM $HAuCl_4$ aqueous solution.

The very high intensity of {111} planes for dendritic nanoparticles shows this face as the prominent face in the particles. These crystalline shapes were also confirmed by the FE-SEM images of the AuNPs, Figure 33 demonstrates the different crystal shapes of electrodeposited AuNPs on HOPG. As it was described in section 2.1.3, the {111} plane has the lowest surface energy. The most stable shape will have the lowest energy surfaces, but at the same time, a single crystal with the next higher surface energy ({100}) has lower surface area. Therefore, based on Wulff's theorem, the most stable crystal structure will

have a combination of both faces. Figure 33 is the FE-SEM images of different shapes which were produced randomly on HOPG substrate. To have better control over the shape of AuNPs, a new method will be proposed in next section that employs the shape control technic borrowed from the colloidal synthesis method.

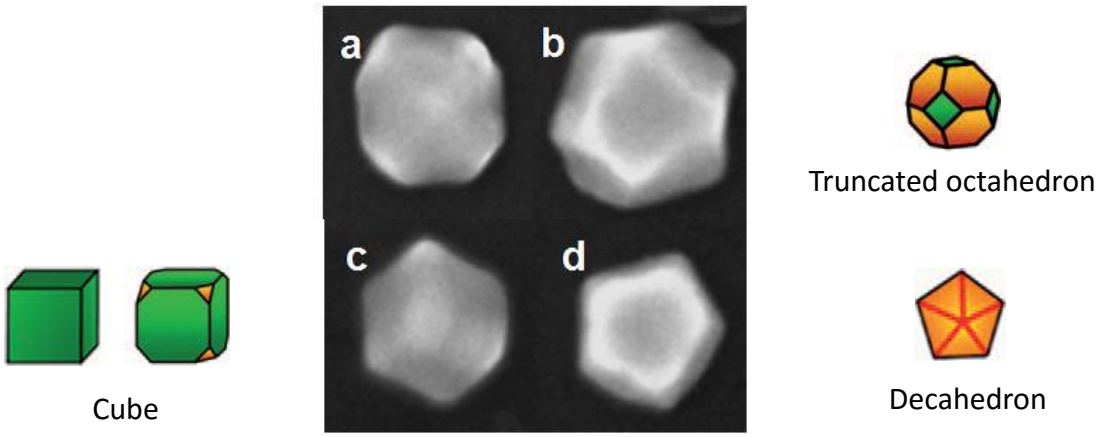

Figure 33. FESEM images of different crystal shapes observed with electrodeposition of AuNP on HOPG [84] and schematic crystal shape of the crystals from literature[17]. Green surface represents {100} plane and orange represents {111} plane.

5.3.3 Introducing a novel method for cube AuNP synthesis

In the previous section, the electrochemical synthesis of spherical and dendritic AuNPs was described. In this section, we are going to introduce a new electrochemical method to produce cube-shaped AuNPs.

Capping agents have been widely used to produce a variety of different shapes of metal nanocrystals based on colloidal chemistry and the shapes include cube, [80] octahedron, [87] tetrahedron, [88] decahedron, [88] icosahedron [89] and others. A capping agent can be chemically reactive to a specific facet of a crystal and, therefore, can change the free energy of that facet. The free energy change then results in the shape change as predicted by the Wulff theorem (Figure 34). [17]

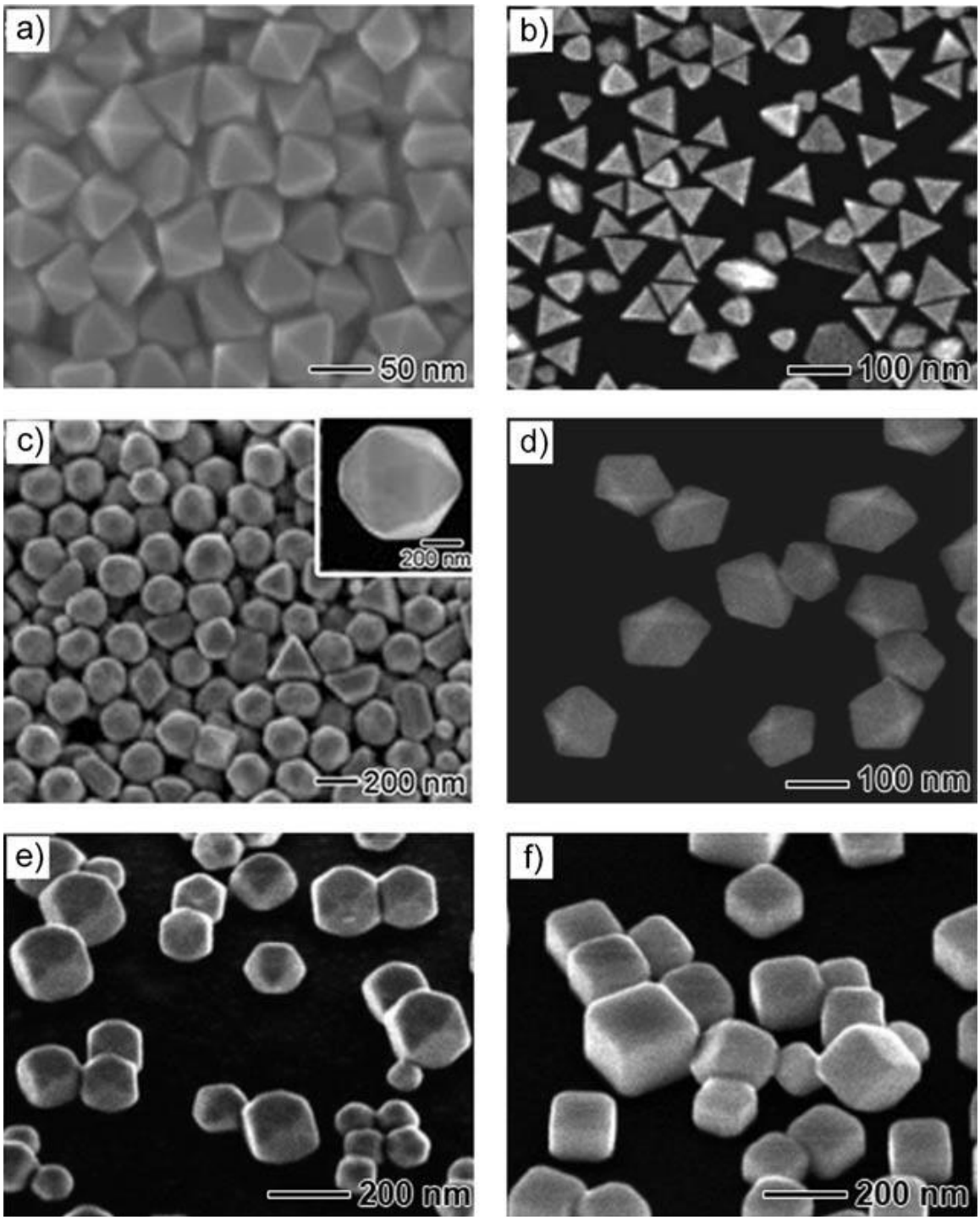

Figure 34. SEM images of different shapes of the AuNPs prepared by different groups with colloidal synthesis method (a) octahedron [87] (b) truncated tetrahedron [88] (c) icosahedron [89] (d) decahedron [88] (e) truncated nanocube [80] and (f) cube. [80]

Since the basis of nucleation in electrocrystallization method and colloidal method are the same, this technique can be employed to control the shape of the AuNPs deposited

electrochemically on freshly cleaved HOPG electrode. We hypothesize that by adding PVP to the $HAuCl_4$ solution deposition of gold will be on {100} face. [21, 80, 90] Therefore, the final shape of the crystal would be a cube or truncated cube. By varying the PVP concentration, we can control the shape of the formed AuNPs. The concentrations, applied potentials and deposition times can be adjusted according to the results. Next we will use the synthesized AuNPs with controlled shape and size as the nucleation seeds for KCP nanocrystal growth to study the effect of different seed shapes on the nucleation of the KCP nanocrystals. It is expected that nanorods grow on the edge of the faceted gold nanoparticles because of the higher surface energy compared to the dominant faces.

AuNPs were synthesized on freshly cleaved HOPG by electrocrystallization method. A solution of 10 to 1 mM hydrogen tetrachloroaurate ($HAuCl_4$), 0.1 M KCl as supporting electrolyte and 0.15 M of polyvinylpyrrolidone (PVP) as the capping agent in DI water was prepared. PVP oxygen atoms will form strong bonds with {100} facets of Au, therefore, the gold atoms would add preferentially to {111} facets and then migrate to face edges resulting in the domination of {100} facets and the expected final shape will be nanocubes made of largely {100} faces. [80] For 10 mM concentration of $HAuCl_4$ cube-shape AuNPs were not observed, but the capping agent dramatically changed the shape of the AuNPs from dendritic shape to symmetrical sphere shape. The size of observed AuNPs for 10mM $HAuCl_4$ is 1.04 ± 0.20 µm . Figure 35 shows the morphology change of the gold nanoparticles for 10mM $HAuCl_4$ solution before and after adding the capping agent. Every other condition was kept constant for both experiments. Particle density is 0.021 ± 0.015 particle/µm^2 that is reduced from 0.220 ± 0.04 particle/µm^2 for PVP free experiment.

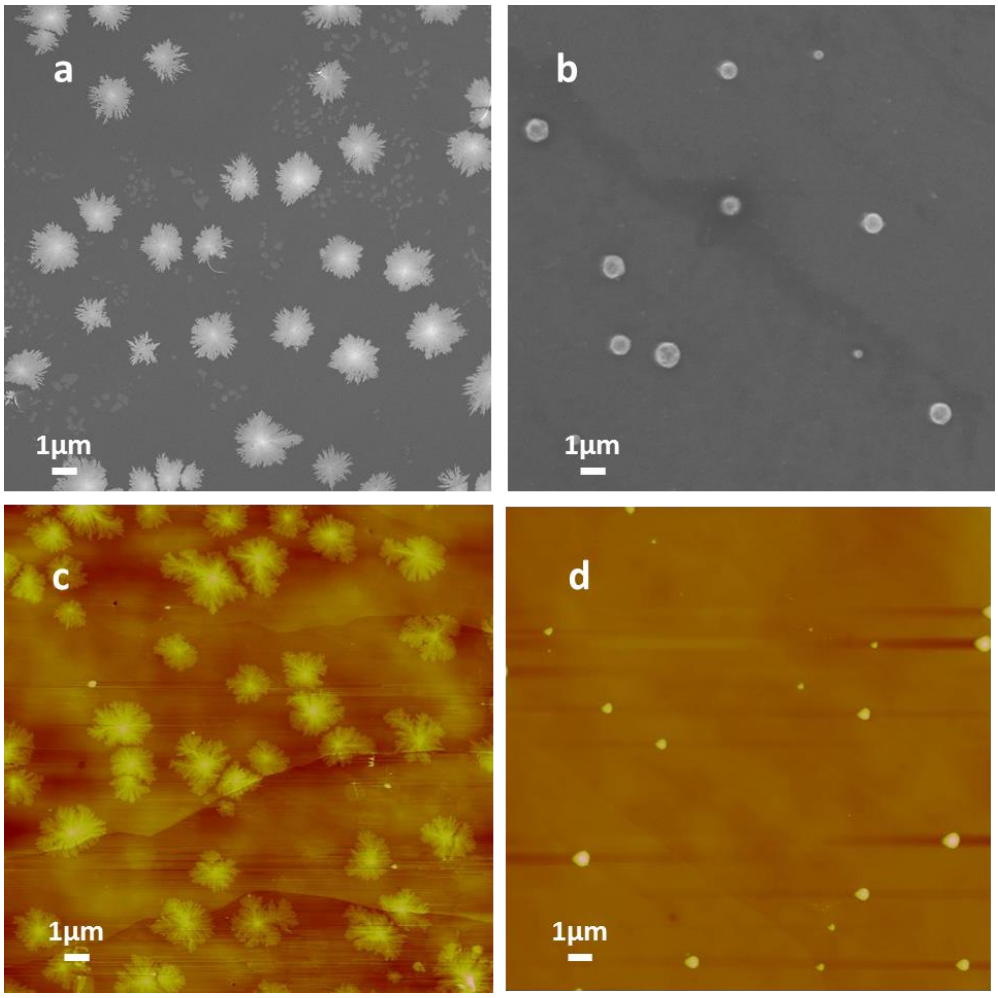

Figure 35. FE-SEM and AFM height images of electrodeposited AuNPs on freshly cleaved HOPG from (a) , (c) 10 mM $HAuCl_4$, 0.1 M KCl (b) , (d) 10 mM $HAuCl_4$, 0.1 M KCl, 0.1M PVP. Applied overpotential for both images is -0.5 V and deposition time are 10ms.

In order to achieve our goal to control the shape of the particles the concentration of $HAuCl_4$ was reduced to 1mM. Other parameters were kept the same as the previous experiment. The results show well-defined cube gold nanoparticles as it was expected. Figure 36 shows the SEM images of the observed cube AuNPs. The composition of the particles was confirmed by EDS. The average width of cubic AuNP is 106 ± 20 nm compared to results for traditional AuNP particles synthesized in the same condition that is 155 ± 11 nm.

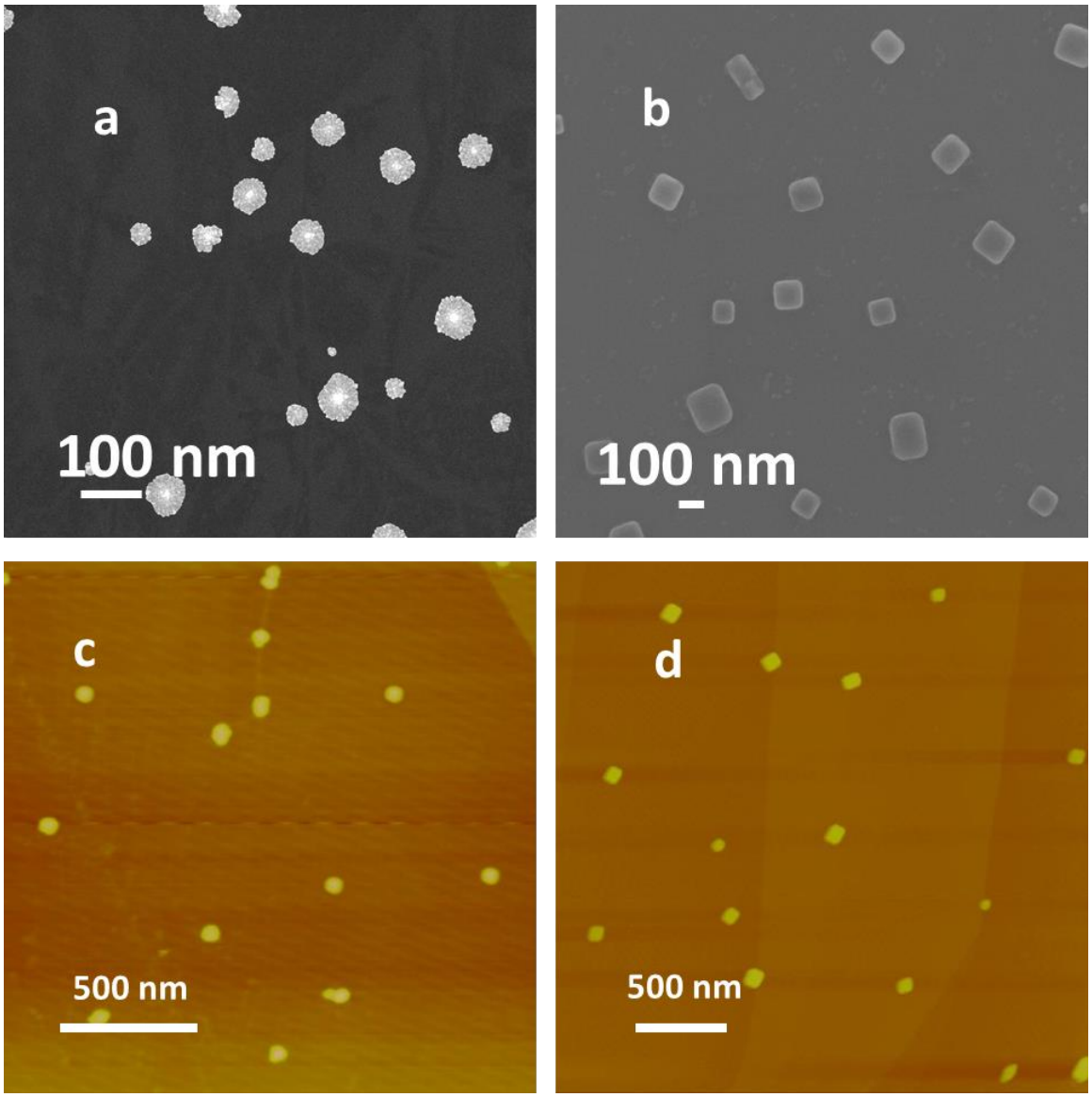

Figure 36. FE-SEM (top) and AFM height (bottom) images of (a),(c) AuNPs produced with the traditional electrochemical method on HOPG (b),(d) cube shape AuNPs synthesized with the modified electrochemical method.

To analyze the height of the particles, cubic AuNPs were also studied with AFM sectional analysis and the results for are shown in Figure 37. The average nanoparticle size is 21.2 ± 0.4 nm, which is decreased by 65% compared to regular AuNP in the same condition. (60 ± 30 nm). Based on the results the overall size of the cubic AuNPs will decrease, compared to traditional AuNPs. We assumed that the size of AuNPs will be

controlled by diffusion and by adding the high concentration PVP, the mass transfer coefficient for gold ions will be decreased; therefore, the size of the AuNP will be smaller.

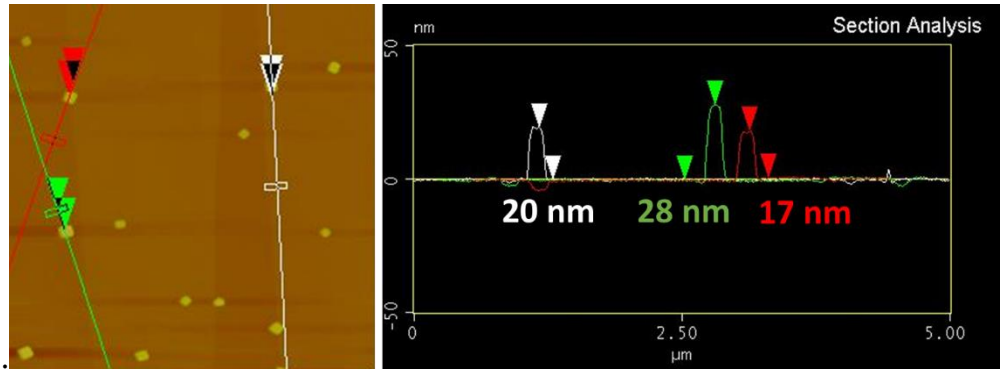

Figure 37. AFM section analysis for cubic AuNP. Concentration of the solution is, 1mM $HAuCl_4$, 0.1 M KCl, and 0.15 PVP

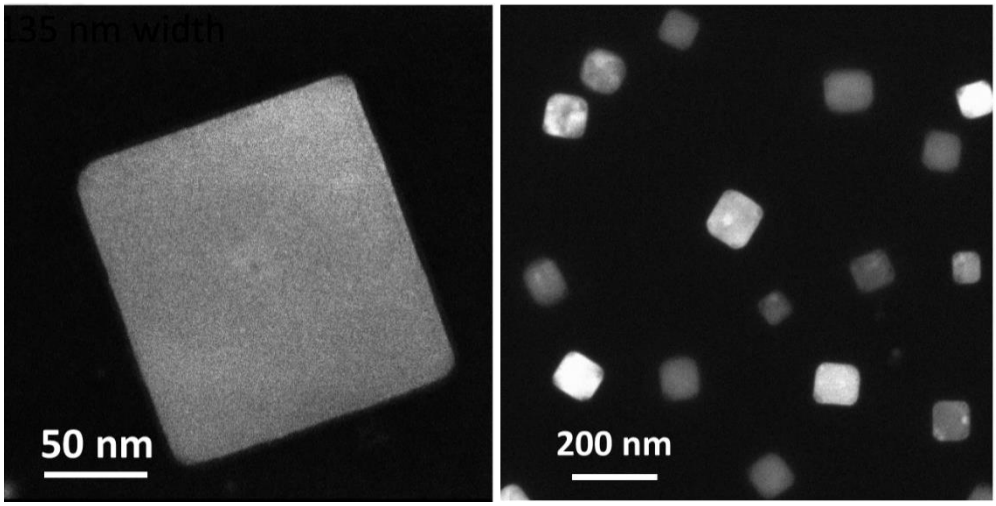

Figure 38. TEM images of the nanocube synthesized electrochemically on a TEM grid.

We hypothesize that by adding the capping agent (in this case PVP), the surface energy for {100} facets would be lower due to the bond between the oxygen atom in PVP and this face. Therefore, we expected to see the domination {100} facet in the final shape of the crystal which is a cubic shape; and the results match our prediction of the controlling the crystal shape.

5.4 Conclusion

This work demonstrates the methodology to control the morphology of AuNPs based on SMN theory via electrochemical methods. We were able to control the size of the AuNPs using the electrochemical methods by changing the concentration of Au^{+3} in the solution. Other factors like deposition time and overpotential were also investigated and the results show that the most effective governing factor on the size of the synthesized AuNPs is the concentration. We were able to change the shape of AuNPs by a two-step method from the dendritic shape in higher concentrations to a spherical shape. Furthermore, we were able to control the shape of the AuNPs using a capping agent PVP. Using this method cube AuNPs were formed directly on the substrate. The cube-shaped AuNPs can enable us to study the area confinement effect of seed-mediated nucleation and better control of the nanorod orientation nucleated from a well-defined facet in our future studies.

CHAPTER 6 ELECTROCRYSTALLIZATION OF $(TTF)Br_{0.76}$ NANORODS ON AuNP DECORATED HOPG

6.1 Introduction

This chapter focuses on the synthesis of organic/inorganic materials with electrochemical methods. Synthesis of organic/inorganic hybrids is based on seed-mediated nucleation (SMN) method which was explained in Chapter 2. Different characteristics of the nanoconfinement including the size of the seeds, curvature effect and separation distance and controlling parameters on size and shape of the nanocrystals will be addressed.

Nanostructures are defined as the structures that have at least one dimension lower than 100 nm and have interesting properties compared to their bulk counterparts.[91] 1D nanostructures wires, rods and tubes because of their unique shape and properties have many applications especially in the fabrication of nanodevices. Recently intensive research has been done on 1D nanostructures and most of the studies has been focused on conducting nanomaterials, mainly for the microelectronic applications.[92] By downsizing the structures to the nanoscale, there will be more applications for these types of structure. The best example is microelectronics, which shows smaller structure will lead to better performance. With the invention of integrated circuits, the more components a chip has the operation will be faster, and the cost and power consumption will be lower. [93] Another great example of downsizing benefits is information storage technologies, which many works have been done on developing magnetic and optical storage components with nano size scale.[94]

In this chapter, synthesis of the metallic organic charge-transfer salt, tetrathiafulvalene bromide ($(TTF)Br_x$) will be explained. Organic charge-transfer salts

display conductive properties that make them good candidates for electronic applications. [95] In the area of organic conductors, the TTF family compounds are a point of interest since their discovery in 1973 and since then a variety of TTF compound has been synthesized with electrochemical methods. [96-97] TTF combines with halogen molecules and forms a crystal with interesting temperature dependent electrical properties and usually have needle-like shape. $(TTF)Br_{0.76}$ can be synthesized according to the following reaction:

$$TTF + 0.76\ Br^- = (TTF)Br_{0.76} + 0.76e^-\ (E^0 = 0.3\ \text{V vs. SCE}) \quad \text{(Equation 14)}$$

In this chapter, we are going to study the nanoparticle confinement effect on the size of formed crystals. Electrochemically produced AuNPs on HOPG substrate were used as nucleation seeds and effect of other factors like TTF concentration, deposition time and applied overpotential were investigated. The average $(TTF)Br_{0.76}$ crystal sizes were determined using Nanoscope software for AFM images (N=20-70) and measureIT software was used for FE-SEM images (N= 30-50).

6.2 Experimental

6.2.1 Materials

All the materials were used as received; tetrathiafulvalene (TTF, 97%, Aldrich), gold (III) chloride trihydrate (HAuCl4·3H2O, >99.9%, Aldrich), potassium chloride (KCl, ACS grade, Fisher Scientific), tetrabutylammonium bromide (TBAB, ≥ 99%, Fluka), acetonitrile (CH3CN, 99.9%, Fisher Scientific), methanol (Mallinckrodt Chemicals, 100%), 1-propanol (Fisher Scientific, 100%), ethanol (Pharmco, 100%) and HOPG (Mikromasch, ZYB grade).

Similar to AuNP electrodeposition section, potentiostat 273A (Princeton Applied research) was used for applying potential for electrochemical crystallization. We are using

a three electrode electrochemical cell. The current and potential was controlled by Gamry Instruments' framework electrochemistry software and the main electrochemical techniques that we used, are chronoamperometry and cyclic voltammetry. The working electrode is connected to the conductive surface (HOPG) and the surface will act as our working electrode, the counter electrode is Platinum (Pt), and the reference electrode is silver wire. The supporting electrolyte is 0.1M tetrabutylammonium bromide (TBAB) which its duty is to reduce the solution resistance and minimize the migration of electroactive species.

Tetrathiafulvalene (TTF) is an organosulfur compound with the formula $(H_2C_2S_2C)_2$ that is a strong electron donor and is an important component of charge-transfer salts. TTF salts have high electrical conductivity because of the planar structure which allows π-π stacking of oxidized derivatives. TTF salts also have high symmetry, which promote charge delocalization and minimizes columbic repulsions. TTF can be oxidized to a TTF^+ radical cation by applying the potential of 0.34 V (vs. Ag/AgCl). A variety of CT TTF salts electrochemically have been synthesized, for example (TTF) X_n (X= NO_3^-, Cl^-, Br^-, I^-, HCO_3^-, BF_4^-). $(TTF)Br_{0.76}$ is one of well-studied CT salts that have been synthesized on HOPG and platinum decorated HOPG electrodes successfully. [98]

6.3 Results and discussion

In order to study the electrochemical growth of the organic rods on the AuNPs seed, the synthesis of the $(TTF)Br_{0.76}$ rods was first done on bare freshly cleaved HOPG. A solution of 5 mM TTF and 0.1 M TBAB was prepared in acetonitrile. Based on the previous studies applied potential 0.5V and deposition time is 4s. [9] AFM and FE-SEM were the main tools to study the morphology of the synthesized nanocrystals. The observed crystals

have needle-like shapes with an average width of 500 ± 55 nm and 10 ± 3.4 μm in length. Also, the height of the rods is 320±48 nm which is measured from the AFM images. Figure 39 shows a side by side comparison of both SE FEM and AFM images and images show the needle shape like crystal growth on HOPG in the micrometer range. To confirm the composition of the (TTF)$Br_{0.76}$ crystals, EDS was used and the determined S/Br ratio is 5.4±1.2 (N=16) which is close to the expected Sulfur to Bromide ratio, 5.3.

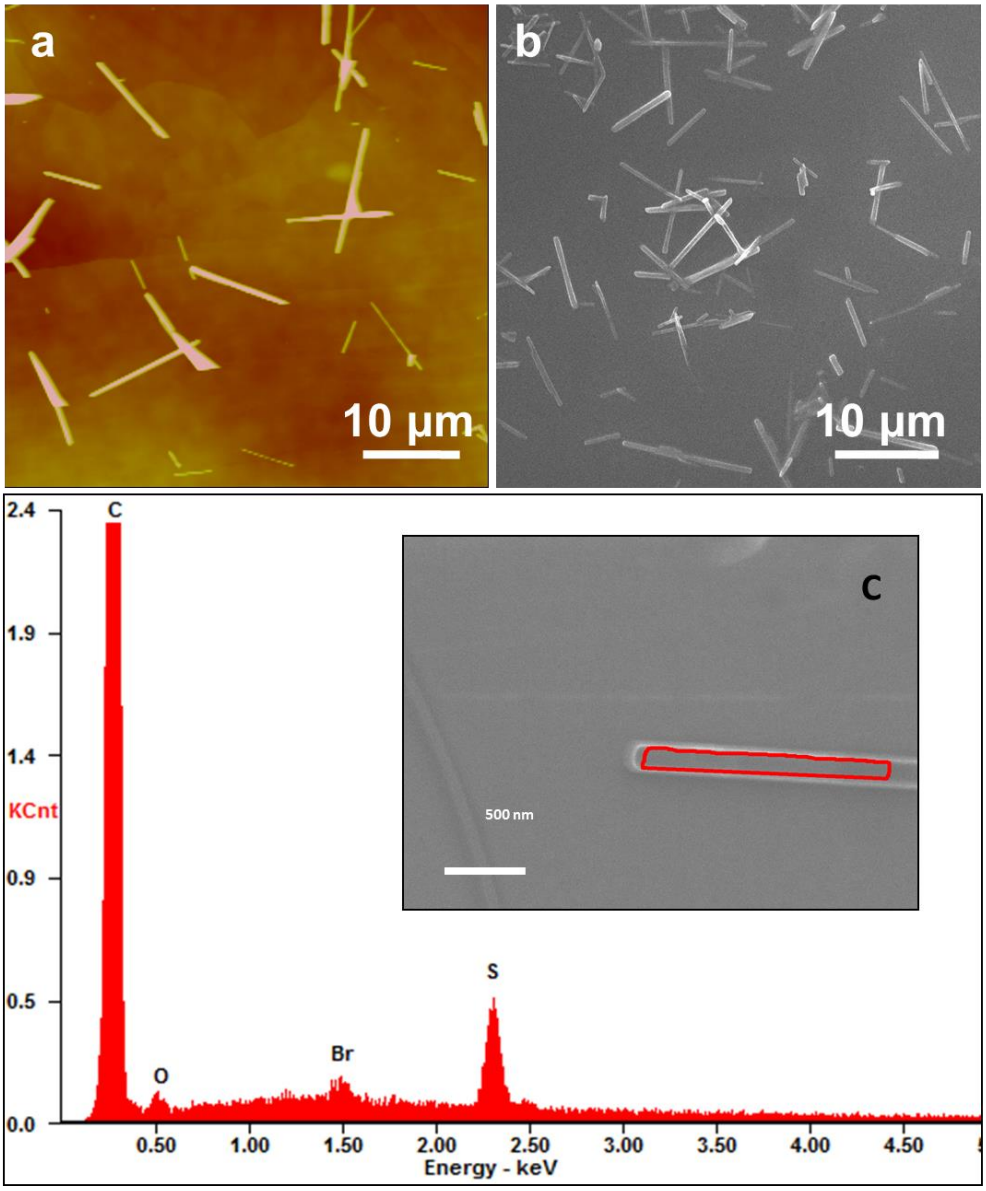

Figure 39. Side by side comparison of (a) AFM and (b) FE-SEM images of $(TTF)Br_{0.76}$ [99] and (c) EDS confirmation on the composition of the crystals on bare HOPG.

6.3.1 Effect of seed size on $(TTF)Br_{0.76}$ crystal size

In order to study the controlled growth of $(TTF)Br_{0.76}$ nanocrystals on AuNPs seeds with sizes lower than 100nm, well-formed seeds are suitable for further crystal nucleation . Considering our previous study on controlling shape and size of the AuNPs, the best candidate for the $(TTF)Br_{0.76}$ nanorod growth is two step method electrodepositing of 10

$HAuCl_4$ and 0.1M KCl. In the two step method, the first step, the potential of 0.1V and 0.01s deposition time is selected and for the second step 1V at 5s is selected which results in the best morphology of AuNPs for the growth of $(TTF)Br_{0.76}$ nanorods. First the effect of TTF concentration in acetonitrile was investigated. All the other conditions were kept the same as the previous electrocrystallization of $(TTF)Br_{0.76}$ on bare HOPG. $HAuCl_4$ concentration was 10 mM with 0.1 KCl in DI water for the seed preparation. TTF concentration was varied from 1 mM to 10 mM. Figure 40 shows the FE-SEM images of observed $(TTF)Br_{0.76}$ nanorods on AuNPs decorated HOPG. Figure 40a-c demonstrate the induced $(TTF)Br_{0.76}$ on AuNPs for different concentration of TTF and Figure 40d shows the crystallization results for 10 mM TTF with smaller AuNPs seeds. The results clearly demonstrate a preferential growth of $(TTF)Br_{0.76}$ rod on the AuNP electrodes (60%). The data show that the average size of the nanorods are much smaller than the rods grown on bare HOPG, which suggest $(TTF)Br_{0.76}$ crystal growth was affected by the presence of the AuNPs. Table 4 shows the average dimensions of the synthesized $(TTF)Br_{0.76}$ nanorods on AuNPs decorated HOPG, varying the concentration of the TTF. The smallest nanorods are seen from the 5mM TTF solution, with 99±48 nm in width and 1.26±0.50μm in length. For lower concentrations of TTF, smaller average rods are synthesized, which shows, 5mM is the optimum concentration for the growth of nano size $(TTF)Br_{0.76}$ nucleation on the AuNP decorated HOPG. It also demonstrates that the size of seeds has a significant effect on the formed $(TTF)Br_{0.76}$ crystals.

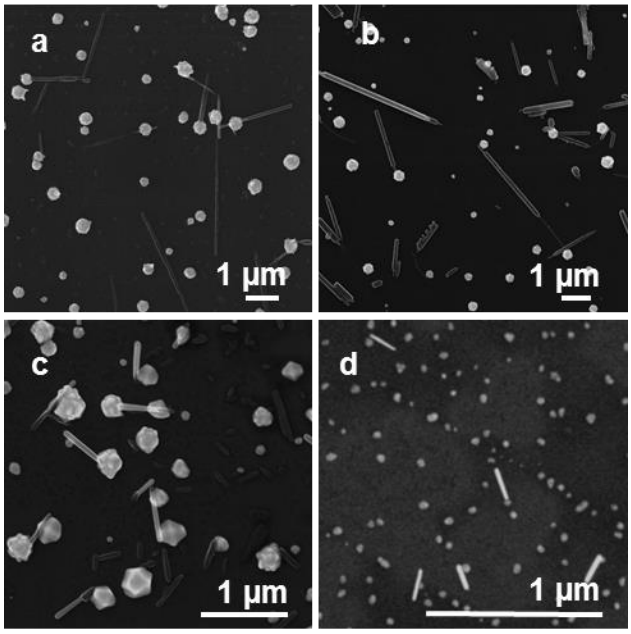

Figure 40. FE-SEM images of synthesized $(TTF)Br_{0.76}$ on AuNPs decorated HOPG with different concentrations of TTF (a) 1mM (b) 2.5mM (c) 10 mM and (d) 10mM with smaller seeds. [99]

Table 4. Average dimension of synthesized $(TTF)Br_{0.76}$ nanorods with different concentrations of TTF on AuNPs decorated HOPG. [99]

TTF concentration (mM)	AuNP Diameter (nm)	$(TTF)Br_{0.76}$ Rod Width (nm)	$(TTF)Br_{0.76}$ Rod Length (µm)
1	401 ± 90	173 ± 65	2.11 ± 1.03
2.5	397 ± 94	254 ± 74	2.03 ± 0.71
5	333 ± 85	99 ± 48	1.26 ± 0.50
10	415 ± 112	282 ± 115	3.31 ± 1.15
10	53 ± 9	36 ± 9	0.33 ± 0.14

The results for TTF concentration variation show a significant change in width of the nanorods when it is formed on smaller seeds. We furthermore studied the effect of the seed by synthesizing the $(TTF)Br_{0.76}$ on different seed sizes. A range between 30 nm to 500 nm in width of AuNP particles were prepared to be used as seeds. The $(TTF)Br_{0.76}$ nanorods were formed from 5 mM TTF solution in acetonitrile and 0.1 M TBAB as supporting electrolyte. Figure 41 shows a side by side FE-SEM and AFM images of the induced $(TTF)Br_{0.76}$ nanorods on AuNPs with different sizes. Table 5 demonstrate the analyzed data for the width and height of the AuNPs and the width and the length of the induced $(TTF)Br_{0.76}$ crystal.

Table 5. $(TTF)Br_{0.76}$ nanorods size dependent on AuNP seeds.

AuNP diameter (nm)	AuNP height (nm)	$(TTF)Br_{0.76}$ Width (nm)	$(TTF)Br_{0.76}$ Length (μm)
48.1 ± 6.8	19.6 ± 2.1	32.1 ± 7.7	0.1- 0.5
289 ± 57	134.8 ± 44.1	106.4 ± 16.8	0.8 - 2
1050 ± 208	19.2 ± 4.8	54.3 ± 11.8	0.1 – 0.5

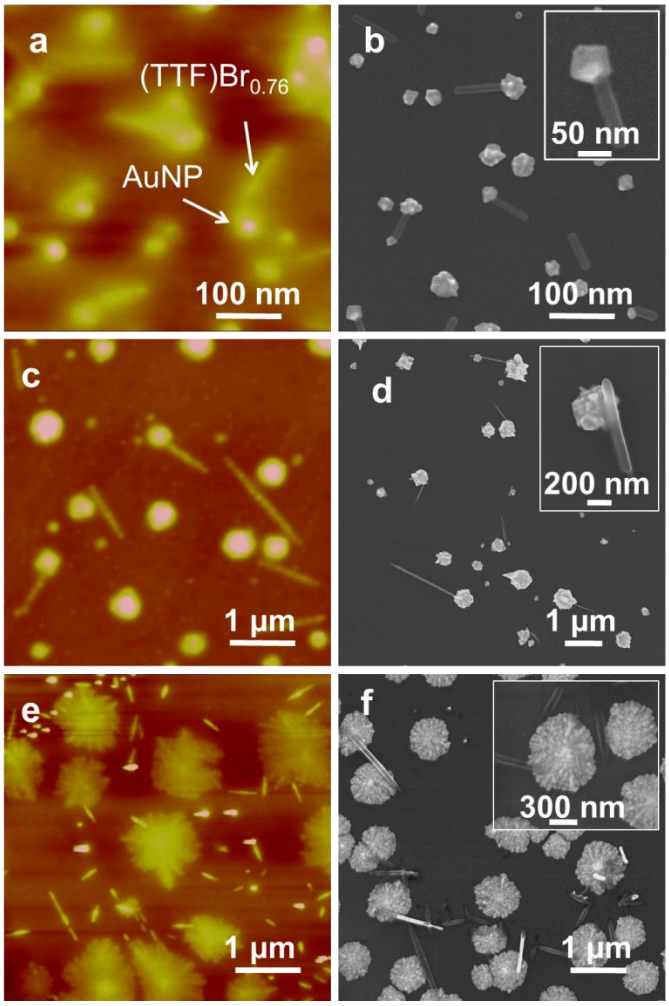

Figure 41. Side by side FE-SEM and AFM images of synthesized $(TTF)Br_{0.76}$ nanorods on AuNP seeds with different sizes. The TTF concentration for all the images is 5 mM with 0.1 M TBAB. The AuNP sizes are increasing from the top row to the bottom.[99]

The average width of the induced $(TTF)Br_{0.76}$ nanorod and AuNP particles were determined from the AFM and FE-SEM images. Figure 42 demonstrates the plotted data of the AuNP seeds versus the $(TTF)Br_{0.76}$ nanorod width. It clearly shows a linear relationship between the AuNP seed and the induced $(TTF)Br_{0.76}$ nanorod with the correlation coefficient of 0.956 which suggests that the size of the organic crystal is confined with the size of the nucleation seed. The slope of the plot is the average ratio of induced $(TTF)Br_{0.76}$ crystal width to the seed size (0.327).

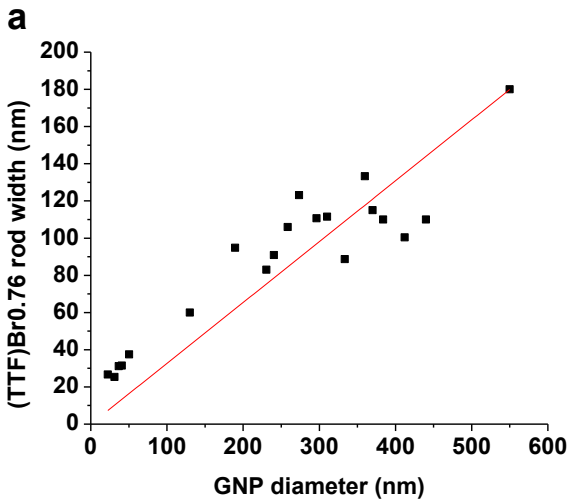

Figure 42. AuNP seeds width correlation with synthesized $(TTF)Br_{0.76}$ nanorods. [99]

Figure 43 represents close up FE-SEM images of the grown $(TTF)Br_{0.76}$ rods on the AuNPs. It clearly shows that the $(TTF)Br_{0.76}$ nanorods prefer to grow on the edges of the different shapes of the nanoparticles that has higher surface energy compared to the dominant {111} face. EDS is used to confirm the composition of the particles and the rods attached to it. EDS for gold nanoparticle Figure 44a shows a predominant Au peak and Figure 44b shows the peak for Br, S, and Au that could exist because of the overlaps of the nanorod on the gold particle. The data shows that the average atomic ratio of sulfur to bromide is 5.4± 0.7, which matches the previous data.

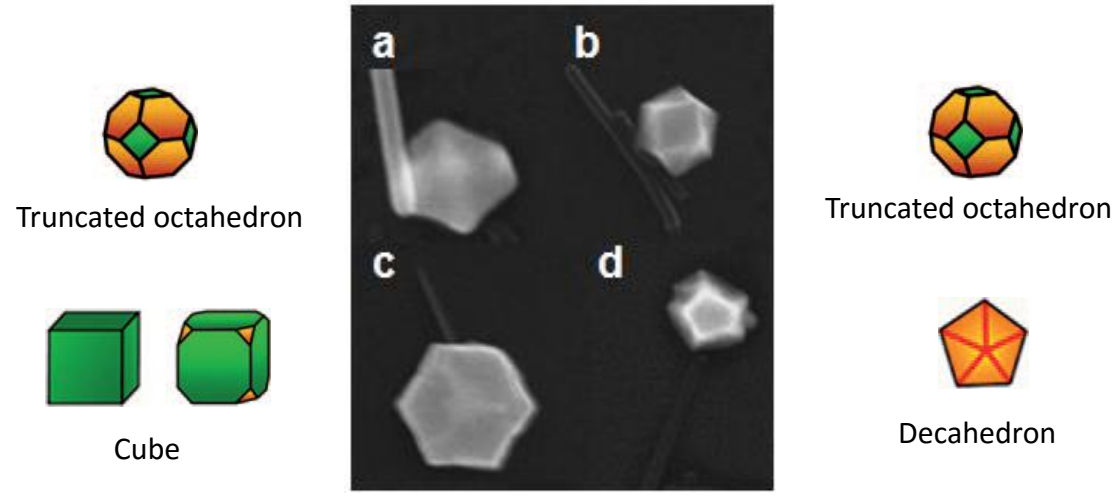

Figure 43. FE-SEM images of $(TTF)Br_{0.76}$ growth on different shapes of synthesized AuNPs on freshly cleaved HOPG and schematic shape of the spotted particles from literature [17]. Green surface represents {100} plane and orange represents {111} plane.

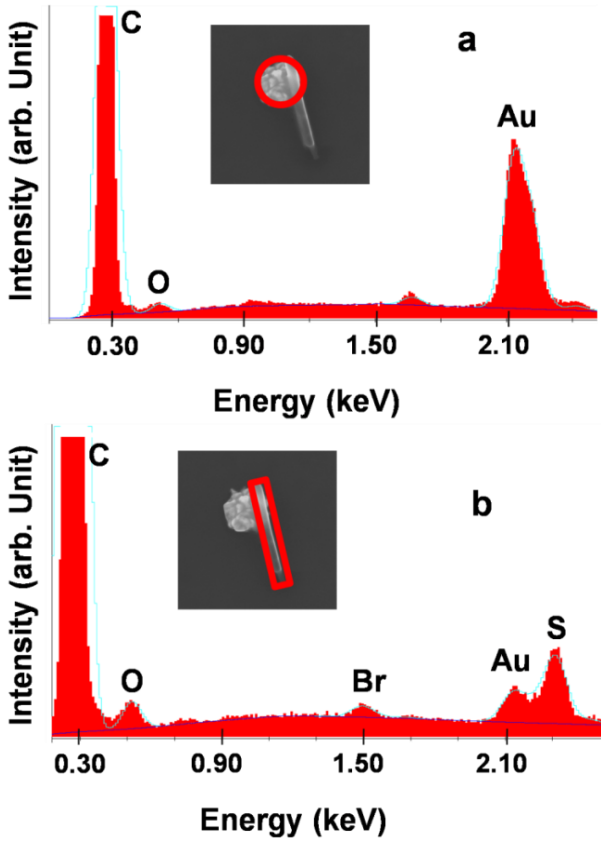

Figure 44. EDS data of (a) gold nanoparticle and (b) $(TTF)Br_{0.76}$ nanorod formed on the particle

6.4 Conclusion

In this chapter, the confinement of organic nanocrystals using inorganic particles as nucleation seed using electrochemical methods was explained. Previously studied AuNPs in chapter 5 is used as the nucleation seed for $(TTF)Br_{0.76}$ nanorods. We were able to control the shape of the formed AuNPs to be suitable for the further nucleation of the organic crystals. It was demonstrated that the $(TTF)Br_{0.76}$ nanorods prefer to grow on the seed rather than the HOPG substrate. It was also shown that the size of $(TTF)Br_{0.76}$ crystals was controlled by the confinement effect. The results show that the size of $(TTF)Br_{0.76}$ nanorods is controlled by TTF concentration in acetonitrile and also AuNPs size and morphology. This study contributes to the understanding of nanoconfinement effect using seed nucleation and controlled formation of hybrid materials using electrochemical methods.

CHAPTER 7 SYNTHESIS OF PARTIALLY OXIDIZED TETRACYANOPLATINATE NANOCRYSTALS ON GOLD NANOPARTICLE SEEDS FOR VAPOR SENSING

7.1 Introduction

One-dimensional (1D) nanostructures such as nanowires are widely recognized as the next generation building block for the direct detection of chemical/biological species.[100-106] A majority of current 1D nanomaterials are inorganic in nature, but organic nanomaterials can be both complementary and even competitive to their inorganic counterparts. Organic functional nanomaterials are attractive because they are easily processable, flexible, energy friendly, inexpensive, and compatible with downscaling towards nanodevices.[107] The ultrahigh surface-to-volume ratio, sensitivity, selectivity, and response of nanowires offer high commercial potential in a myriad of fields including defense, environmental monitoring, food safety, and industrial operations. Nanowire sensing is based on the change of nanowire electrical properties (*e.g.,* electrical conductance, resistance, and impedance) upon the adsorption of an analyte on the surface of the sensor. The high sensitivity of nanowire sensors is derived from their large surface-to-volume ratio. Nanowires offer additional mechanical benefits that enable their incorporation into flexible electronics. However, nanowires have been applied to sensing for over ten years, but very few nanowire sensors have reached the market. The major barriers are the complexity of manufacturing and difficulty in manipulating and connecting nanowires in devices. Sensor arrays in so-called electronic nose capable of detecting volatile organic compounds (VOCs) at low levels and high selectivity are in demand for a wide range of applications.[108-113] Chemically sensitive layers are still needed.[114]

Nano-sized interconnects, for example, CNTs, can be placed individually on prearranged metal contact nanopatterns, a slow process.[115-116] Alternatively, one can design individual nano-objects consisting of discrete nanoparticle cores and nanorod branches and devise further strategies to pattern these nano-objects. To that end, inorganic architectures, for example, multipods, nanodendrites, and higher-order geometries, have been synthesized.[117-121] In these examples, both seeds and nuclei consist of similar inorganic building blocks through epitaxy mechanisms. On the other hand, when organics are interfaced with inorganic nanocrystals,[122-125] they are usually deposited as shells and not as branches with separate geometry. The work reported here offers an approach to place nanowires direct on nanopatterns using the nanopattern as nucleation points. Our approach is a solution-based, room-temperature process that facilitates scalable manufacturing directly on large-area microelectronic circuitry. We made the original discovery that when mixing organic crystalline compounds with nanoparticles in a solution, nanowires of the organic compounds nucleate on the nanoparticles upon solvent evaporation.[126] Subsequently, we have formulated and tested a working hypothesis, which attributes the nanowire formation to the nanoconfinement effect imposed by the nanoparticle seed. The high curvature of a nanoparticle seed imposes unsustainable strain energy on the nucleated crystal at the crystal/seed interface and results in a nanowire crystal with constrained cross-sectional area. We have achieved control over nanowire width by nanoparticle diameter and tested our hypothesis on different nanoparticles and organic crystalline compounds.[10, 127] The nanoconfinement concept has been successfully applied to the synthesis of tetrathiafulvalene (TTF) charge-transfer salt nanowires.[99]

This paper reports the synthesis of cation deficient salt of potassium tetracyanoplatinate sesquihydrate ($K_{1.75}Pt(CN)_4 \bullet 1.5H_2O$ or KCP) nanowire crystals on AuNP seeds using electrochemistry. Nanowires are synthesized using the electrochemical method similar to our previous work with the aim to lower sizes and more control over the size of the charge transfer salt and fabrication of a sensor.[84]

The paper further demonstrates the sensing capability of KCP nanocrystals deposited on microchips for various vapors based on impedance spectroscopy. The electrochemical deposition of AuNP seeds and the seed-medicated nucleation of KCP nanocrystals were studied by CV and AFM. The nanomaterials were further characterized by FE-SEM with energy dispersive spectroscopy (EDAX) and Kelvin force microscopy (KPFM). The seed-mediated process employing direct and controllable nanowire growth on microchips will allow supramolecular structures and functions of small molecules to be utilized in electronic applications.[128-136]

Similar to previous chapter we are going to synthesize organic nanocrystals using the AuNP seeds. Partially oxidized potassium tetracyanoplatinate ($K_{1.75}Pt(CN)_4 \cdot 1.5H_2O$) also known as KCP or Krogmann's salt, is a series of partially oxidized tetracyanoplatinate complexes linked by the platinum-platinum bonds on the top and bottom faces of the planar $[Pt(CN)_4]^{n-}$ anions. One of the most widely researched properties of Krogmann's salt is its unusual electric conductance. Because of its linear chain structure and overlap of the platinum d_z^2 orbitals, Krogmann's salt is an excellent conductor of electricity. This property makes it an attractive material for nanotechnology.[137] The average AuNP sizes are determined using Nanoscope software for AFM images (N=80-100) and measureIT software was used for FE-SEM images of KCP nanorods (N= 16-30).

7.2 Experimental

7.2.1 Materials

$HAuCl_4.3H_2O$ (>99.9%, Sigma-Aldrich), KCl (ACS grade, Fisher Scientific), and Potassium tetracyanoplatinate(II) (Sigma-Aldrich) have been used as received. HOPG (ZYB grade, 1 × 1 cm^2), Platinum wire for counter electrode (Alfa Aesar, 0.25mm, 99.9%) and silver wire for quasi reference electrode (A-M systems Inc., 0.25mm).

7.2.2 Electrochemical Synthesis of KCP nanorods

All the instruments that have been used and the experiments setup are similar to our previous work. [84] PAP 263A potentiostat (Princeton Applied Research) was used in the electrochemical measurements employing a three electrode system. HOPG and AuNP decorated HOPG was used as working electrode (WE); a platinum wire was used as the counter electrode (CE) and a silver wire was used as the quasi-reference electrode (QRE). All the potentials reported in this paper are referenced to the saturated calomel electrode (SCE). AuNP electrodeposition conditions are similar to our previous study [84] Electrocrystallization of $K_{1.75}Pt(CN)_4.1.5H2O$ were conducted in 0.07-0.03 M $K_2Pt(CN)_4$ in DI water. Chronoamperometry with a pulse of 1.5 V for 0.1-1 s was used on the AuNP decorated HOPG. The substrate was rinsed with ethanol and dried with N_2 after deposition. The nanocrystals were studied and characterized with a Dimension 3100 AFM (Bruker). Both tapping mode and contact mode were used for imaging the nanostructures. For tapping mode, silicon tapping mode tips with a resonance frequency of 300 kHz (nanoScience instruments, Vista Probes T300) and for contact mode, aluminum coated silicon tips with a resonance frequency of 12 kHz (nanoScience instruments, Vista Probes CLR-10) were used. The height, the amplitude, and phase images were recorded with a

scan rate of 1 Hz. Size analysis of the nanoparticles was done with NanoScope analysis 1.5.Nanoparticles were characterized by FE-SEM (JEOL JSM 7600F SEM). The acceleration voltage was 5kV and 15 kV with a working distance of 8mm and probe current of 6 µA. Observed images were analyzed with MeasureIT software (Olympus). The elemental composition data were obtained by *in situ* energy-dispersive spectroscopy (EDS) attached to the FE-SEM, and the EDAX Genesis V6.33 software was used to collect the data.

7.3 Results and Discussion

7.3.1 Confined synthesis of partially oxidized KCP using AuNP seeds

Metal nanoparticles supported on bulk electrodes are useful for electroplating, fabrication of microelectronics, electrocatalysis, and understanding of charge transport phenomena including tunneling, single-electron charging, percolation effects, and scattering in granular materials.[138-141] Here AuNPs are used as nucleation seeds for the synthesis of KCP nanowires. AuNPs on highly ordered pyrolytic graphite (HOPG) were prepared by hydrogen tetrachloroaurate ($HAuCl_4$) reduction as described before. [84, 142-144] The concentration of $HAuCl_4$ was varied from 0.05 to 1 mM with 0.1 mM KCl as supporting electrolyte. CV measurements were used to determine the appropriate potential range for gold reduction based on equilibrium reduction potential. The scan rate was fixed at 100 mV/s for all the experiments. The potential range was varied between -0.5 and 1.5 V. The $HAuCl_4$ concentration range was varied between 0.05 and 10 mM.

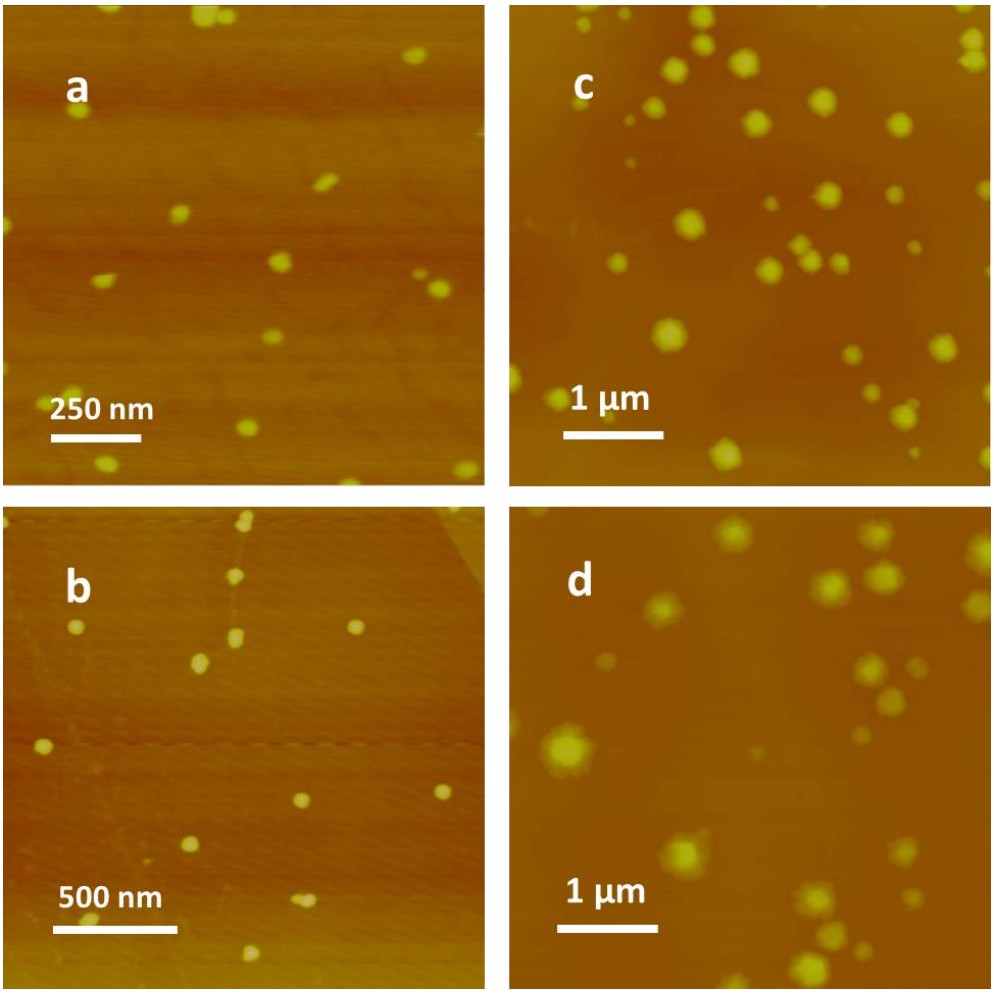

Figure 45. AFM height images of deposited AuNPs on HOPG in different concentrations. Applied overpotential was fixed at -0.5 V and deposition time was fixed at 0.01 s. Concentration of HAuCl4 was (a) 0.01 mM, (b) 0.1 mM, (c) 1 mM, and (d) 5 mM. (e)

The AuNP morphology was studied as a function of the $HAuCl_4$ concentration and deposition time. AFM and FE-SEM were used to determine the size, morphology, and density of the deposited AuNPs on HOPG. The HOPG basal plane surface was cleaved using Scotch tape immediately prior to use. The overpotential was fixed at -0.5V for all the cases while the $HAuCl_4$ concentration was varied at 0.01 mM, 0.1 mM, 1 mM and 5 mM. Potentiostat and amperometric pulses were applied using potentiostat 273A (Princeton Applied research). Figure 45 shows the deposited AuNPs on HOPG as a function of the

$HAuCl_4$ concentration. Particle density was determined by the average number of particles per μm^2 from more than 20 AFM images for each concentration. Particle density for $HAuCl_4$ concentration of 0.01 mM, 0.1 mM, 1 mM and 5 mM, is 19.0 ± 4.5, 13.0 ± 3.8, 0.98 ± 0.15 and 0.28 ± 0.05 per μm^2 respectively. The data show that AuNP particle density decreases when increasing $HAuCl_4$ concentration. It is due to the larger size of AuNPs and larger depletion zone [86], higher concentrations have higher mass transfer gradient and this leads to larger particle size. Deposition time is 0.01s for all the cases. Since the deposition is diffusion-controlled growth, the depletion layer dictates the particle density. It means that when the size of the particle gets larger when deposition time and overpotential is the same depletion layer will be larger this will lead to lower particle density [145]. AFM images show that the size of the AuNPs increases with increasing concentration. The shape of the AuNPs changes from spherical to a dendritic shape when the concentration is above 1 mM. The smallest observed particle size for 0.01 mM $HAuCl_4$ is 38 ± 3 nm in width and 10 ± 1 nm in height.

The AuNP-covered HOPG was used as the working electrode for electrochemical crystallization of partially oxidized tetracyanoplatinate salt. Based on the AuNP electrodeposition results, we chose an $HAuCl_4$ concentration range below 1 mM for depositing hemispherical seeds in the size range of 60 to 500 nm for nucleating KCP crystals. The applied overpotential was kept at -0.5 V and deposition time at 10 ms for AuNP electrodeposition.

The family of partially oxidized tetracyanoplatinates is one of the oldest 1D conducting materials formed by oxidation of crystalline samples of Pt(II) complexes.[146] Krogmann salts and similar 1D materials based on transition metal backbones were intensively studied

from 1960 to 1980 and appear to gain renewed interest associated with nanotechnology.[137] For example, platinum double salt crystals in the form of $[Pt(CNR)_4][M(CN)_4]$ (M = Pt, Pd; R = aryl, alkyl) can detect volatile organic compounds (VOCs) due to the color change upon solvent molecule adsorption.[147] The original anion deficient salt, potassium tetracyanoplatinate bromide trihydrate ($K_2[Pt(CN)_4]Br_{0.3}\bullet 3H_2O$ or KCP(Br)) possesses high, nearly metallic conductivity due to short Pt-Pt separation (2.89 angstroms) thus allowing intrachain valence electron delocalization along the stacking direction of the tetracyanoplatinate complex $Pt(CN)_4^{2-}$.[148-152] The crystal structure of KCP was determined using single crystal neutron diffraction by Williams et al.[153-156] The synthesis and crystal structure of the cation deficient salt, potassium tetracyanoplatinate sesquihydrate ($K_{1.75}Pt(CN)_4\bullet 1.5H_2O$ or KCP) were also reported.[156-157] It has a triclinic crystal structure with the following unit cell lattice parameters: a = 10.360 Å, b = 9.303 Å, c = 11.832 Å, α = 77.57°, β= 114.74°, γ = 73.64°, and V_C = 918.3 $Å^3$ and Pt to Pt separation of 2.96 Å. Study shows that partially oxidized Krogmann's salt has a non-linear Pt chain that makes the crystal display large electrical and optical conductivities along the chain axis due to the d_z electron orbital overlap. The crystal has 3 non-equivalent Pt atoms and two distinct Pt-Pt separations (2.966 and 2.978 Å). [158-160]

Electrochemical reduction of 0.07 M of $K_2Pt(CN)_4$ in deionized water on HOPG to form $K_{1.75}Pt(CN)_4.1.5H_2O$ crystals was conducted following literature procedure using a potential pulse of 1.5 V (*vs.* SCE) for 0.1 s $1.75K^+ + Pt(CN)_4^{2-} + 1.5H_2O \rightarrow 0.25e^- + K1.75Pt(CN)4.1.5H2O$. (Equation 15): [156]

$$1.75K^+ + Pt(CN)_4^{2-} + 1.5H_2O \rightarrow 0.25e^- + K_{1.75}Pt(CN)_4.1.5H_2O \ .$$ (Equation 15)

The $Pt^0/Pt(CN)_4^{2-}$ oxidation potential is 0.59 V (*vs.* SCE). Needle shaped crystals with a size range of 600 nm to 5µm in length and 100-500 nm in width was synthesized on bare HOPG with an aspect ratio of 3.18 ± 0.86. Figure 46 shows an FE-SEM image of the formed crystals on HOPG.

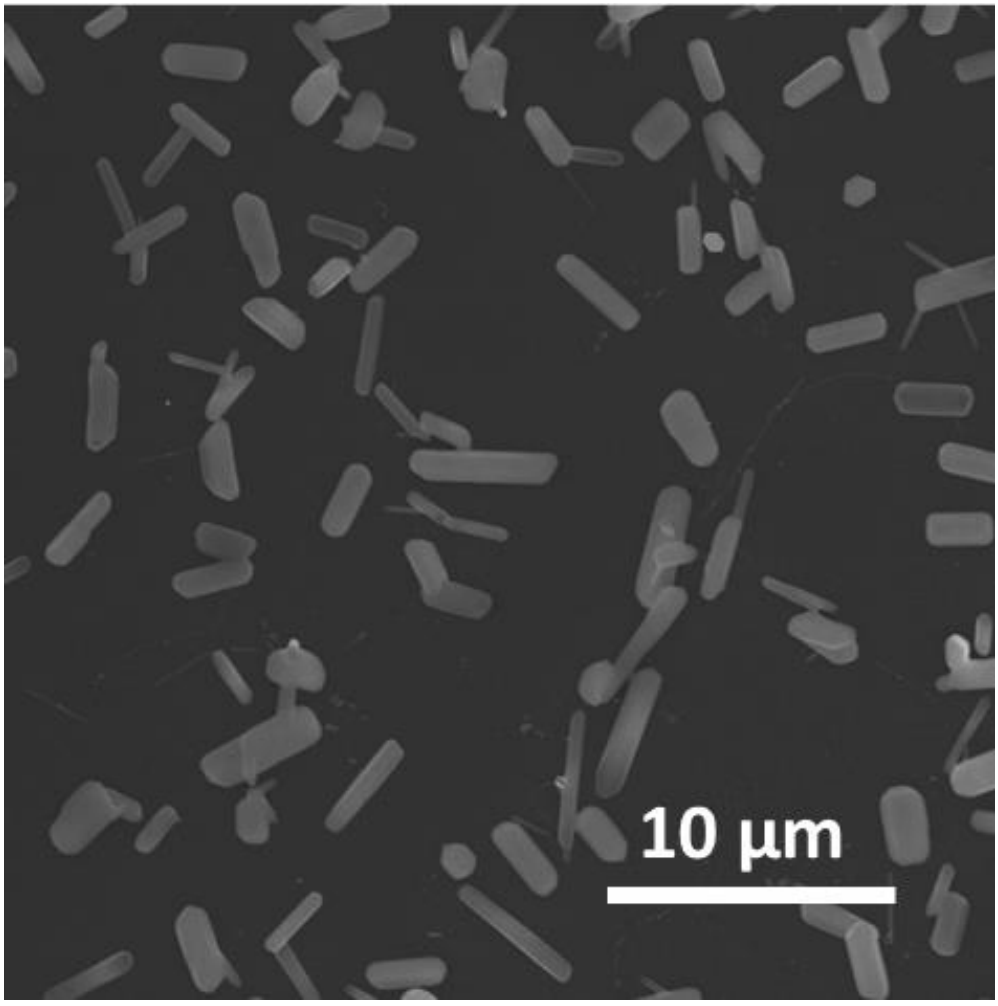

Figure 46. Field emission SEM image of $K_{1.75Pt}(CN)_4.1.5H_2O$ bulk crystals on bare HOPG.

To study the controlled electrocrystallization of KCP nanocrystals on AuNPs decorated HOPG, AuNPS are synthesized based our previous work on the synthesis of different sizes and shapes of AuNPs. AuNPs are prepared from 10mM aqueous solution of $HAuCl_4$ with the two-pulse method. The first step will be done with a applied potential of

0.1 V for 0.01 s, and the second step with applied potential of 1 V and for 5 s, spherical shapes AuNPs are synthesized to be used as electrodes for KCP crystal formation. Different concentrations of $K_2[Pt(CN)_4]\cdot 3H_2O$ are prepared to study the effect of the concentration on the KCP nanorods formation. Selected concentration range is from 0.03M to 0.3M of $K_2[Pt(CN)_4]\cdot 3H_2O$ in DI water. In order to study the nanoconfinement effect, the concentration is reduced to 0.3 M. The KCP electrocrystallization was done with applied potential of 1.5V with different deposition time varies from 0.01 to 1s. The average diameter of AuNP electrodes is 436±251 nm and average formed KCP nanorod is 190±121 nm with a length range from 100 nm to 3µm. Figure 47 shows FE-SEM images of KCP nanocrystal grown on AuNPs decorated HOPG. Concentration of $K_2[Pt(CN)_4]\cdot 3H_2O$ is at constant 0.3M in DI water and applied potential is 1.5V for 0.1s. The FE-SEM images show that preferential growth of the KCP nanorods on the nucleation seeds is the result of higher electrochemical activity on the AuNPs compared to HOPG substrate. Table 6 represents the data analysis of the observed FE-SEM images. $K_2[Pt(CN)_4]\cdot 3H_2O$ concentration is 0.3M, applied potential 1.5V and deposition time is 0.1 s for all the samples. Gold nanoparticle size varies from 564±106 nm to 345±88 nm the AuNPs are synthesized from the reduction of 5mM, 1mM and 0.1mM of $HAuCl_4$. Figure 48 represents the observed data from FE-SEM images of several experiments for KCP formation on AuNPs decorated HOPG, and it plots the average KCP nanorods width formed on the AuNPs versus AuNPs width. The plot shows a linear relationship between them, which describes the seed nucleation effect on crystallization.

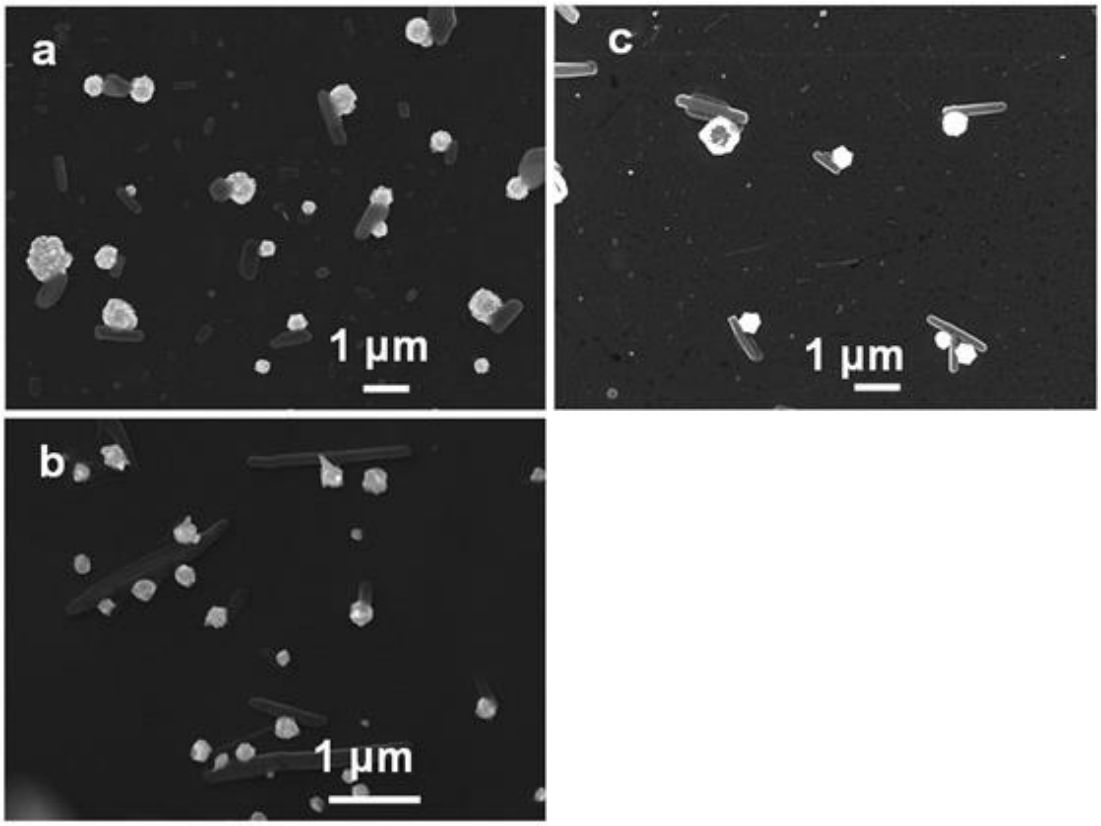

Figure 47. FE-SEM images of KCP nanorods nucleated from gold nanoparticle seeds for different sizes of AuNPs

Table 6. Dimension of KCP nanorods nucleated on AuNPs seed with 0.3 M concentration of $K_2[Pt(CN)_4]\cdot 3H_2O$ with different $HAuCl_4$ aqueous concentration , (a) 5mM (b) 1mM HAuCl4 (c) 0.1mM HAuCl4 based on FE-SEM data.

$HAuCl_4$ (mM)	AuNP Diameter (nm)	$(TTF)Br_{0.76}$ Rod Width (nm)	$(TTF)Br_{0.76}$ Rod Length (μm)
5.0	564 ± 106	318 ± 66	2.28 ± 0.44
1.0	440 ± 104	263 ± 41	3.11 ± 1.20
0.1	345 ± 88	212 ± 56	3.78 ± 1.45

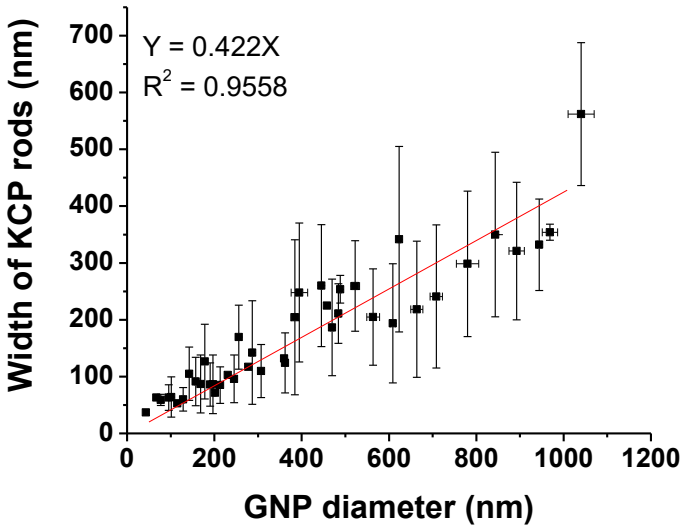

Figure 48. Plot of average KCP nanorods diameter versus AuNPs seed diameter observed from FE-SEM images of different experiments

As we described in section 4.1 of AuNPs is synthesized via electrochemistry method, although different shapes are formed on the HOPG electrode, there is no control over the specific shape of formed electrochemistry. In this section a method will be proposed that may will lead to controlled electrocrystallization over the shape and we will use the synthesized AuNP on HOPG to investigate the effect of seed shape on crystallization of KCP crystals.

We independently verify the crystal structure of KCP crystals by single X-ray crystallography. Unit cell drawing of KCP crystal has been demonstrated in Figure 49.

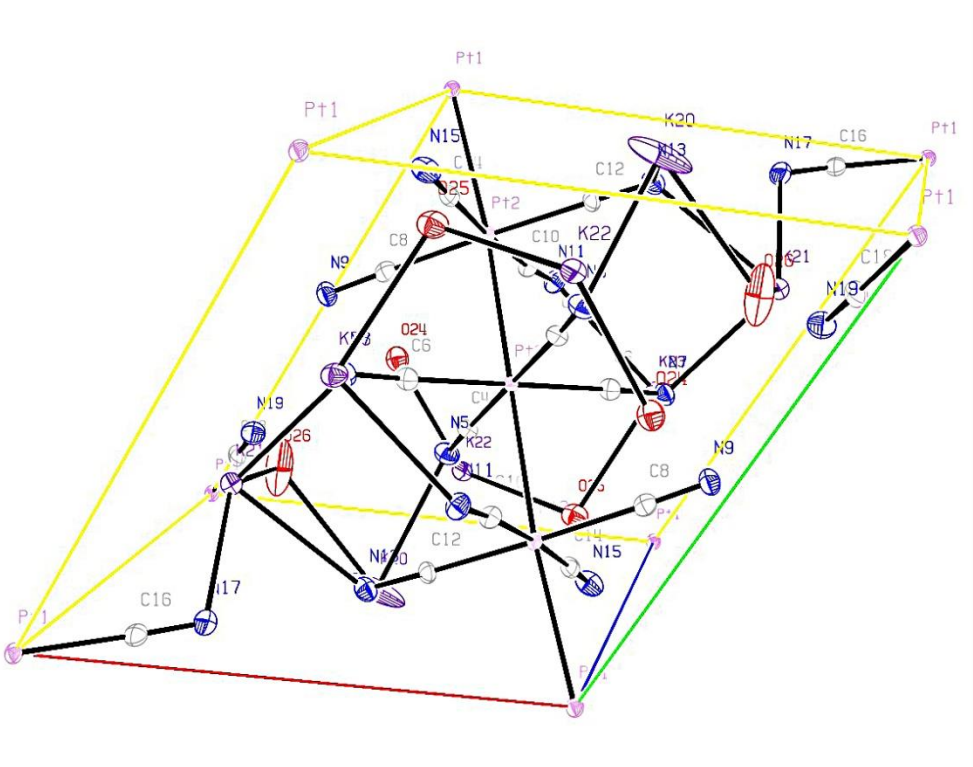

Figure 49. The unit cell of $K_{1.75}Pt_2(CN)_8 \cdot 1.5H2O$ crystal structure showing the nonlinear Pt(l)-Pt(2)-Pt(S) (marked on the image) chain that extends along the [111] direction and has equal Pt-Pt separations.

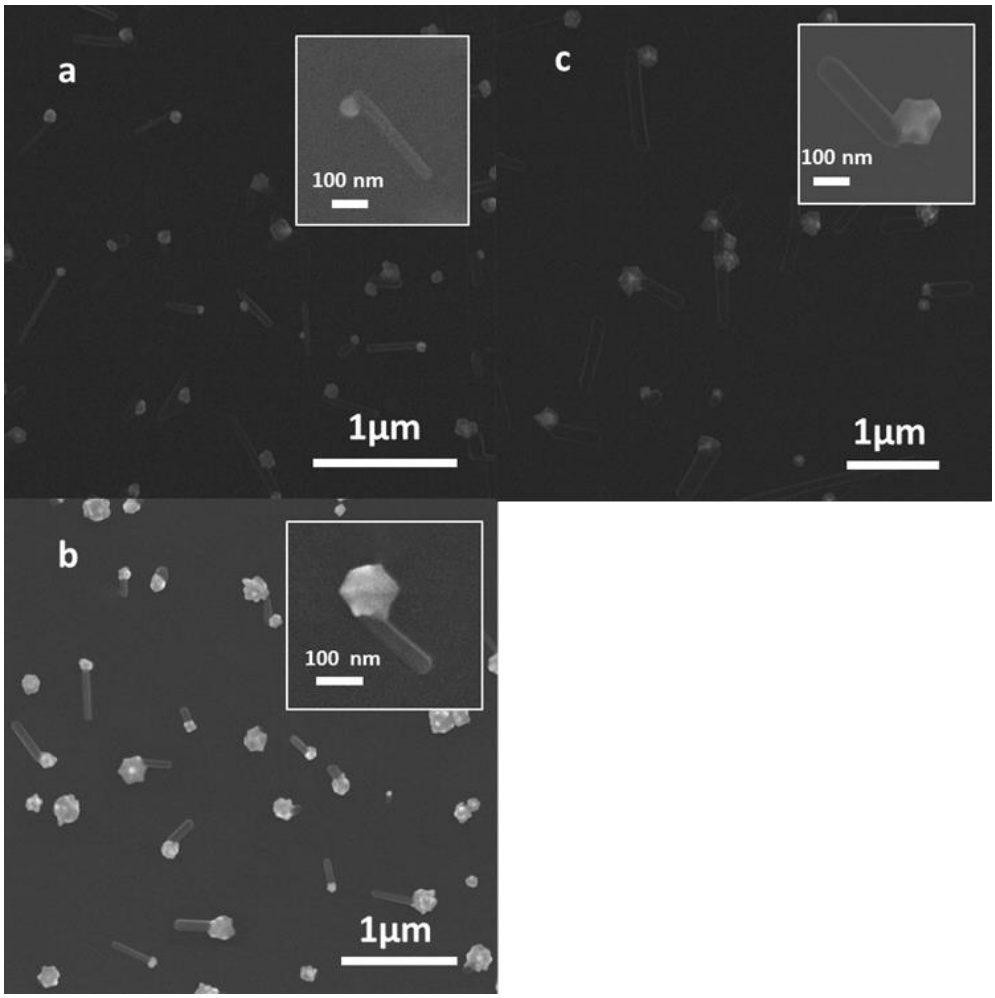

Figure 50. FE-SEM image of nanocrystals synthesized on AuNP seeds, K2[Pt(CN)4]·3H2O concentration was 0.07 M and applied potential was 1.5 V for 0.1 s. Average AuNP particle width is (a) 97 ± 16 nm, (b) 176 ± 20 nm, and (c) 237 ± 25 nm.

In the next step, the size of the seed was reduced to below 300 nm range to furthermore study the confinement effect in a smaller scale. The concentration of $K_2[Pt(CN)_4]\cdot 3H_2O$ was set to 0.07 M in order to study its effect on the size and shape of the crystal. The applied potential was fixed at 1.5 V and the pulse time was varied from 0.01 to 1 s. Under these experimental conditions, we were able to grow KCP nanocrystals in the width range of 40-250 nm and length range of 0.08-3 µm. Figure 50 shows the observed FE-SEM images of KCP nanocrystals grown on AuNP-decorated HOPG. The concentration of $K_2[Pt(CN)_4]\cdot 3H_2O$ was 0.07 M and the applied potential, 1.5 V was pulsed for 0.1 s. The

FE-SEM images clearly show the preferential growth of the KCP nanorods on AuNP seeds than the HOPG substrate. FE-SEM data analysis also shows that roughly the 65% of the nanorods were grown on the AuNPs. A closer examination of the SEM images shows that there is a direct correlation between the width of the KCP nanorods and that of the AuNP seeds to which they are attached. Most of the nanorods are oriented in the radial direction, but a minor fraction (33 %) of the nanorods orient tangentially to the AuNP surface. Figure 51 plots the KCP nanorod width as a function of its seed AuNP width. The KCP nanorod aspect ratio is 4.15 ± 0.16, 2.86 ± 0.25, and 3.51 ± 0.44 for the three KCP nanorod sizes 97 ± 16 nm nm, 176 ± 20 nm, and 237 ± 25 nm nm, respectively.

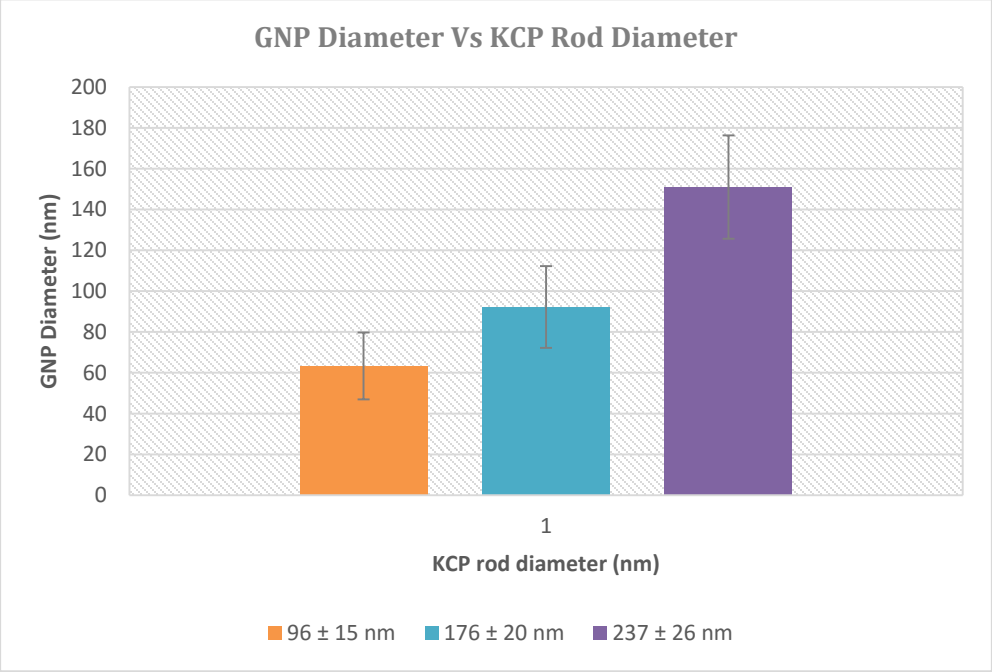

Figure 51. Average AuNP diameter vs. average synthesized KCP nanorod diameter.

The plot shows a linear relationship between the seed and seed-induced nanocrystal width values. EDS was used to confirm the composition of the KCP crystal deposited on

HOPG. Both K and Pt were detected by EDS focused on the KCP crystal (Figure 52). The measured K/Pt ratio, 1.84, is slighted higher than the theoretical value, 1.75, of the KCP crystal.

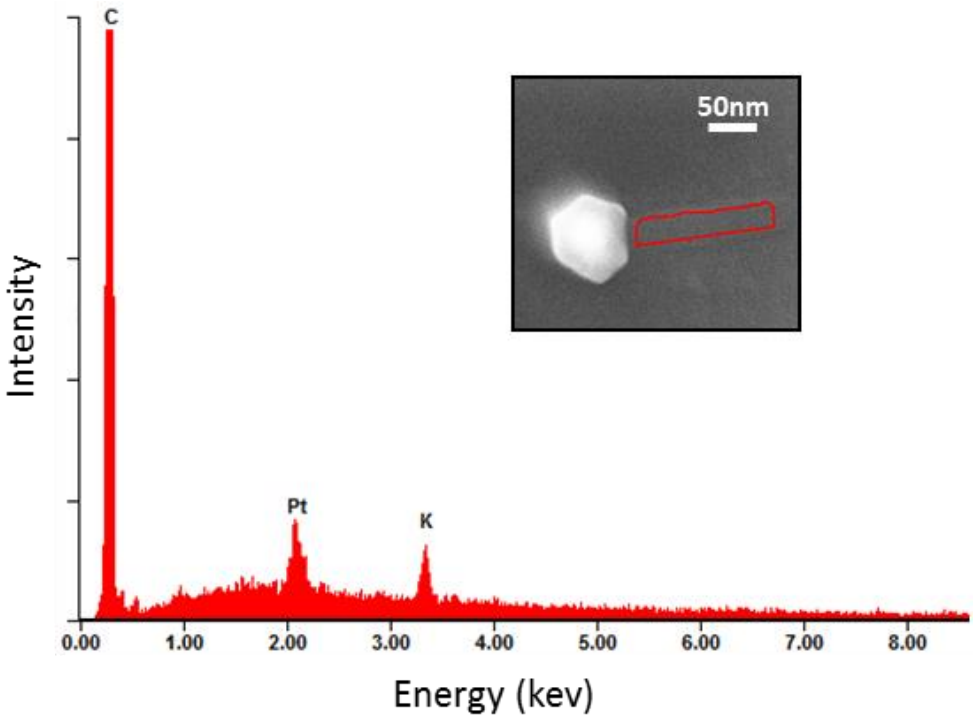

Figure 52. EDS results of a KCP nanorod synthesized attached to the AuNP.

The seed-mediated electrocrystallization process was also studied by real-time AFM. The home-built electrochemical fluid cell was shown in Figure 53. Describe the basic elements of the fluid cell. The fluid cell was connected to the potentiostat with the HOPG as the working electrode before conducting real-time AFM imaging of the electrochemical process. The AuNP electrodeposition was same as above.

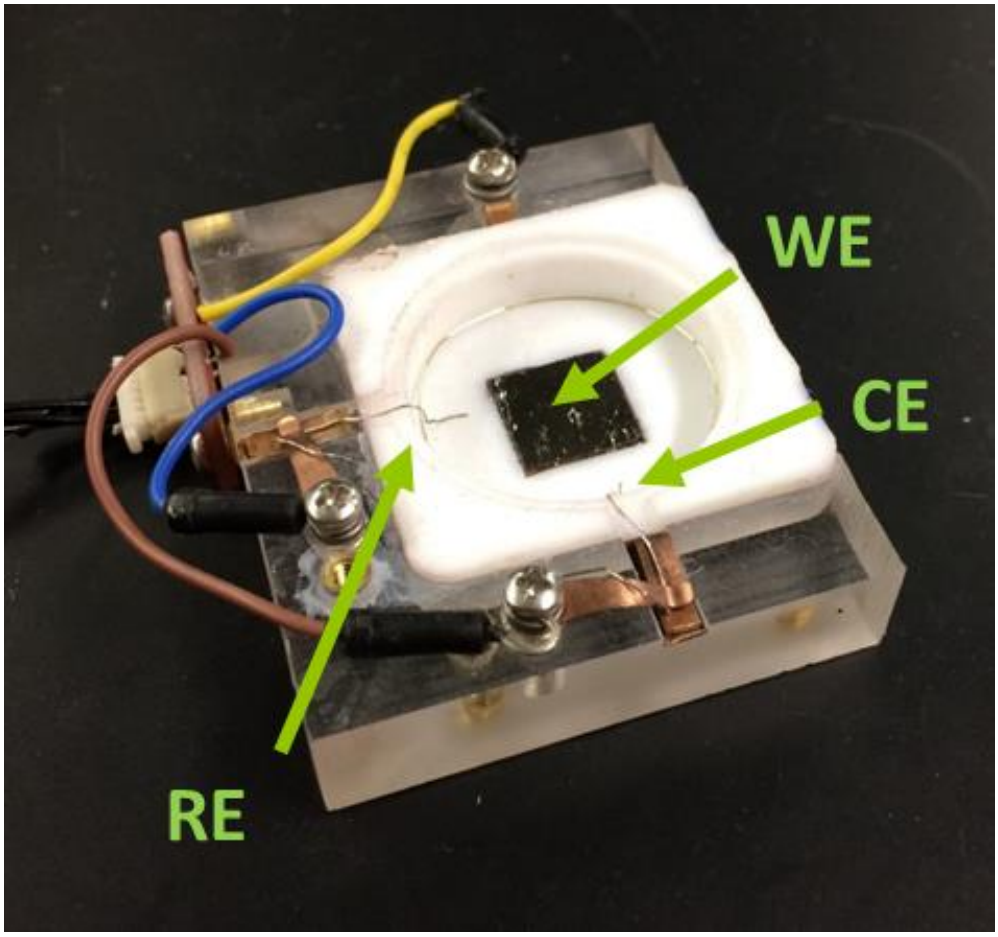

Figure 53. Designed three-electrode cell for in situ electrochemical AFM measurements. WE, working electrode, fresh peeled HOPG, CE, counter electrode, platinum wire, RE, reference electrode, silver wire.

Figure 54b shows an AFM imaged of AuNP-decorated was imaged in the solution of 0.07 M $K_2[Pt(CN)_4]\cdot 3H_2O$ in DI water. The overpotential was -0.5 V and the pulse time was 0.01 s, and the concentration of $HAuCl_4$ was 5 mM. The average AuNP height and width are 82 ± 23 nm and 336 ± 35 nm, respectively, by AFM sectional height analysis. The width was determined by the particle width at half maximum height in order to minimize AFM tip convolution. Then 0.07 M $K_2[Pt(CN)_4]\cdot 3H_2O$ solution of 1 μL in DI water was injected into the cell. The potential pulse of 1.5 V for 0.01 s was applied while AFM scanning was conducted. Figure 54b-c shows the observed images before and after

deposition of the KCP crystals. In Figure 54c, the average nanorod size was determined by AFM sectional height analysis to be 156 nm in length and 342 nm in width.

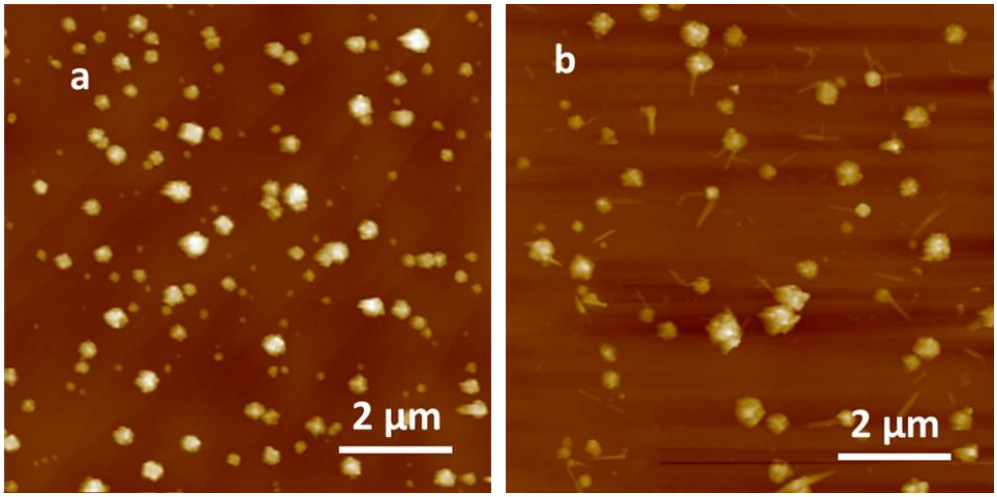

Figure 54. *in-situ* AFM imaging of (a) AuNP seeds and (b) synthesized KCP nanorods on AuNP seeds

7.3.2 Manufacturing a vapor detecting sensor using the hybrid structure

Next we conducted Kelvin Probe Force Microscopy (KPFM) measurements on individual KCP nanorods to confirm the conductive nature of the KCP nanorods as well as the electrical conductivity change when exposed to water vapor. KPFM is a tool to measure the contact potential difference (CPD) between a conducting AFM probe and the surface. It is a unique characterization technic to analyze the electrical properties of conductive and semiconductive materials in a nano-scale domain. When two conductive materials are connected through an external wire, the electrons will flow from the one with lower work function to the other one with higher work function to equalize the Fermi energy levels. If the materials are plates with small distant, equal opposite charges will be induced to the surfaces of the plates. The potential between the plates is called CPD. If a potential of equal magnitude but opposite direction to the CPD is applied to the surface, the surface charge will become zero. KPFM will detect and monitor CPD to map the electrical properties of the surface. [161] The conductive probe and the conductive sample will act as a capacitor. The electrostatic force can be calculated from following equation:

$$F_{el} = -\frac{1}{2}\frac{\partial C}{\partial z}(\Delta V)^2 \qquad \text{(Equation 16)}$$

In this equation F_{el} is the electrostatic force, C is the capacitance between the tip and the surface, ΔV is the voltage difference that is:

$$\Delta V = V_{DC} - V_{CPD} + V_{AC}\sin(\omega t) \qquad \text{(Equation 17)}$$

Which is the sum of externally applied DC voltage (V_{DC}), intersinic CPD (V_{CPD}) and AC voltage (V_{AC}). By combining two equations we will have:

$$F_{el} = \frac{\partial C}{\partial z}\left((V_{DC} - V_{CPD})^2 + \frac{1}{2}{V_{AC}}^2\right) + \frac{\partial C}{\partial z}(V_{DC} - V_{CPD})V_{AC}\sin(\omega t) + \frac{1}{4}\frac{\partial C}{\partial z}{V_{AC}}^2\cos 2\omega t$$ (Equation 18)

This equation describes that the applied AC voltage with ω frequency will cause, the force to be modulated at ω and 2ω frequencies which can be measured by the cantilever deflection. This frequency usually is selected to be close to the cantilever resonant frequency for better sensitivity of the cantilever.

Crystals were imaged with Keysight 5500 KPFM instrument using similar synthesis procedure as described above. Real-time KPFM imaging was conducted to measure electrical property change of the KCP nanorod after its exposure to the water vapor (Figure 55-Figure 57). KPFM measures the capacitance gradient of the sample, which is related to the nanorod conductivity. Figure 55 shows the KPFM image of KCP nanorods deposited on HOPG. Figure 56 shows the average capacitance gradient change of KCP crystals when exposed to water vapor. The data show that KCP capacitance gradient increases upon exposure to water vapor, and the effect is reversible with the capacitance gradient decreasing after purging with N_2. The same trend was observed for different sizes of KCP nanocrystals with length range from 100 nm to 2,000 nm (Figure 57). KPFM measurements show that the electrochemically deposited KCP nanocrystals are conductive.

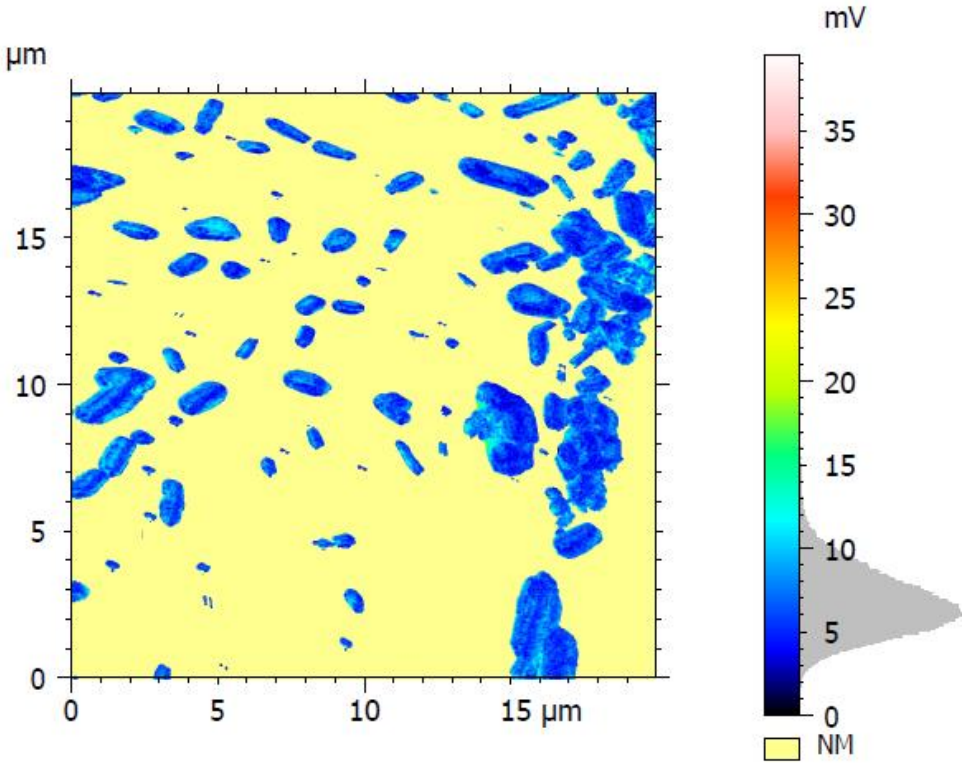

Figure 55. Capacitance gradient KPFM image of KCP nanorods.

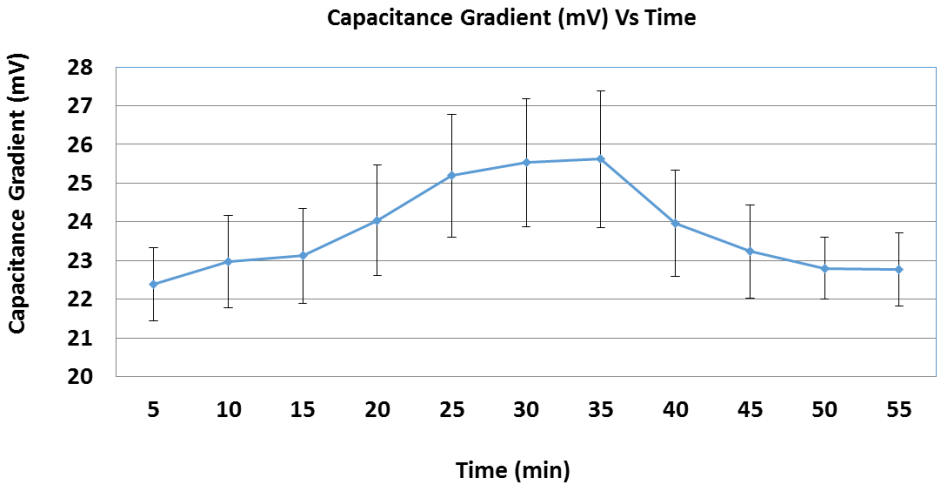

Figure 56. Average capacitance gradient change of KCP nanorods with exposure to water vapor.

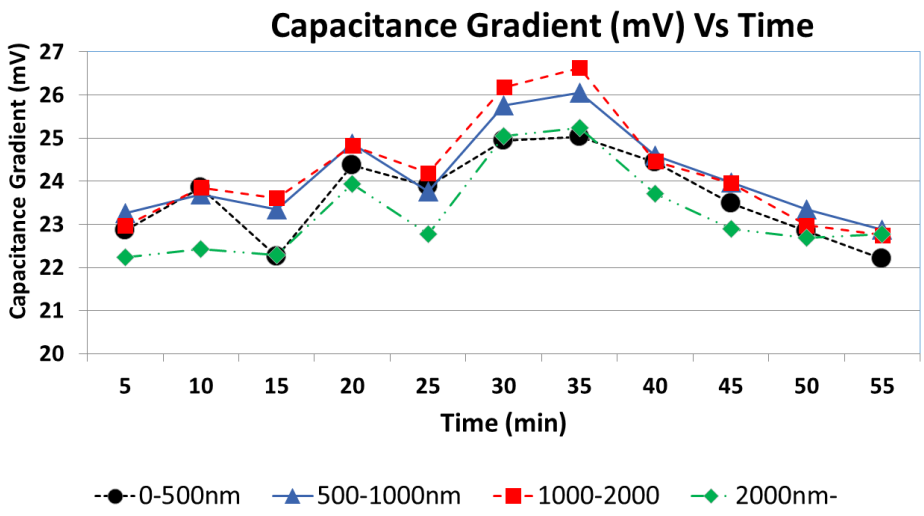

Figure 57. Capacitance gradient change of KCP rods with respect to the size of the rods

After confirming the conductivity of the electrochemically synthesized KCP nanocrystal, we attempt to show their potential use in sensor devices. To that end, KCP crystals were synthesized on patterned Cr/Au electrodes by reducing 0.3 M solution of $K_2Pt(CN)_4$ using an applied overpotential of 1.5 V for 1 h. The fabrication of electrodes was done by standard photolithography. The Au pattern is comb-like inter-digit electrodes with a spacing of 10, 20 and 30 μm for ensuring a better connection. Figure 58 shows a photo of the electrode with the pattern printed on a glass plate. The inset photo shows the interdigitated lines at close-up.

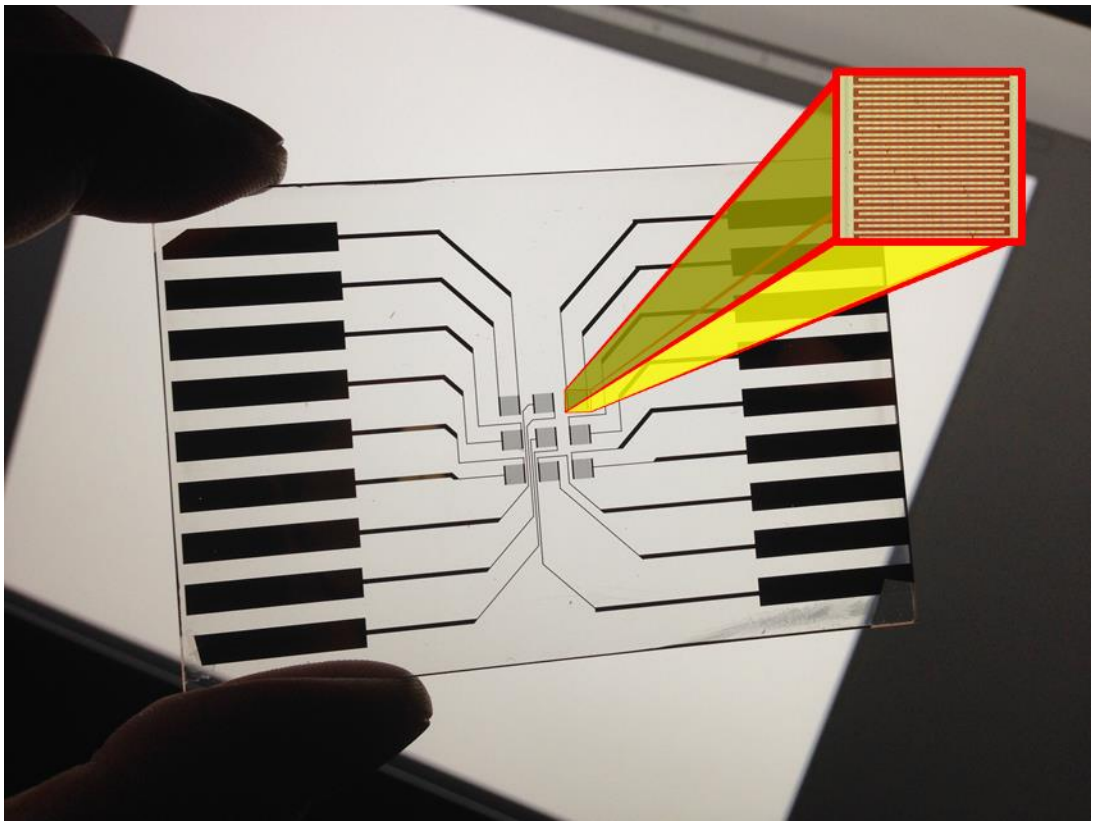

Figure 58. Comb-like Au pattern electrodes on glass for KCP crystal synthesis. The spacing between the electrodes is 10, 20 and 30 μm.

The patterned electrode containing KCP microcrystals was exposed to vapors of water, ethanol, and acetone in a home-built vapor chamber and the impedance of the electrode was measured by an electrochemical workstation (CH Instruments Electrochemical Workstation 600D) with a commercial humidity meter (Extech Instruments, Humidity alert II) as a control for water vapor. Impedance is a complex number (Z) in which, the real part represents resistance (R) and the imaginary part is reactance (X). Reactance is consisted of two parts, capacitive reactance that represents the capacitance and Inductive reactance that represents Faraday's law of electromagnetic induction. [162] In this study, the impedance involving both terms is monitored as the crystal is exposed to the target vapors. We

hypothesize that molecular adsorption of the target vapor on the crystal surface will change the polarity of the crystal depends on the polarity of the vapor molecules which changes the conductivity properties of the crystal. The change in impedance can be due to the change in resistance and conductance of the crystal and the conductance change can be because of the change in dielectric constant with the presence of the vapor. The chamber was purged with N_2 prior to each experiment. Figure 59 shows the impedance variation as a function of time when exposed to different vapors including water, methanol, ethanol, isopropanol, dichloromethane, and hexane. The KCP crystals show higher sensitivity to polar solvents while little or no impedance change when they are exposed to nonpolar solvents such as hexane and dichloromethane. The polarity index for water is 9 , methanol 5.1, ethanol 5.2 , isopropanol 3.9, dichloromethane 3.1, and hexane 0. [163] To demonstrate the sensitivity of KCP conductivity, water vapor concentration was varied in the range of 0.002-0.011 M by controlling the volumetric flow rate of saturated water vapor relative to that of N_2. Figure 60 shows the repeatability of the sensor function by cycling the measurements 10 times. Lastly, Figure 61 shows the impedance value decreasing with decreasing water concentration.

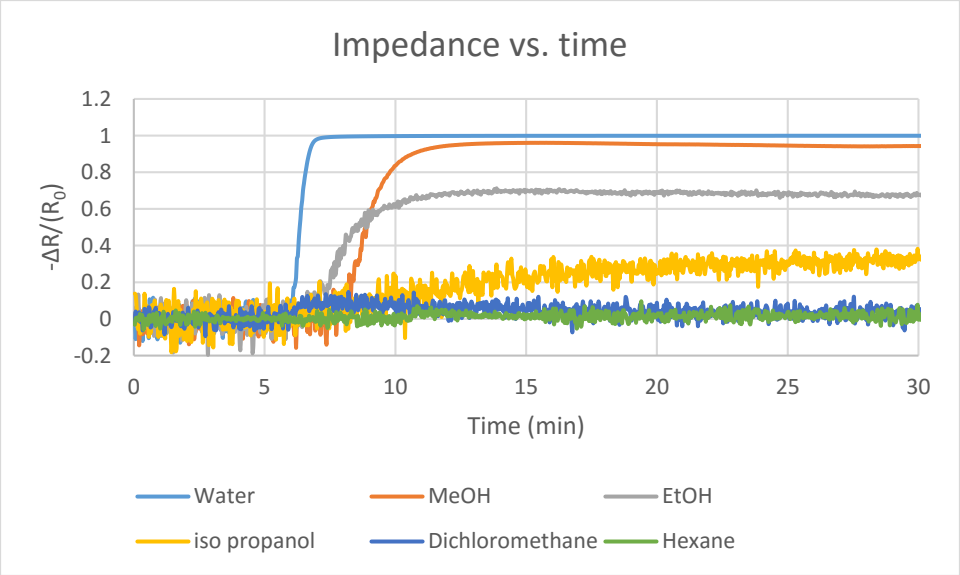

Figure 59. Selectivity impedance measurement of the sensor, responding to different vapors.

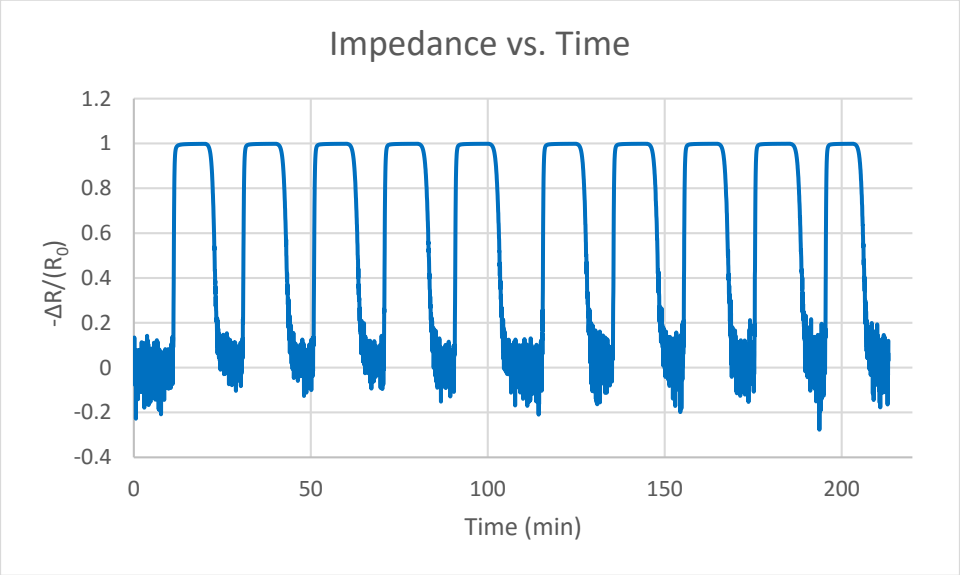

Figure 60. Reproducibility of the sensor with the exposure to water vapor

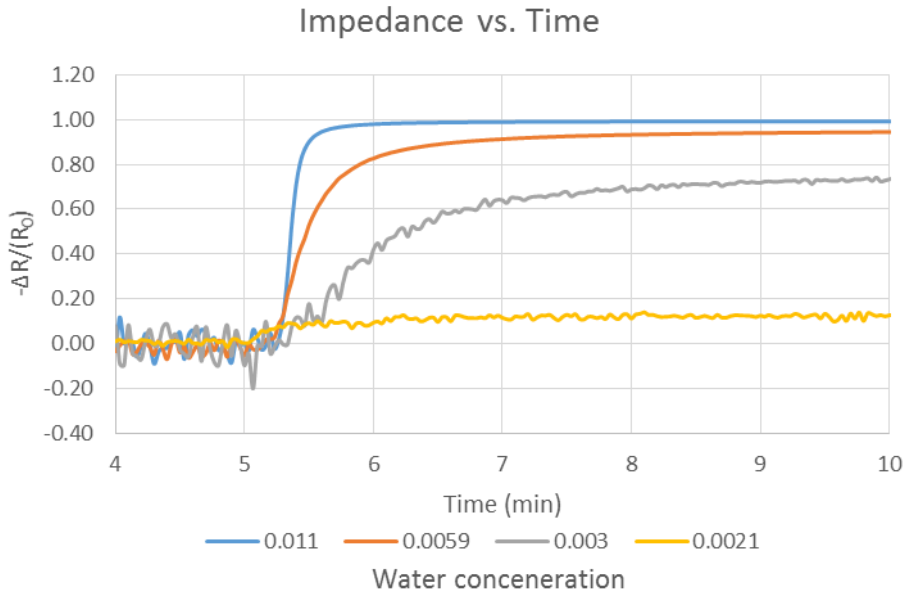

Figure 61. Sensitivity impedance measurement of sensor for water vapor

7.4 Conclusion

Similar to the previous chapter we were able to electrochemically fabricate another inorganic/organic structure using the KCP crystals and AuNPs as seeds. The size of the KCP nanorods was controlled by nanoparticle confinement and the crystals show preferential growth (68%) on the AuNP seed compare to HOPG substrate. KCP crystal growth was also studied in real time with *in-situ* AFM, and the results match the obtained ex-situ data. Using the same principles, we manufactured a vapor sensor prototype using the electrochemical methods. The KCP crystal was grown on a gold pattern on silicon wafer substrate. The chip was connected to an electrochemical workstation and the impedance of the KCP crystal was monitored while the crystal is exposed to the target vapor. The sensor prototype shows great sensitivity, reversibility and selectivity required for commercialization of the prototype sensor. This study contributes to a better understanding of nanoparticle confinement and heterogeneous nucleation studies.

CHAPTER 8 CONCLUSIONS AND RECOMMENDATION FOR FUTURE WORK

8.1 Conclusions

This project focuses on the nanoconfinement effect on organic crystallization using nanopatterns and nanoparticles of various shapes. The design of the experiments is guided by the classical nucleation theory and observations made by other research groups on nanoconfinement phenomena. We apply mainly electrochemistry to make the nano seeds as well as the organic crystals but also include other synthesis methods such as particle lithography, CVD, and colloidal chemistry. The main characterization methods used in this study include FE-SEM, AFM, XRD, and TEM. We have arrived at a universal concept of using nanoparticle seeds to produced nanorod crystals and a hybrid inorganic/organic nanostructure by demonstrating this concept on diverse organic compounds including carboxylic acids (previous work from the Mao group), tetrathiafulvalene charge transfer salt (this work), and partially oxidized tetracyanoplatinate salt. Lastly, the project has produced an organic nanowire sensor prototype for the detection of volatile compounds.

In the first project, we used a well-formed OTS nanopattern to confine the crystallization of organic compounds to produce NP arrays. The reaction conditions were optimized to produce the multi-layer OTS nanorings that can later be used as nano-flasks. We were able to deposit molecular nanocrystal arrays in these OTS nano-flasks that are uniform in size and distribution. This concept is a reliable method to manufacture drug nanoparticle arrays. This study contributes to nanoconfinement study using nanopatterns.

Next, the electrochemical deposition of AuNP nanoparticles on HOPG was investigated. We were able to vary the size of synthesized AuNPs on HOPG in the range

of 50 nm to 1.3 μm. We were able to produce AuNPs of spherical, dendritic, and cubic shapes. The size and shape effect of the seed on crystallization can then be studied.

Later, the nanoconfinement effect using the nanoparticles of different sizes and shapes was studied in two sections. We studied the effect of nanoparticle seeds on the nucleation and crystallization of organic compounds and later we manufacture a vapor sensor using the same principles. The synthesized AuNPs with control over morphology, size and distribution in the previous section is used as seeds to produce inorganic/organic nanostructures based on heterogeneous nucleation theory. Crystallization of two different organic materials, $(TTF)Br_{0.76}$ and KCP on AuNP decorated HOPG substrate is studied using the electrochemical methods. The results demonstrate that size of induced organic crystal is controlled by the nucleation gold seeds. It was also demonstrated that the organic nanorods prefer to grow on the seed rather than the HOPG substrate.

Lastly, we were able to manufacture a vapor sensor prototype using the electrochemical methods. The KCP crystal was grown electrochemically on a designed gold pattern on silicon wafer substrate. The chip was connected to an electrochemical workstation, and the impedance of the KCP crystal was monitored while the crystal is exposed to the target vapor. The sensor prototype shows great sensitivity, reversibility and selectivity that are the main three factors for commercial sensor make it a promising candidate for the manufactured sensor.

Overall, this dissertation contributes to a better understanding of SMN and heterogeneous nucleation study using nanoparticle confinement effect. We also established a universal strategy to synthesize controlled inorganic/organic hybrid materials using

electrochemical methods and using these principles we were able to manufacture a vapor sensor prototype with promising results for production.

8.2 Recommendations for future work

We were able to introduce a universal method to control the size and shape of AuNPs that can be extended to other types of inorganic materials like platinum, palladium, silver, copper, rhodium, and nickel. We only synthesized cube-shape AuNPs, and more work can be done to produce different shapes of inorganic crystals with this method. Inorganic-organic hybrid materials were synthesized on HOPG substrate; using the electrochemical technics. In this study, we only used the traditional AuNP seed that tends to have a spherical shape and uncontrollable dendritic shapes. Even the so-called spherical shape does not have a perfect spherical shape. Therefore, it will be very interesting to use the new shape control method to fabricate the well-shaped seed for the further growth of the organic rods to better study the effect of the seed morphology on the organic crystal growth. We were able to capture the crystal growth without disturbing the system, by using the *in-situ* AFM imaging in liquid. More work can be done to improve the real-time imaging of the crystal growth on the seed.

The studied organic crystals in this research have mostly plate-like habit. Basically, we only change the size of the crystal by heterogeneous nucleation. There are many other crystal structures in the TTF family that show plate-like shape when they grow in normal conditions like BEDT-TTF and $(BEDT\text{-}TTF)_2I_3$. More study can be done to study the effect of the seed to change the shape of the crystals.

A major setback for the electrodeposition of AuNP on HOPG is that it is mostly a random event, and we cannot control the position of the particles. In one of our studies we

were able to produce a well-ordered OTS nanorings on silicon wafer substrate. With controlling the adsorbed water on the surface and beneath the PS particles it is possible to synthesize a single layer or multilayer film with the well-formed pattern. We were also able to synthesize AuNP particles on silicon substrates and it is possible to use this pattern to grow the seeds in the nanopattern rings. With this method, it is possible to produce a well formed AuNP pattern on the substrate using the electrochemical methods.

REFERENCES

1. Sanchez, C.; Julian, B.; Belleville, P.; Popall, M., Applications of hybrid organic-inorganic nanocomposites. *J Mater Chem* **2005,** *15* (35-36), 3559-3592.

2. Mullin, J. W., *Crystallization*. 4th ed.; Butterworth-Heinemann: Oxford ; Boston, 2001; p xv, 594 p.

3. Ha, J. M.; Hamilton, B. D.; Hillmyer, M. A.; Ward, M. D., Phase Behavior and Polymorphism of Organic Crystals Confined within Nanoscale Chambers. *Cryst Growth Des* **2009,** *9* (11), 4766-4777.

4. Chayen, N. E.; Saridakis, E.; El-Bahar, R.; Nemirovsky, Y., Porous silicon: an effective nucleation-inducing material for protein crystallization. *J Mol Biol* **2001,** *312* (4), 591-595.

5. Hamilton, B. D.; Weissbuch, I.; Lahav, M.; Hillmyer, M. A.; Ward, M. D., Manipulating Crystal Orientation in Nanoscale Cylindrical Pores by Stereochemical Inhibition. *J Am Chem Soc* **2009,** *131* (7), 2588-2596.

6. Mao, G. Z.; Handa, H.; Chen, D.; Dong, W. F.; Kurth, D. G.; Mohwald, H., Nanopattern-directed crystallization of aspirin. *Abstr Pap Am Chem S* **2007,** *233*.

7. Mao, G. Z.; Dong, W. F.; Kurth, D. G.; Mohwald, H., Synthesis of copper sulfide nanorod arrays on molecular templates. *Nano Lett* **2004,** *4* (2), 249-252.

8. Favier, F.; Penner, R. M.; Liu, H., Size-selective electrosynthesis of TTFBr on Pt nanoparticles. *Abstr Pap Am Chem S* **2001,** *221*, U332-U333.

9. Favier, F.; Liu, H. T.; Penner, R. M., Size-selective growth of nanoscale tetrathiafulvalene bromide crystallites on platinum particles. *Adv Mater* **2001,** *13* (20), 1567-+.

10. Wang, S. X.; Li, L.; Mao, G. Z., Formation of Carboxylic Acid Nanorods on Oleylamide-Capped Au Nanoparticles. *J Phys Chem C* **2012,** *116* (9), 5492-5498.

11. Tao, A. R.; Habas, S.; Yang, P. D., Shape control of colloidal metal nanocrystals. *Small* **2008,** *4* (3), 310-325.

12. Murphy, C. J.; Gole, A. M.; Hunyadi, S. E.; Orendorff, C. J., One-dimensional colloidal gold and silver nanostructures. *Inorg Chem* **2006,** *45* (19), 7544-7554.

13. Pankhurst, Q. A.; Connolly, J.; Jones, S. K.; Dobson, J., Applications of magnetic nanoparticles in biomedicine. *J Phys D Appl Phys* **2003,** *36* (13), R167-R181.

14. Dobson, J., Gene therapy progress and prospects: magnetic nanoparticle-based gene delivery. *Gene Ther* **2006,** *13* (4), 283-287.

15. Rudge, S.; Peterson, C.; Vessely, C.; Koda, J.; Stevens, S.; Catterall, L., Adsorption and desorption of chemotherapeutic drugs from a magnetically targeted carrier (MTC). *J Control Release* **2001,** *74* (1-3), 335-340.

16. Laurent, S.; Forge, D.; Port, M.; Roch, A.; Robic, C.; Elst, L. V.; Muller, R. N., Magnetic iron oxide nanoparticles: Synthesis, stabilization, vectorization, physicochemical characterizations, and biological applications. *Chem Rev* **2008,** *108* (6), 2064-2110.

17. Xia, Y. N.; Xiong, Y. J.; Lim, B.; Skrabalak, S. E., Shape-Controlled Synthesis of Metal Nanocrystals: Simple Chemistry Meets Complex Physics? *Angew Chem Int Edit* **2009,** *48* (1), 60-103.

18. Xiong, Y. J.; Xia, Y. N., Shape-controlled synthesis of metal nanostructures: The case of palladium. *Adv Mater* **2007,** *19* (20), 3385-3391.

19. Harris, P. J. F., Sulfur-Induced Faceting of Platinum Catalyst Particles. *Nature* **1986,** *323* (6091), 792-794.

20. Tao, A.; Sinsermsuksakul, P.; Yang, P. D., Polyhedral silver nanocrystals with distinct scattering signatures. *Angew Chem Int Edit* **2006,** *45* (28), 4597-4601.

21. Niu, W. X.; Zheng, S. L.; Wang, D. W.; Liu, X. Q.; Li, H. J.; Han, S. A.; Chen, J.; Tang, Z. Y.; Xu, G. B., Selective Synthesis of Single-Crystalline Rhombic Dodecahedral, Octahedral, and Cubic Gold Nanocrystals. *J Am Chem Soc* **2009,** *131* (2), 697-703.

22. Guo, S. J.; Wang, E. K., Synthesis and electrochemical applications of gold nanoparticles. *Anal Chim Acta* **2007,** *598* (2), 181-192.

23. Shipway, A. N.; Katz, E.; Willner, I., Nanoparticle arrays on surfaces for electronic, optical, and sensor applications. *Chemphyschem* **2000,** *1* (1), 18-52.

24. Turkevich, J.; Stevenson, P. C.; Hillier, J., A Study of the Nucleation and Growth Processes in the Synthesis of Colloidal Gold. *Discuss Faraday Soc* **1951,** (11), 55-&.

25. Yee, C.; Scotti, M.; Ulman, A.; White, H.; Rafailovich, M.; Sokolov, J., One-phase synthesis of thiol-functionalized platinum nanoparticles. *Langmuir* **1999,** *15* (13), 4314-4316.

26. Huang, D.; Liao, F.; Molesa, S.; Redinger, D.; Subramanian, V., Plastic-compatible low resistance printable gold nanoparticle conductors for flexible electronics. *J Electrochem Soc* **2003,** *150* (7), G412-G417.

27. Stuchinskaya, T.; Moreno, M.; Cook, M. J.; Edwards, D. R.; Russell, D. A., Targeted photodynamic therapy of breast cancer cells using antibody-phthalocyanine-gold nanoparticle conjugates. *Photoch Photobio Sci* **2011,** *10* (5), 822-831.

28. Ali, M. E.; Hashim, U.; Mustafa, S.; Man, Y. B. C.; Islam, K. N., Gold Nanoparticle Sensor for the Visual Detection of Pork Adulteration in Meatball Formulation. *J Nanomater* **2012**.

29. Thompson, D. T., Using gold nanoparticles for catalysis. *Nano Today* **2007,** *2* (4), 40-43.

30. Pope, M.; Magnante, P.; Kallmann, H. P., Electroluminescence in Organic Crystals. *J Chem Phys* **1963,** *38* (8), 2042-&.

31. Tang, C. W.; Albrecht, A. C., Photovoltaic Effects of Metal-Chlorophyll-a-Metal Sandwich Cells. *J Chem Phys* **1975,** *62* (6), 2139-2149.

32. Koch, N., Organic electronic devices and their functional interfaces. *Chemphyschem* **2007,** *8* (10), 1438-1455.

33. Sun, D. M.; Liu, C.; Ren, W. C.; Cheng, H. M., A Review of Carbon Nanotube- and Graphene-Based Flexible Thin-Film Transistors. *Small* **2013,** *9* (8), 1188-1205.

34. Cao, Q.; Hur, S. H.; Zhu, Z. T.; Sun, Y. G.; Wang, C. J.; Meitl, M. A.; Shim, M.; Rogers, J. A., Highly bendable, transparent thin-film transistors that use carbon-nanotube-based conductors and semiconductors with elastomeric dielectrics. *Adv Mater* **2006,** *18* (3), 304-+.

35. Sangwan, V. K.; Southard, A.; Moore, T. L.; Ballarotto, V. W.; Hines, D. R.; Fuhrer, M. S.; Williams, E. D., Transfer printing approach to all-carbon nanoelectronics. *Microelectron Eng* **2011,** *88* (10), 3150-3154.

36. Aikawa, S.; Einarsson, E.; Thurakitseree, T.; Chiashi, S.; Nishikawa, E.; Maruyama, S., Deformable transparent all-carbon-nanotube transistors. *Appl Phys Lett* **2012,** *100* (6).

37. Heister, E.; Brunner, E. W.; Dieckmann, G. R.; Jurewicz, I.; Dalton, A. B., Are Carbon Nanotubes a Natural Solution? Applications in Biology and Medicine. *Acs Appl Mater Inter* **2013,** *5* (6), 1870-1891.

38. Wu, W.; Wieckowski, S.; Pastorin, G.; Benincasa, M.; Klumpp, C.; Briand, J. P.; Gennaro, R.; Prato, M.; Bianco, A., Targeted delivery of amphotericin B to cells by using functionalized carbon nanotubes. *Angew Chem Int Edit* **2005,** *44* (39), 6358-6362.

39. Martins, M. A.; Fateixa, S.; Girao, A. V.; Pereira, S. S.; Trindade, T., Shaping Gold Nanocomposites with Tunable Optical Properties. *Langmuir* **2010,** *26* (13), 11407-11412.

40. Shi, Y.; Yang, R. Z.; Yuet, P. K., Easy decoration of carbon nanotubes with well dispersed gold nanoparticles and the use of the material as an electrocatalyst. *Carbon* **2009,** *47* (4), 1146-1151.

41. Fischler, M.; Simon, U., Metal nanoparticle-DNA hybrids - from assembly towards functional conjugates. *J Mater Chem* **2009,** *19* (11), 1518-1523.

42. Yamada, M.; Aono, H., DNA-inorganic hybrid material as selective absorbent for harmful compounds. *Polymer* **2008,** *49* (21), 4658-4665.

43. Chuang, Y. J.; Tseng, F. G.; Lin, W. K., Reduction of diffraction effect of UV exposure on SU-8 negative thick photoresist by air gap elimination. *Microsyst Technol* **2002,** *8* (4-5), 308-313.

44. Sun, H. B.; Kawata, S., Two-photon photopolymerization and 3D lithographic microfabrication. *Adv Polym Sci* **2004,** *170*, 169-273.

45. Yamazaki, K.; Namatsu, H., Two-axis-of-rotation drive system in electron-beam lithography apparatus for nanotechnology applications. *Microelectron Eng* **2004,** *73-4*, 85-89.

46. Fujii, T.; Iwasaki, K.; Munekane, M.; Takeuchi, T.; Hasuda, M.; Asahata, T.; Kiyohara, M.; Kogure, T.; Kijima, Y.; Kaito, T., A nanofactory by focused ion beam. *J Micromech Microeng* **2005,** *15* (10), S286-S291.

47. van Kan, J. A.; Bettiol, A. A.; Watt, F., Three-dimensional nanolithography using proton beam writing. *Appl Phys Lett* **2003,** *83* (8), 1629-1631.

48. Mamin, H. J.; Terris, B. D.; Fan, L. S.; Hoen, S.; Barrett, R. C.; Rugar, D., High-density data storage using proximal probe techniques. *Ibm J Res Dev* **1995,** *39* (6), 681-699.

49. Despont, M.; Drechsler, U.; Yu, R.; Pogge, H. B.; Vettiger, P., Wafer-scale microdevice transfer/interconnect: Its application in an AFM-based data-storage system. *J Microelectromech S* **2004,** *13* (6), 895-901.

50. Minne, S. C.; Manalis, S. R.; Atalar, A.; Quate, C. F., Independent parallel lithography using the atomic force microscope. *J Vac Sci Technol B* **1996,** *14* (4), 2456-2461.

51. Vettiger, P.; Cross, G.; Despont, M.; Drechsler, U.; Durig, U.; Haberle, W.; Lutwyche, M. I.; Rothuizen, H. E.; Stutz, R.; Widmer, R.; Binnig, G. K., The "Millipede"-more than 1000 tips for parallel and dense data storage. *Transducers '01: Eurosensors Xv, Digest of Technical Papers, Vols 1 and 2* **2001**, 1054-1057.

52. Vettiger, P.; Despont, M.; Drechsler, U.; Durig, U.; Haberle, W.; Lutwyche, M. I.; Rothuizen, H. E.; Stutz, R.; Widmer, R.; Binnig, G. K., The "Millipede" - More than one thousand tips for future AFM data storage. *Ibm J Res Dev* **2000,** *44* (3), 323-340.

53. Smay, J. E.; Gratson, G. M.; Shepherd, R. F.; Cesarano, J.; Lewis, J. A., Directed colloidal assembly of 3D periodic structures. *Adv Mater* **2002,** *14* (18), 1279-+.

54. Gratson, G. M.; Xu, M. J.; Lewis, J. A., Microperiodic structures - Direct writing of three-dimensional webs. *Nature* **2004,** *428* (6981), 386-386.

55. Bao, L. R.; Cheng, X.; Huang, X. D.; Guo, L. J.; Pang, S. W.; Yee, A. F., Nanoimprinting over topography and multilayer three-dimensional printing. *J Vac Sci Technol B* **2002,** *20* (6), 2881-2886.

56. Lee, J. H.; Kim, C. H.; Ho, K. M.; Constant, K., Two-polymer microtransfer molding for highly layered microstructures. *Adv Mater* **2005,** *17* (20), 2481-+.

57. Li, J. R.; Lusker, K. L.; Yu, J. J.; Garno, J. C., Engineering the Spatial Selectivity of Surfaces at the Nanoscale Using Particle Lithography Combined with Vapor Deposition of Organosilanes. *Acs Nano* **2009,** *3* (7), 2023-2035.

58. Sagiv, J., Organized Monolayers by Adsorption .1. Formation and Structure of Oleophobic Mixed Monolayers on Solid-Surfaces. *J Am Chem Soc* **1980,** *102* (1), 92-98.

59. Wasserman, S. R.; Tao, Y. T.; Whitesides, G. M., Structure and Reactivity of Alkylsiloxane Monolayers Formed by Reaction of Alkyltrichlorosilanes on Silicon Substrates. *Langmuir* **1989,** *5* (4), 1074-1087.

60. Wasserman, S. R.; Whitesides, G. M.; Tidswell, I. M.; Ocko, B. M.; Pershan, P. S.; Axe, J. D., The Structure of Self-Assembled Monolayers of Alkylsiloxanes on Silicon - a Comparison of Results from Ellipsometry and Low-Angle X-Ray Reflectivity. *J Am Chem Soc* **1989,** *111* (15), 5852-5861.

61. Dong, J. P.; Wang, A. F.; Ng, K. Y. S.; Mao, G. Z., Self-assembly of octadecyltrichlorosilane monolayers on silicon-based substrates by chemical vapor deposition. *Thin Solid Films* **2006,** *515* (4), 2116-2122.

62. Legrange, J. D.; Markham, J. L.; Kurkjian, C. R., Effects of Surface Hydration on the Deposition of Silane Monolayers on Silica. *Langmuir* **1993,** *9* (7), 1749-1753.

63. Denkov, N. D.; Velev, O. D.; Kralchevsky, P. A.; Ivanov, I. B.; Yoshimura, H.; Nagayama, K., Mechanism of Formation of 2-Dimensional Crystals from Latex-Particles on Substrates. *Langmuir* **1992,** *8* (12), 3183-3190.

64. Denkov, N. D.; Velev, O. D.; Kralchevsky, P. A.; Ivanov, I. B.; Yoshimura, H.; Nagayama, K., 2-Dimensional Crystallization. *Nature* **1993,** *361* (6407), 26-26.

65. Li, J. R.; Garno, J. C., Elucidating the role of surface hydrolysis in preparing organosilane nanostructures via particle lithography. *Nano Lett* **2008,** *8* (7), 1916-1922.

66. Lusker, K. L.; Yu, J. J.; Garno, J. C., Particle lithography with vapor deposition of organosilanes: A molecular toolkit for studying confined surface reactions in nanoscale liquid volumes. *Thin Solid Films* **2011,** *519* (15), 5223-5229.

67. Mao, G. Z.; Chen, D. Z.; Handa, H.; Dong, W. F.; Kurth, D. G.; Mohwald, H., Deposition and aggregation of aspirin molecules on a phospholipid bilayer pattern. *Langmuir* **2005,** *21* (2), 578-585.

68. Wang, S. X.; Sobczynski, D. J.; Jahanian, P.; Xhahysa, J.; Mao, G. Z., A Supra-monolayer Nanopattern for Organic Nanoparticle Array Deposition. *Acs Appl Mater Inter* **2013,** *5* (7), 2699-2707.

69. Chen, J. X.; Liao, W. S.; Chen, X.; Yang, T. L.; Wark, S. E.; Son, D. H.; Batteas, J. D.; Cremer, P. S., Evaporation-Induced Assembly of Quantum Dots into Nanorings. *Acs Nano* **2009,** *3* (1), 173-180.

70. Xia, Y. N.; Halas, N. J., Shape-controlled synthesis and surface plasmonic properties of metallic nanostructures. *Mrs Bull* **2005,** *30* (5), 338-344.

71. El-Sayed, M. A., Some interesting properties of metals confined in time and nanometer space of different shapes. *Accounts Chem Res* **2001,** *34* (4), 257-264.

72. Kamat, P. V., Photophysical, photochemical and photocatalytic aspects of metal nanoparticles. *J Phys Chem B* **2002,** *106* (32), 7729-7744.

73. Daniel, M. C.; Astruc, D., Gold nanoparticles: Assembly, supramolecular chemistry, quantum-size-related properties, and applications toward biology, catalysis, and nanotechnology. *Chem Rev* **2004,** *104* (1), 293-346.

74. Zangwill, A., *Physics at surfaces*. Cambridge University Press: Cambridge Cambridgeshire ; New York, 1988; p xiii, 454 p.

75. Thomas, K. G.; Kamat, P. V., Chromophore-functionalized gold nanoparticles. *Accounts Chem Res* **2003,** *36* (12), 888-898.

76. Nam, J. M.; Thaxton, C. S.; Mirkin, C. A., Nanoparticle-based bio-bar codes for the ultrasensitive detection of proteins. *Science* **2003,** *301* (5641), 1884-1886.

77. Taton, T. A.; Mirkin, C. A.; Letsinger, R. L., Scanometric DNA array detection with nanoparticle probes. *Science* **2000,** *289* (5485), 1757-1760.

78. Elghanian, R.; Storhoff, J. J.; Mucic, R. C.; Letsinger, R. L.; Mirkin, C. A., Selective colorimetric detection of polynucleotides based on the distance-dependent optical properties of gold nanoparticles. *Science* **1997,** *277* (5329), 1078-1081.

79. Dykman, L.; Khlebtsov, N., Gold nanoparticles in biomedical applications: recent advances and perspectives. *Chem Soc Rev* **2012,** *41* (6), 2256-2282.

80. Seo, D.; Park, J. C.; Song, H., Polyhedral gold nanocrystals with O-h symmetry: From octahedra to cubes. *J Am Chem Soc* **2006,** *128* (46), 14863-14870.

81. Murphy, C. J.; San, T. K.; Gole, A. M.; Orendorff, C. J.; Gao, J. X.; Gou, L.; Hunyadi, S. E.; Li, T., Anisotropic metal nanoparticles: Synthesis, assembly, and optical applications. *J Phys Chem B* **2005,** *109* (29), 13857-13870.

82. Murphy, C. J.; Jana, N. R., Controlling the aspect ratio of inorganic nanorods and nanowires. *Adv Mater* **2002,** *14* (1), 80-82.

83. Liu, H.; Favier, F.; Ng, K.; Zach, M. P.; Penner, R. M., Size-selective electrodeposition of meso-scale metal particles: a general method. *Electrochim Acta* **2001,** *47* (5), 671-677.

84. Li, L.; Jahanian, P.; Mao, G. Z., Electrocrystallization of Tetrathiafulvalene Charge-Transfer Salt Nanorods on Gold Nanoparticle Seeds. *J Phys Chem C* **2014,** *118* (32), 18771-18782.

85. Martin, H.; Carro, P.; Creus, A. H.; Gonzalez, S.; Salvarezza, R. C.; Arvia, A. J., Growth mode transition involving a potential-dependent isotropic to anisotropic surface atom diffusion change. Gold electrodeposition on HOPG followed by STM. *Langmuir* **1997,** *13* (1), 100-110.

86. Liu, H.; Penner, R. M., Size-selective electrodeposition of mesoscale metal particles in the uncoupled limit. *Journal of Physical Chemistry B* **2000,** *104* (39), 9131-9139.

87. Li, C. C.; Shuford, K. L.; Park, Q. H.; Cai, W. P.; Li, Y.; Lee, E. J.; Cho, S. O., High-yield synthesis of single-crystalline gold nano-octahedra. *Angew Chem Int Edit* **2007,** *46* (18), 3264-3268.

88. Seo, D.; Il Yoo, C.; Chung, I. S.; Park, S. M.; Ryu, S.; Song, H., Shape adjustment between multiply twinned and single-crystalline polyhedral gold nanocrystals: Decahedra, icosahedra, and truncated tetrahedra. *J Phys Chem C* **2008,** *112* (7), 2469-2475.

89. Connor, S.; Kim, F.; Song, H.; Goldberger, J.; Yang, P. D., Syntheses and optical properties of gold nanocube, -prism, and -icosahedron. *Abstr Pap Am Chem S* **2004,** *227*, U1309-U1309.

90. Kim, F.; Connor, S.; Song, H.; Kuykendall, T.; Yang, P. D., Platonic gold nanocrystals. *Angew Chem Int Edit* **2004,** *43* (28), 3673-3677.

91. Edelstein, A. S.; Cammarata, R. C.; NetLibrary Inc., Nanomaterials synthesis, properties, and applications. Pbk. ed.; Institute of Physics Pub.,: Bristol ; Philadelphia, 1998; pp. xxii, 596 p..

92. Yuan, J. Y.; Xu, Y. Y.; Muller, A. H. E., One-dimensional magnetic inorganic-organic hybrid nanomaterials. *Chem Soc Rev* **2011,** *40* (2), 640-655.

93. Luryi, S.; Xu, J.; Zaslavsky, A.; ebrary Inc., Future Trends in Microelectronics frontiers and innovations. Wiley,: Hoboken, N.J., 2013; pp. 1 online resource (xiii, 403 p.).

94. Ross, C., Patterned magnetic recording media. *Annu Rev Mater Res* **2001,** *31*, 203-235.

95. Bachtold, A.; Hadley, P.; Nakanishi, T.; Dekker, C., Logic circuits with carbon nanotube transistors. *Science* **2001,** *294* (5545), 1317-1320.

96. Ferraris, J.; Walatka, V.; Perlstei.Jh; Cowan, D. O., Electron-Transfer in a New Highly Conducting Donor-Acceptor Complex. *J Am Chem Soc* **1973,** *95* (3), 948-949.

97. Mas-Torrent, M.; Hadley, P., Electrochemical growth of organic conducting microcrystals of tetrathiafulvalene bromide. *Small* **2005,** *1* (8-9), 806-808.

98. Batail, P.; Boubekeur, K.; Fourmigue, M.; Gabriel, J. C. P., Electrocrystallization, an invaluable tool for the construction of ordered, electroactive molecular solids. *Chem Mater* **1998,** *10* (10), 3005-3015.

99. Li, L.; Jahanian, P.; Mao, G., Electrocrystallization of Tetrathiafulvalene Charge-Transfer Salt Nanorods on Gold Nanoparticle Seeds. *The Journal of Physical Chemistry C* **2014,** *118* (32), 18771-18782.

100. Fan, Z. Y.; Ho, J. C.; Takahashi, T.; Yerushalmi, R.; Takei, K.; Ford, A. C.; Chueh, Y. L.; Javey, A., Toward the Development of Printable Nanowire Electronics and Sensors. *Adv Mater* **2009,** *21* (37), 3730-3743.

101. Long, Y. Z.; Yu, M.; Sun, B.; Gu, C. Z.; Fan, Z. Y., Recent advances in large-scale assembly of semiconducting inorganic nanowires and nanofibers for electronics, sensors and photovoltaics. *Chem Soc Rev* **2012,** *41* (12), 4560-4580.

102. Xia, Y. N.; Yang, P. D.; Sun, Y. G.; Wu, Y. Y.; Mayers, B.; Gates, B.; Yin, Y. D.; Kim, F.; Yan, Y. Q., One-dimensional nanostructures: Synthesis, characterization, and applications. *Adv Mater* **2003,** *15* (5), 353-389.

103. Tian, B.; Kempa, T. J.; Lieber, C. M., Single nanowire photovoltaics. *Chem Soc Rev* **2009,** *38* (1), 16-24.

104. Hochbaum, A. I.; Yang, P. D., Semiconductor Nanowires for Energy Conversion. *Chem Rev* **2010,** *110* (1), 527-546.

105. Fang, X. S.; Zhai, T. Y.; Gautam, U. K.; Li, L.; Wu, L. M.; Yoshio, B.; Golberg, D., ZnS nanostructures: From synthesis to applications. *Prog Mater Sci* **2011,** *56* (2), 175-287.

106. Kempa, T. J.; Day, R. W.; Kim, S. K.; Park, H. G.; Lieber, C. M., Semiconductor nanowires: a platform for exploring limits and concepts for nano-enabled solar cells. *Energ Environ Sci* **2013,** *6* (3), 719-733.

107. Moulin, E.; Cid, J. J.; Giuseppone, N., Advances in Supramolecular Electronics - From Randomly Self-assembled Nanostructures to Addressable Self-Organized Interconnects. *Adv Mater* **2013,** *25* (3), 477-487.

108. Mansour, M. A.; Connick, W. B.; Lachicotte, R. J.; Gysling, H. J.; Eisenberg, R., Linear chain Au(I) dimer compounds as environmental sensors: A luminescent switch for the detection of volatile organic compounds. *Journal of the American Chemical Society* **1998,** *120* (6), 1329-1330.

109. Beauvais, L. G.; Shores, M. P.; Long, J. R., Cyano-bridged Re(6)Q(8) (Q = S, Se) Cluster-Cobalt(II) framework materials: Versatile solid chemical sensors. *Journal of the American Chemical Society* **2000,** *122* (12), 2763-2772.

110. Cariati, E.; Bu, X. H.; Ford, P. C., Solvent- and vapor-induced isomerization between the luminescent solids [CuI(4-pic)](4) and [CuI(4-pic)](infinity) (pic = methylpyridine). The structural basis for the observed luminescence vapochromism. *Chem Mater* **2000,** *12* (11), 3385-3391.

111. Evju, J. K.; Mann, K. R., Synthesis and spectroscopic investigations of a crystalline humidity sensor: Bis(triphenylphosphine) iminium 2,2 '-bipyridyltetracyanoruthenate. *Chem Mater* **1999,** *11* (6), 1425-1433.

112. Persaud, K.; Dodd, G., Analysis of Discrimination Mechanisms in the Mammalian Olfactory System Using a Model Nose. *Nature* **1982,** *299* (5881), 352-355.

113. Corcoran, P.; Shurmer, H. V., An Intelligent Gas Sensor. *Sensor Actuat a-Phys* **1994,** *41* (1-3), 192-197.

114. Dickert, F. L.; Haunschild, A., Sensor Materials for Solvent Vapor Detection - Donor-Acceptor and Host-Guest Interactions. *Adv Mater* **1993,** *5* (12), 887-895.

115. Postma, H. W. C.; de Jonge, M.; Yao, Z.; Dekker, C., Electrical transport through carbon nanotube junctions created by mechanical manipulation. *Phys Rev B* **2000,** *62* (16), 10653-10656.

116. Hamada, Y.; Negishi, H.; Akita, S.; Nakayama, Y., Electrical properties of connected multiwall carbon nanotubes. *Jpn J Appl Phys 1* **2005,** *44* (4A), 1629-1632.

117. Fan, F.-R.; Ding, Y.; Liu, D.-Y.; Tian, Z.-Q.; Wang, Z. L., Facet-Selective Epitaxial Growth of Heterogeneous Nanostructures of Semiconductor and Metal: ZnO Nanorods on Ag Nanocrystals. *Journal of the American Chemical Society* **2009,** *131* (34), 12036-12037.

118. Hao, E.; Bailey, R. C.; Schatz, G. C.; Hupp, J. T.; Li, S., Synthesis and Optical Properties of "Branched" Gold Nanocrystals. *Nano Lett.* **2004,** *4* (2), 327-330.

119. Takagi, D.; Hibino, H.; Suzuki, S.; Kobayashi, Y.; Homma, Y., Carbon Nanotube Growth from Semiconductor Nanoparticles. *Nano Lett.* **2007,** *7* (8), 2272-2275.

120. Wang, D. S.; Li, Y. D., Bimetallic Nanocrystals: Liquid-Phase Synthesis and Catalytic Applications. *Adv Mater* **2011,** *23* (9), 1044-1060.

121. Xia, Y.; Xiong, Y. J.; Lim, B.; Skrabalak, S. E., Shape-Controlled Synthesis of Metal Nanocrystals: Simple Chemistry Meets Complex Physics? *Angewandte Chemie-International Edition* **2009,** *48* (1), 60-103.

122. Caruso, F., Nanoengineering of Particle Surfaces. *Adv Mater* **2001,** *13* (1), 11-22.

123. Khanal, A.; Inoue, Y.; Yada, M.; Nakashima, K., Synthesis of Silica Hollow Nanoparticles Templated by Polymeric Micelle with Core-Shell-Corona Structure. *J. Am. Chem. Soc.* **2007,** *129* (6), 1534-1535.

124. Shin, K.; Xiang, H.; Moon, S. I.; Kim, T.; McCarthy, T. J.; Russell, T. P., Curving and Frustrating Flatland. *Science* **2004,** *306* (5693), 76-.

125. Zhang, H.; Han, J.; Yang, B., Structural Fabrication and Functional Modulation of Nanoparticle–Polymer Composites. *Advanced Functional Materials* **2010,** *20* (10), 1533-1550.

126. Chen, D.; Wang, R.; Arachchige, I.; Mao, G.; Brock, S. L., Particle-Rod Hybrids: Growth of Arachidic Acid Molecular Rods from Capped Cadmium Selenide Nanoparticles. *J. Am. Chem. Soc.* **2004,** *126* (50), 16290-16291.

127. Wang, R. M.; Li, L.; Arachchige, I.; Ganguly, S.; Brock, S. L.; Mao, G. Z., Nanoparticles Change the Ordering Pattern of n-Carboxylic Acids into Nanorods on HOPG. *Acs Nano* **2010,** *4* (11), 6687-6696.

128. Leclere, P.; Surin, M.; Jonkheijm, P.; Henze, O.; Schenning, A. P. H. J.; Biscarini, F.; Grimsdale, A. C.; Feast, W. J.; Meijer, E. W.; Mullen, K.; Bredas, J. L.; Lazzaroni, R., Organic semi-conducting architectures for supramolecular electronics. *European Polymer Journal* **2004,** *40* (5), 885-892.

129. Mullen, K.; Rabe, J. P., Macromolecular and supramolecular architectures for molecular electronics. *Molecular Electronics: Science and Technology* **1998,** *852*, 205-218.

130. Ruaudelteixier, A., Supramolecular Assemblies for Molecular Electronics. *Molecular Crystals and Liquid Crystals Science and Technology Section a-Molecular Crystals and Liquid Crystals* **1994,** *255*, 27-33.

131. Schenning, A. P. H. J.; Jonkheijm, P.; Hoeben, F. J. M.; van Herrikhuyzen, J.; Meskers, S. C. J.; Meijer, E. W.; Herz, L. M.; Daniel, C.; Silva, C.; Phillips, R. T.; Friend, R. H.; Beljonne, D.; Miura, A.; De Feyter, S.; Zdanowska, M.; Uji-i, H.; De Schryver, F.

C.; Chen, Z.; Wurthner, F.; Mas-Torrent, M.; den Boer, D.; Durkut, M.; Hadley, P., Towards supramolecular electronics. *Synthetic Metals* **2004,** *147* (1-3), 43-48.

132. Schenning, A. P. H. J.; Meijer, E. W., Supramolecular electronics; nanowires from self-assembled pi-conjugated systems. *Chemical Communications* **2005,** (26), 3245-3258.

133. Dieter Horn, J. R., Organic Nanoparticles in the Aqueous Phase - Theory, Experiment, and Use. *Angewandte Chemie International Edition* **2001,** *40* (23), 4330-4361.

134. Nguyen, T. Q.; Martel, R.; Avouris, P.; Bushey, M. L.; Brus, L.; Nuckolls, C., Molecular interactions in one-dimensional organic nanostructures. *Journal of the American Chemical Society* **2004,** *126* (16), 5234-5242.

135. Asahi, T.; Sugiyama, T.; Masuhara, H., Laser Fabrication and Spectroscopy of Organic Nanoparticles. *Accounts of Chemical Research* **2008,** *41* (12), 1790-1798.

136. Zang, L.; Che, Y. K.; Moore, J. S., One-Dimensional Self-Assembly of Planar pi-Conjugated Molecules: Adaptable Building Blocks for Organic Nanodevices. *Accounts of Chemical Research* **2008,** *41* (12), 1596-1608.

137. Bera, J. K.; Dunbar, K. R., Chain compounds based on transition metal backbones: New life for an old topic. *Angew Chem Int Edit* **2002,** *41* (23), 4453-+.

138. Crespilho, F. N.; Zucolotto, V.; Brett, C. M. A.; Oliveira, O. N.; Nart, F. C., Enhanced Charge Transport and Incorporation of Redox Mediators in Layer-by-Layer Films Containing PAMAM-Encapsulated Gold Nanoparticles. *The Journal of Physical Chemistry B* **2006,** *110* (35), 17478-17483.

139. Bradbury, C. R.; Zhao, J. J.; Fermin, D. J., Distance-independent charge-transfer resistance at gold electrodes modified by thiol monolayers and metal nanoparticles. *J Phys Chem C* **2008,** *112* (27), 10153-10160.

140. Shein, J. B.; Lai, L. M. H.; Eggers, P. K.; Paddon-Row, M. N.; Gooding, J. J., Formation of Efficient Electron Transfer Pathways by Adsorbing Gold Nanoparticles to Self-Assembled Monolayer Modified Electrodes. *Langmuir* **2009,** *25* (18), 11121-11128.

141. Pruneanu, S.; Pogacean, F.; Biris, A. R.; Ardelean, S.; Canpean, V.; Blanita, G.; Dervishi, E.; Biris, A. S., Novel Graphene-Gold Nanoparticle Modified Electrodes for the High Sensitivity Electrochemical Spectroscopy Detection and Analysis of Carbamazepine. *J Phys Chem C* **2011,** *115* (47), 23387-23394.

142. Martín, H.; Carro, P.; Hernández Creus, A.; González, S.; Salvarezza, R. C.; Arvia, A. J., Growth Mode Transition Involving a Potential-Dependent Isotropic to Anisotropic Surface Atom Diffusion Change. Gold Electrodeposition on HOPG followed by STM. *Langmuir* **1997,** *13* (1), 100-110.

143. Schmidt, U.; Donten, M.; Osteryoung, J. G., Gold Electrocrystallization on Carbon and Highly Oriented Pyrolytic Graphite from Concentrated Solutions of LiCl. *Journal of The Electrochemical Society* **1997,** *144* (6), 2013-2021.

144. Boxley, C. J.; White, H. S.; Lister, T. E.; Pinhero, P. J., Electrochemical deposition and reoxidation of Au at highly oriented pyrolytic graphite. Stabilization of Au nanoparticles on the upper plane of step edges. *Journal of Physical Chemistry B* **2003,** *107* (2), 451-458.

145. Penner, R. M., Mesoscopic metal particles and wires by electrodeposition. *J Phys Chem B* **2002,** *106* (13), 3339-3353.

146. Krogmann, K., Planar Complexes Containing Metal-Metal Bonds. *Angewandte Chemie-International Edition* **1969,** *8* (1), 35-&.

147. Buss, C. E.; Mann, K. R., Synthesis and Characterization of Pt(CN-p-(C2H5)C6H4)2(CN)2, a Crystalline Vapoluminescent Compound That Detects Vapor-Phase Aromatic Hydrocarbons. *Journal of the American Chemical Society* **2002,** *124* (6), 1031-1039.

148. Kuse, D.; Zeller, H. R., Evidence for One-Dimensional Metallic Behavior in K2pt(Cn)4br0.3 (H2o)N. *Phys Rev Lett* **1971,** *27* (16), 1060-&.

149. Geserich, H. P.; Stampfl, P.; Hausen, H. D.; Krogmann, K., Optical Investigations on Metallic Behavior of K2pt(Cn)4clo.3.2.6h2o and K2pt(Cn)4bro.3.2.6h2o Single-Crystals. *Phys Status Solidi A* **1972,** *9* (1), 187-&.

150. Wagner, H.; Geserich, H. P.; Baltz, R. V.; Krogmann, K., Optical Conductivity and Electron Interaction in One-Dimensional Metal K2pt (Cn)4 Br0.3.3h2o. *Solid State Commun* **1973,** *13* (6), 659-663.

151. Comes, R.; Lambert, M.; Launois, H.; Zeller, H. R., Evidence for a Peierls Distortion or a Kohn Anomaly in One-Dimensional Conductors of Type K2pt(Cn)4bro30 Xh2o. *Phys Rev B* **1973,** *8* (2), 571-575.

152. Renker, B.; Rietsche.H; Pintscho.L; Glaser, W.; Bruesch, P.; Kuse, D.; Rice, M. J., Observation of Giant Kohn Anomaly in One-Dimensional Conductor K2pt(Cn)4br0.3.3h2o. *Phys Rev Lett* **1973,** *30* (22), 1144-1146.

153. Williams, J. M.; Petersen, J. L.; Gerdes, H. M.; Peterson, S. W., New Structural Findings from a Neutron-Diffraction Study of One-Dimensional K2pt(Cn)4br0.3.3h20. *Phys Rev Lett* **1974,** *33* (18), 1079-1081.

154. Williams, J. M.; Ross, F. K.; Iwata, M.; Petersen, J. L.; Peterson, S. W.; Lin, S. C.; Keefer, K., Neutron-Diffraction Study of Structural-Changes in One-Dimensional K2pt(Cn)4br0.3 3h2o from 77-323 Degreesk. *Solid State Commun* **1975,** *17* (1), 45-48.

155. Williams, J. M.; Iwata, M.; Ross, F. K.; Petersen, J. L.; Peterson, S. W., Comparison of Low-Temperature Neutron and X-Ray Structures of K2pt(Cn)4br0.3.3h2o, Kcp (Br). *Mater Res Bull* **1975,** *10* (5), 411-415.

156. Miller, J. S., Electrochemical Growth of Highly Conducting Inorganic Complexes. *Science* **1976,** *194* (4261), 189-189.

157. Williams, J. M.; Keefer, K. D.; Washecheck, D. M.; Enright, N. P., Structural Studies of Precursor and Partially Oxidized Conducting Complexes .1. Neutron-Diffraction and Spectroscopic Investigation of Quasi-One-Dimensional Potassium Tetracyanoplatinate (1.75-1) Sesquihydrate, K1.75[Pt(Cn)4].1.5h2o. *Inorg Chem* **1976,** *15* (10), 2446-2455.

158. Bloch, A. N.; Weisman, R. B., Some Comments on Electronic-Structure of Krogmann Salts and Stability of Pt 2.3. *Adv Chem Ser* **1974,** (5), 356-371.

159. Reis, A. H.; Peterson, S. W.; Washecheck, D. M.; Miller, J. S., Nature of Pt Chain Distortion in Partially Oxidized One-Dimensional Complex, K1.75pt(Cn)4.1.5h2o. *Inorg Chem* **1976,** *15* (10), 2455-2462.

160. Glynn, C.; Thompson, D.; Paez, J.; Collins, G.; Benavente, E.; Lavayen, V.; Yutronic, N.; Holmes, J. D.; Gonzalez, G.; O'Dwyer, C., Large directional conductivity change in chemically stable layered thin films of vanadium oxide and a 1D metal complex. *J Mater Chem C* **2013,** *1* (36), 5675-5684.

161. Melitz, W.; Shen, J.; Kummel, A. C.; Lee, S., Kelvin probe force microscopy and its application. *Surf Sci Rep* **2011,** *66* (1), 1-27.

162. Horowitz, P.; Hill, W., *The art of electronics*. 2nd ed.; Cambridge University Press: Cambridge England ; New York, 1989; p xxiii, 1125 p.

163. Reichardt, C., *Solvents and solvent effects in organic chemistry*. 3rd, updated and enl. ed.; Wiley-VCH: Weinheim, 2003; p xxiv, 629 p.

ABSTRACT

ENGINEERING GOLD NANOPARTICLES AND THEIR USE TO CONTROL NUCLEATION

by

PEDRAM JAHANIAN

May 2016

Advisor: Dr. Guangzhao Mao

Major: Chemical Engineering

Degree: Doctor of Philosophy

This study focuses on the fabrication of hybrid nanostructures using gold nanoparticles (AuNP) as seeds and partially oxidized potassium tetracyanoplatinate, known as Krogmann's salt (KCP), and later this method will be employed to manufacture a prototype sensor for detecting different vapors. Nanocrystals are synthesized using the electrochemical method with the aim to have more control over the size and shape of the charge transfer salt based on the seed-mediated nucleation method. AuNP seeds are prepared on highly ordered pyrolytic graphite (HOPG) substrate by the electrocrystallization method. An aqueous solution of 0.05 to 1 mM Hydrogen tetrachloroaurate ($HAuCl_4$) with 0.1 mM (Potassium chloride) KCl as the supporting electrolyte was prepared. The electrodeposition of the AuNPs was monitored by Cyclic Voltammetry (CV) and analyzed by Atomic Force Microscopy (AFM). The results show that the most dominant factor to control the AuNP size is the $HAuCl_4$ concentration. Deposition time and applied potential are the other factors controlling the electrodeposition. The smallest particle size was observed with the lowest $HAuCl_4$

concentration. The synthesis of $K_{1.75}Pt(CN)_4.1.5H2O$ rods is conducted according to literature on bare HOPG with a concentration of 0.07 M of $K_2Pt(CN)_4$ in DI water and a potential pulse of 1.5V (vs. SCE) for 0.1s. Needle shaped crystals with a size range of 600 nm to 5µm in length and 100-500nm in width were synthesized on the bare HOPG. When the experiment was conducted with the same conditions on AuNP decorated HOPG, in result, the average diameter and length of the rods were reduced significantly that matches our hypothesis based on seed-mediated nucleation theory. The results will help to have a better understanding of seed-mediated nucleation theory for producing nanoparticles of the desired size and shape, and also, introduce a new way of manufacturing future nanosensors and nanoelectrods. Next, micro-sized crystals were synthesized using the same method with longer deposition time on patterned Cr/Au electrodes. The conductivity of the KCP crystals was measured in the exposure of different vapors. The results show dramatic conductivity change after introducing the vapors to the sensor, and also, it shows a rapid respond and more sensitivity compare to commercial sensors.They prove that this prototype can be a reliable and cheap replacement of available sensors in different applications.

AUTOBIOGRAPHICAL STATEMENT

EDUCATION

- PhD, Chemical Engineering, Wayne State University, Detroit, United States, 2016
- M.Sc.,Chemical Engineering, Sistan and Baluchestan Universtiy, Zahedan, Iran, 2007
- B.S.,Chemical Engineering, Ferdowsi University of Mashhad, Mashhad, Iran, 2002

EXPERIENCES

- Graduate Research Assistant, Wayne State University, (1/2011 – 5/2016)
- Process Engineer, Nargan Company, Tehran, Iran (8/2007 – 1/2011)
- Process Engineer, Petro Farayand Energy Co., Tehran, Iran (11/2004 - 8/2007)

PUBLICATIONS AND PATENTS

- **Jahanian, P**.; Li, L.; Guangzhao, M., "Controlled Synthesis of Krogmann's Salt Nanorod on Gold Nanopartilce Seeds". In Preparation
- Li, L.; **Jahanian, P.**; Mao, G. Z., "Electrocrystallization of Tetrathiafulvalene Charge-Transfer Salt Nanorods on Gold Nanoparticle Seeds". *J Phys Chem C,* **2014**. Published
- Wang, S. X.; Sobczynski, D. J.; **Jahanian, P.**; Xhahysa, J.; Mao, G. Z., "A Supra-monolayer Nanopattern for Organic Nanoparticle Array Deposition". *Acs Appl Mater Inter,* **2013**. Published
- Wang, S.; Sobczynski, D.; **Jahanian, P**.; Xhahysa, J.; Mao, G. "Controlled Synthesis of Partially Oxidized Tetracyanoplatinate Nanorods on Gold Nanoparticle Seeds". ***Published***